MAGYAR ÁLLAMI
EÖTVÖS LORÁND
GEOFIZIKAI INTÉZET

GEOFIZIKAI
KÖZLEMÉNYEK

ВЕНГЕРСКИЙ
ГЕОФИЗИЧЕСКИЙ
ИНСТИТУТ
ИМ Л. ЭТВЕША

ГЕОФИЗИЧЕСКИЙ
БЮЛЛЕТЕНЬ

GEOPHYSICAL

TRANSACTIONS

EÖTVÖS LORÁND GEOPHYSICAL INSTITUTE OF HUNGARY

CONTENTS

VOL. 39. NO. 1. NOVEMBER 1994. (ISSN 0016-7177)

BUDAPEST

TARTALOMJEGYZÉK

GEOPHYSICAL TRANSACTIONS 1994
Vol. 39. No. 1. pp. 3-33

ROLE OF GEOELECTRIC METHODS IN HYDROCARBON AND DEEP STRUCTURAL INVESTIGATIONS IN RUSSIA

Mark N. BERDICHEVSKY*

Editorial Note

The Editorial Board is aware of the unusual content of this paper; it differs from those generally published in Geophysical Transactions. The paper was accepted in spite of the fact that the theoretical considerations tend to be qualitative descriptions, and the case histories do not go into detail; identification of the geographic locations is by no means an easy task.

In our opinion, however, this review by Professor BERDICHEVSKY provides an insight —probably the first — into an area in which only a limited amount of information is available.

The history of geoelectric methods in Russia started with the resistivity method in the USSR before World War II . After the initial successes, however, frequency and transient soundings, and the magnetotelluric (MT) and telluric methods became dominant. Geoelectric methods are of great practical importance because they are used to investigate non-structural hydrocarbon deposits as well.

Theoretical aspects of the MT method, data processing, effects of lateral inhomogeneities, solutions to 2D and 3D in inverse problems are discussed. MT case histories from the Moscow syneclise, Western Siberia, Eastern Siberia (Siberian Platform), and Sakhalin are presented. Examples from investigating non-structural deposits are shown from Western Siberia, the Caspian Basin and Turkmenistan.

Techniques of *S*-transform, multiple overlap and normalized second differences used in transient soundings are illustrated by case histories from the Caspian Depression, Eastern Siberia and the Black Sea.

Frequency domain induced polarization profiling has successfully been applied to hydrocarbon detection in the North Caspian Depression.

Finally physical background and some results (Eastern Europe and Russia and, in detail, Kamchatka) of deep geomagnetic and magnetotelluric soundings are discussed.

Keywords: geoelectric methods, hydrocarbons, Russia

* Moscow State University, Geological Department, Moscow 119899, Lenin Hill, Russia
Manuscript received: 13 November, 1992

1. Introduction

The paper reviews the geoelectrical investigations carried out in Russia and the former Soviet Union. Interesting conclusions can be drawn from the history of these investigations; in addition, their efficiency, scale of application, and their perspectives are also discussed. Development and results achieved in electric, time and frequency domain electromagnetic methods and deep magnetic sounding are summarized.

2. Electric and electromagnetic prospecting

2. 1. A piece of history

The application of electrical and electromagnetic methods to oil and gas prospecting is discussed.

Nowadays only few people know that geoelectrical prospecting, primarily the direct current resistivity method, played the dominant role in geophysics applied to oil and gas prospecting before World War II. In fact, between 1932 and 1935 the Oil Ministry of the Soviet Union had about 50 field groups that used the resistivity method, but only 5 to 10 seismic groups. After the rapid progress experienced in the 1930s, however, the activity in resistivity prospecting decreased due to the limitations of direct current (cumbersome equipment, screening caused by high resistivity layers). Thus, electrical prospecting lost its importance and gave way to seismics with its higher resolution and processing potential. In the early 1950s the number of electric exploration groups working in regions of hydrocarbon potential in the Soviet Union was close to zero. Renewal of electrical prospecting needed innovative ideas. Three novel methods based on the use of electromagnetic fields varying with time were suggested:

1) Frequency sounding — FS [KRAJEV 1941, TIKHONOV 1950]. The frequency response of the earth determined by means of an artificial multifrequency electromagnetic field is inverted into a geoelectrical section.
2) Transient sounding — TS [TIKHONOV 1946, SHEINMANN 1947]. The time response of the earth determined by means of a series of artificial electromagnetic impulses is inverted into a geoelectrical section.
3) Magnetotelluric sounding — MTS [TIKHONOV1950, CAGNIARD 1953]. The earth's impedance determined by means of the natural electromagnetic field is inverted into a geoelectrical section.

In addition, the old idea of the telluric current method — TM [SCHLUMBERGER 1920, 1939] was also renewed. In tellurics the electric component of

the earth's response to the natural electromagnetic field is studied and a qualitative or even quantitative representation of basement topography can be obtained if there is a resistivity contrast between the basement and the overlying formations.

All these ideas were realized in the Soviet Union in the 1950s and 1960s [VANYAN, DMITRIEV, SIDOROV, KULIKOV, BERDICHEVSKY]. The rapid introduction and the scale of routine application of these new geoelectric methods were impressive. About 150 TM, TS and MTS groups worked in 1965 and the area covered by geoelectric surveys reached $3 \cdot 10^6$ km^2. Such activity could be observed until the early 1980s. During this period electric prospecting methods contributed to the construction of tectonic maps of regions having hydrocarbon potential, and were responsible for detecting numerous local elevations. The most important results were obtained in Siberia, mainly by magnetotellurics. A highly spectacular outcome of electric prospecting was the discovery of the famous Urengoy gas field (Western Siberia) which is connected to an uplift of Paleozoic rocks revealed by MTS.

Recently electric prospecting has had to cope with new problems. The challenge for geophysicists is to search for oil and gas reservoirs of non-structural type. It seems that existing capabilities of electric and electromagnetic methods which proved to be useful in regional structural studies, are not sufficient to solve these new tasks. Therefore, this kind of activity has decreased in many countries in the world. At the same time, intensive development of new approaches opening new horizons in electric prospecting, has continued in the Soviet Union. Transient and frequency soundings (including induced polarization measurements) have come to the forefront due to their higher resolution. It can be said that electric prospecting has overcome the crisis in its utilization in the Soviet Union. In 1992 we had 25 to 30 MTS and 50 TS and FS teams.

2. 2. *Magnetotelluric sounding* [VOZOFF 1982, OBUKHOV et al. 1983, SAVINSKY 1983, SAFONOV 1988, NOVIKOV et al. 1992, BERDICHEVSKY, DIMITRIEV 1992]

2. 2. 1. *Characteristic features of MT processing in the Soviet Union*

Mathematical filters are applied to the spectral analysis of magnetotelluric variations. The impedance tensor is determined from narrow-band telluric and magnetic oscillations using the method of least squares. Both the stability and plausibility of results obtained can be checked by evaluating the misfits $|E_x - Z_{xx}H_x - Z_{xy}H_y|$, $|E_y - Z_{yx}H_x - Z_{yy}H_y|$ and comparing the impedance matrix with inversion of the admittance matrix. Robust statistics and Gamble's remote reference magnetotellurics [GAMBLE 1978] are used to suppress instrument and industrial noise. If observations are carried out simultaneously at moving

and fixed stations, the favourable time intervals of low model noise can be chosen. In this way an accuracy of 2 to 5% in the modulus of the impedance components can be achieved. Finally, the principal values Z_P^+, Z_P^- of impedance tensor determined by Eggers' eigenstate technique are transformed into principal apparent resistivity curves ρ_P^+, ρ_P^- [EGGERS 1982].

Great importance is devoted to the analysis of MTS distortions caused by lateral inhomogeneities. MTS interpretation starts with diagnostics of lateral effects. Some simple transformations are used which allow one to eliminate these effects. Geological noise caused by small subsurface inhomogeneities is smoothed by spatial filtering.

NOVIKOV, BERDICHEVSKY et al. [1992] elaborated the MTM(at) system for space and frequency analysis and transformation of MT data that includes the experience gained in magnetotellurics all over the world. In this context analysis means determination of space and frequency characteristics that enable us to estimate the degree of horizontal inhomogeneity of the medium, to locate geoelectric structures, to outline their form, and to determine the strike. The transformation consists of apparent resistivity calculations and construction of geoelectric pseudo-profiles, sections and maps that provide a qualitative image of the electric conductivity distribution within the earth. The system includes both traditional techniques (e.g. the Niblett transform or amplitude polar diagrams) and the latest display tricks (e.g. phase polar diagrams that can be used to distinguish galvanic and inductive effects and show the effects of deep structures without near surface distortions, the Vozoff, Berdichevsky tippers that provide a more visual and distinct image of geoelectric structure than the traditional induction arrows, and the BAHR [1988] decomposition that separates near surface and deep effects).

The capabilities of the MTM(at) system are illustrated by Figs. 1. and 2.

Fig. 1 shows the model with a near surface 3-D inhomogeneity of lower conductivity and a deep 2-D inhomogeneity of higher conductivity. The near surface and deep inhomogeneities have different strikes. The amplitude polar diagrams are affected by the near surface inhomogeneity (even at very low frequencies) while phase diagrams reflect the orientation of the deep inhomogeneity. It is stressed that polar diagrams offer the simplest way of separating near surface and deep effects.

Fig. 2 shows the model with a near surface 3-D inhomogeneity of higher conductivity. The model provides an opportunity to compare the Vozoff-Berdichevsky tippers with induction arrows. The tipper is based on maximizing $|H_z| / \sqrt{|H_x|^2 + |H_y|^2}$. Its magnitude is equal to the norm $\| \hat{W} \|$ of the Wiese-Parkinson matrix $\hat{W} = [W_{zx}\ W_{zy}]$ while its orientation coincides with the magnetic eigenfield of the matrix. In addition, the phase of matrix invariant $\Psi = \arg \sqrt{W_{zx}^2 + W_{zy}^2}$ is also determined. It seems that tippers are more sensitive than induction arrows. The informative pattern is given by phases: they reflect the relationship between active and reactive excessive currents (if Ψ is close to $\pi/2$, the reactive currents are dominant).

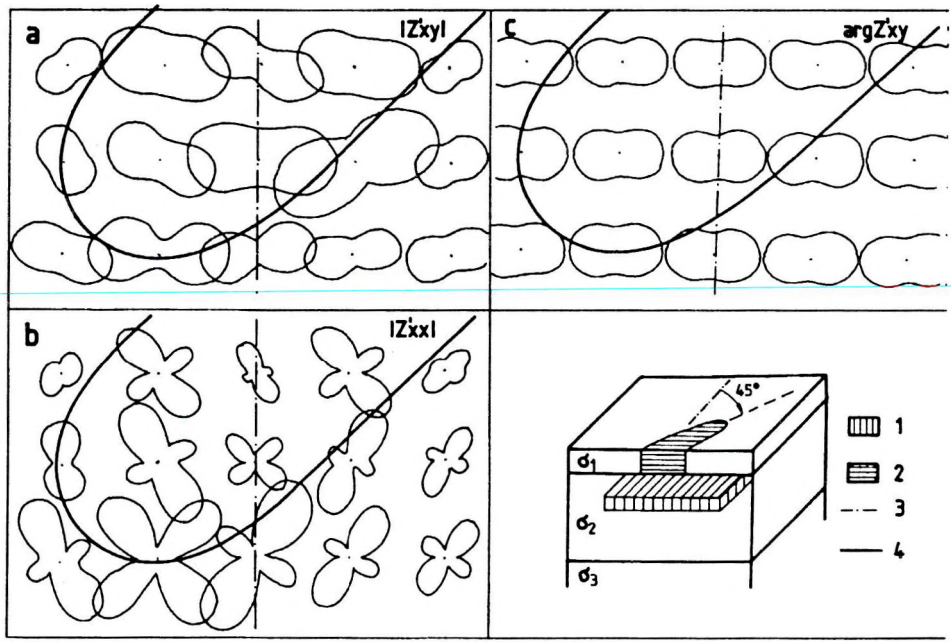

Fig. 1. Impedance polar diagrams for the model with near surface 3-D and deep 2-D inhomogeneity. a, b—amplitude diagrams of $|Z'_{xy}|$, $|Z'_{xx}|$; c—phase diagram of arg Z'_{xy}; 1—inhomogeneity of higher conductivity; 2—inhomogeneity of lower conductivity; 3—axis of deep 2-D inhomogeneity; 4—contour of near surface 3-D inhomogeneity

1. ábra. Felszínközeli 3-D és mély 2-D inhomogenitást tartalmazó modell impedancia polár diagramja. a, b—a $|Z'_{xy}|$, $|Z'_{xx}|$ amplitudó diagramja; c—az arg Z'_{xy} fázis diagramja; 1—nagyobb vezetőképességű inhomogenitás; 2—kisebb vezetőképességű inhomogenitás; 3—a mély 2-D inhomogenitás tengelye; 4—a felszínközeli 3-D inhomogenitás körvonala

The MTM(at) system has a clear algorithmic base and helps
a) to construct a normal conductivity distribution,
b) to evaluate the degree of lateral inhomogeneity,
c) to locate the geoelectrical structures,
d) to classify them according to their dimensions,
e) to outline zones of low and high conductivity,
f) to construct the interpretation model,
g) to choose the inversion strategy.

The inverse magnetotelluric problem is unstable and, therefore, it is ill-posed. It means that any arbitrarily small error in the initial MT data may cause an arbitrarily large error in their inversion, i.e. in the electric conductivity distribution. The inversion is feasible provided that a priori information about the geoelectric structure of a region provides limits: 'you have to know generally what is to be sought and where it is to be sought'. It is evident that the effectiveness of MT interpretation strongly depends on the available amount

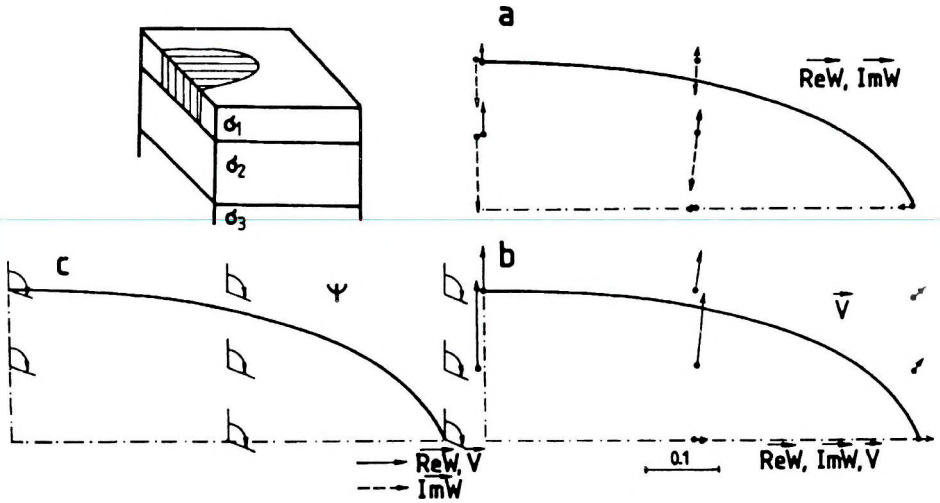

Fig. 2. Tippers and induction arrows for the model with near surface 3-D inhomogeneity of higher conductivity (hatched). a—real and imaginary induction arrow; b—Vozoff-Berdichevsky tipper; c—phase

2. ábra. Nagyobb vezetőképességű felszínközeli 3-D inhomogenitást tartalmazó modellre vonatkozó tipperek és indukciós nyilak. a—valós és képzetes indukciós nyil; b—Vozoff-Berdichevsky tipper; c—fázis

of a priori geological-geophysical information. If there is no a priori information we can obtain only either one of the equivalent models which might be very different from the real structure, or a model with a significantly smoothed conductivity distribution neglecting essential details.

The corner-stone of MT interpretation is the theory of ill-posed problems elaborated by TIKHONOV, ARSENIN [1976], GONCHARSKY [1987], LAVRENTJEV et al. [1980], DMITRIEV [1987].

Within the Tikhonov theory there are two methods of solving the inverse magnetotelluric problem.

The first method is to select a set of models (compactum) and to find within this set a model which best agrees with the a priori information and provides the misfit not exceeding the errors of initial MT data. An example of this approach is regularized fitting.

The second method includes the construction of an approximate inverse operator which acts as a spatial filter and provides a smoothed geoelectric pattern. An example of this approach is the Backus-Gilbert method [BACKUS, GILBERT 1968].

Algorithmically the two methods are based on making an approximate solution more and more accurate by reducing the errors in data. Correctness of the solution results from its fitting to the a priori information. The choice of a specific computational scheme is a question of technology (computer type, CPU time, convenience of entering a priori information, etc.). Whereas some of us prefer the deterministic scheme, others prefer the probabilistic one. It is hardly worth arguing which of the schemes is better: algorithmically they are equivalent.

If lateral resistivity variations are rather slow and the difference between the principal apparent resistivities is sufficiently small, the MT curves can be interpreted using 1-D models at every station. Here the *S*-method developed by DMITRIEV [1987] is popular. The method divides the inversion (non-linear ill-posed problem) into two parts: the *S*-transformation that provides stable integral characteristics $S(z) = \int_0^z \sigma(z)\, dz$ (non-linear well-posed problem) and σ-inversion that reduces to differentiating *S* (linear ill-posed problem). An attractive feature of the *S*-method is that *S*-transformation characterizes the whole set of equivalent models facilitating the input of a priori information and estimation of the limits of equivalence. The results obtained by 1-D inversion should be checked by 2-D and 3-D modelling specifying the influence of lateral inhomogeneities. If this checking does not provide acceptable results we have to reject the 1-D interpretation and change to 2-D or 3-D inversion.

The 2-D inversion is carried out by automatic or interactive (intuitive) fitting. Both E- and H-polarization modes are used. E-polarization data reflect the effects of deep structures covered by resistive screening layers. H-polarization data provide information about the shallow layers and allow one to determine the resistivity of the screening layers as well. Thus, bimodal inversion is the most effective. In 3-D inversion we use the thin-sheet approximation [ZINGER, FAINBERG 1985] and a quasi-1-D technique that reduces the 3-D inversion to an iterative sequence of 1-D inversions corrected by 3-D misfit [DMITRIEV 1987, BARASHKOV et al. 1988, OLDENBURG 1988].

2. 2. 2 MT practice: Case histories

Fig. 3 gives the tectonic map of the *Moscow syneclise** constructed from MTS data. The map shows the relief of the crystalline basement and numerous small uplifts detected by the telluric current method. Several uplifts were

* Syneclise: A negative or depressed structure of the continental platform; it is of broad, regional extent (tens to hundreds of thousands of square kilometres) and is produced by slow crustal downwarp during the course of several geologic periods. The term is used mainly in the Russian literature, e.g. the Caspian syneclise [BATES R. L., JACKSON J. A. (editors): Glossary of geology, American Geological Institute, 1980, p. 633.]

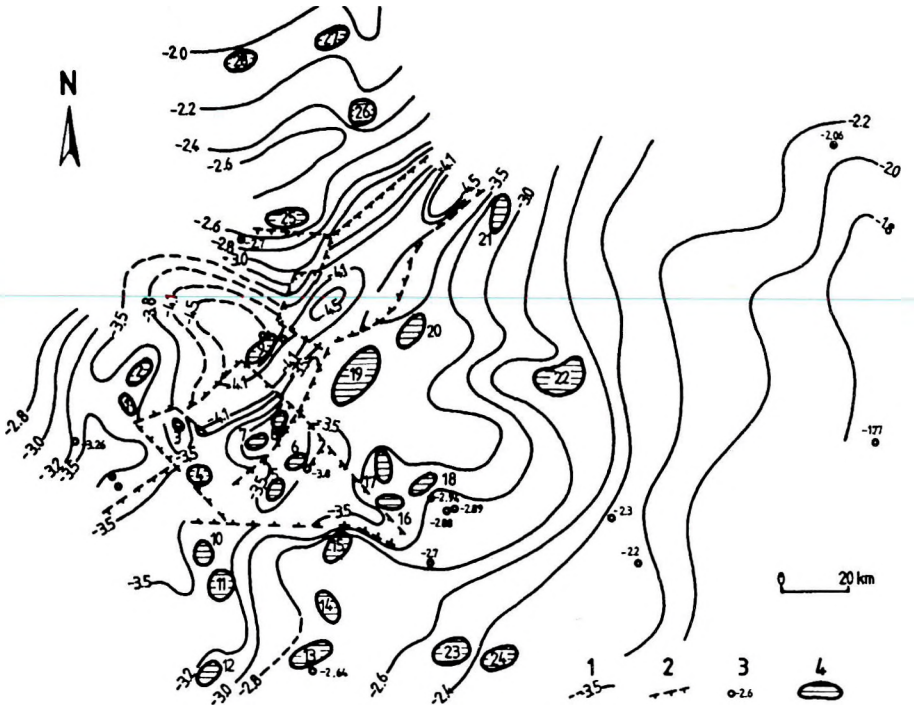

Fig. 3. Tectonic map of the Moscow syneclise [according to SHEINMANN]. 1—contour of depth to the basement (km); 2—tectonic disruption; 3—well with depth to the basement; 4—elevations based on magnetotellurics

3. ábra. A Moszkvai-szineklízis tektonikai térképe [SHEINMANN nyomán]. 1—az aljzatmélység szintvonala (km); 2—tektonikai vonalak; 3—fúrás az aljzat mélységével; 4—magnetotellurikából kapott kiemelkedések

confirmed by seismics and drilling too. The accuracy of MTS interpretation is rather high. It can be seen in *Table I* that the difference between the MTS and drilling data does not exceed 5 to 10 %. Thus, the electrical prospecting was very helpful in studying this huge area.

The efficiency of magnetotellurics was observed in *Western Siberia* as well. The bulk of the oil reserves in Russia has been found in this region, especially in its northern part. Between 1960 and 1975, telluric and magnetotelluric groups investigated an area of 10^6 km^2 and became pioneers in discovering some oil and gas fields (e.g., the Shain oil field or the Urengoy gas field). A significant amount of information about the topography of the Paleozoic basement and resistivity of the Mesozoic sediments has been collected.

Well identification	Depth to basement (in km)		Difference (per cent)
	from drilling	from magnetotellurics	
Dyakonov-1	3.13	3.15	0.5
Dyakonov-3	3.34	3.2	1.0
Galich	3.8	3.4	11.0
Neya-1	3.1	3.2	3.0
Neya-3	3.0	3.15	5.0
Rozhdestvin	2.45	2.65	8.0
Poshekhon	2.94	2.95	0.0
Tot'ma	2.79	2.8	0.0
Lezha	3.49	3.65	4.5
Tarnog	2.19	2.35	7.0
Orekhov	3.45	3.4	1.5

Table I. Differences in depth to the basememnt from drilling and magnetotellurics
I. táblázat. A fúrásból és magnetotellurikából meghatározott aljzatmélységek eltérése

Fig. 4 shows a geoelectric cross-section typical of the *Urengoy region.* Magnetotellurics and seismics give almost the same basement relief at depths of about 6 to 8 km. The geoelectric boundaries in sediments correlate well with the seismic ones. The lateral changes in sediment resistivity reflecting lithologic variations are clearly seen. *Fig. 5* illustrates the scale of magnetotelluric surveys applied in the oil industry in Western Siberia. It shows the conductance of the unconsolidated sediments in the northwestern regions (500 000 km^2). The contour line of 850 S outlines the zone where the pre-Jurassic sediments wedge out and this information is of great importance because oil fields occur mainly in this zone.

Interesting results were obtained by telluric and magnetotelluric methods east of this region, on the *Siberian platform* (Tungus and Vilyuis syneclises, Aldan anteclise*) as well. Here the occurrence of oil and gas fields is connected with the Mesozoic and Paleozoic sediments. *Fig. 6* is the schematic map of the

* Anteclise: A positive or uplifted structure of the continental platform, it is of broad, regional extent (tens to hundreds of thousands of square kilometres) and is produced by slow crustal upwarp during the course of several geologic periods. The term is used mainly in the Russian literature; e.g. the Belorussian anteclises of the Volga-Urals. Also spelt: anticlise [BATES R. L., JACKSON J. A. (editors): Glossary of geology, American Geological Institute, 1980, p.26.]

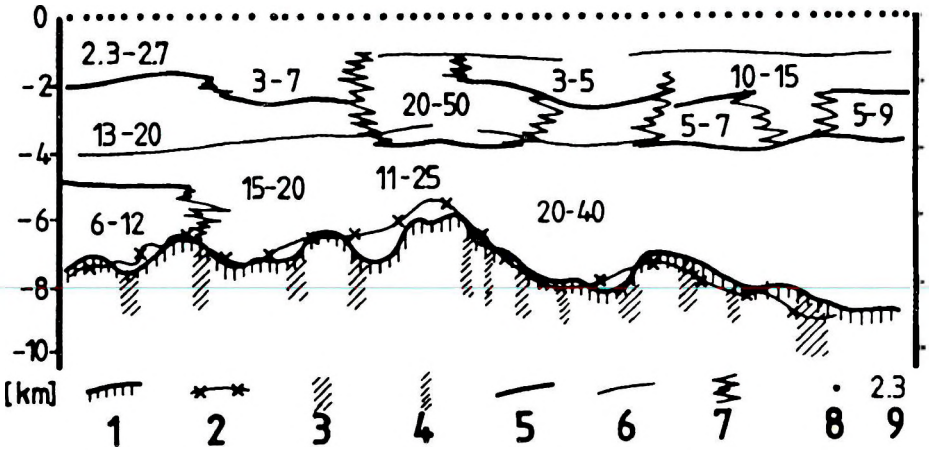

Fig. 4. Geoelectric section along a profile in Nadim-Urengoy region [according to SISOEV]. 1—relief of the basement from MTS data; 2—relief of the basement from seismics; 3—tectonic disruption from seismics; 4—tectonic disruption from magnetotellurics; 5—geoelectric boundary; 6—seismic reflection horizon; 7—zones of sudden changes in conductivity; 8—MT sounding; 9—resistivity (ohmm)

4. ábra. A Nadim-Urengoy terület egy szelvényének geoelektromos metszete [SISOEV nyomán]. 1—az aljzat domborzata MTS adatok alapján; 2—az aljzat domborzata szeizmikus adatok alapján; 3—tektonikai vonal szeizmika alapján; 4—tektonikai vonal magnetotellurika alapján; 5—geoelektromos réteghatár; 6—szeizmikus reflexiós szint; 7—hirtelen vezetőképesség változás zónái; 8—MT szondázás; 9—fajlagos ellenállás (ohmm)

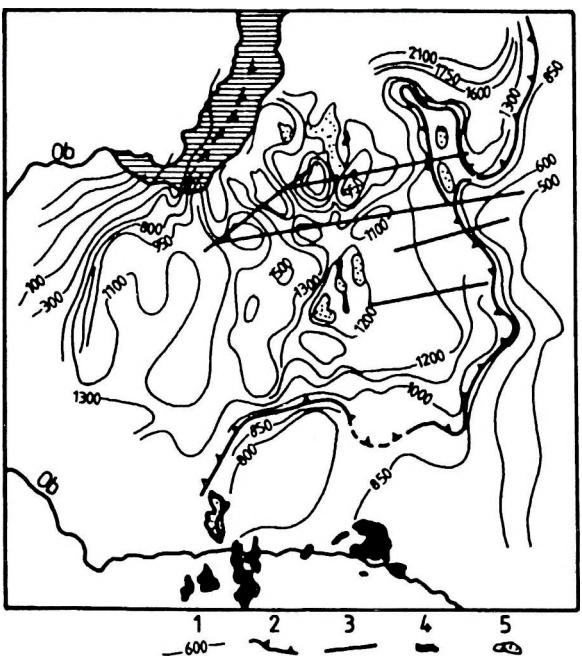

Fig. 5. Map of the sediment conductance in the northwestern part of the West Siberian plate [according to KOPELEV, SISOEV]. 1—isoline of conductance (siemens); 2—boundary of pre-Jurassic sediments; 3—MTS profile; 4—oil field; 5—gas field

5. ábra. Az üledék összegzett hosszirányú vezetőképességének térképe a Nyugat-Szibériai-lemez északnyugati részén [KOPELEV, SISOEV nyomán]. 1—az összegzett hosszirányú vezetőképesség izovonala (siemens); 2—a juránál idősebb üledékek elterjedésének határa; 3—MTS szelvény; 4—olajmező; 5—gázmező

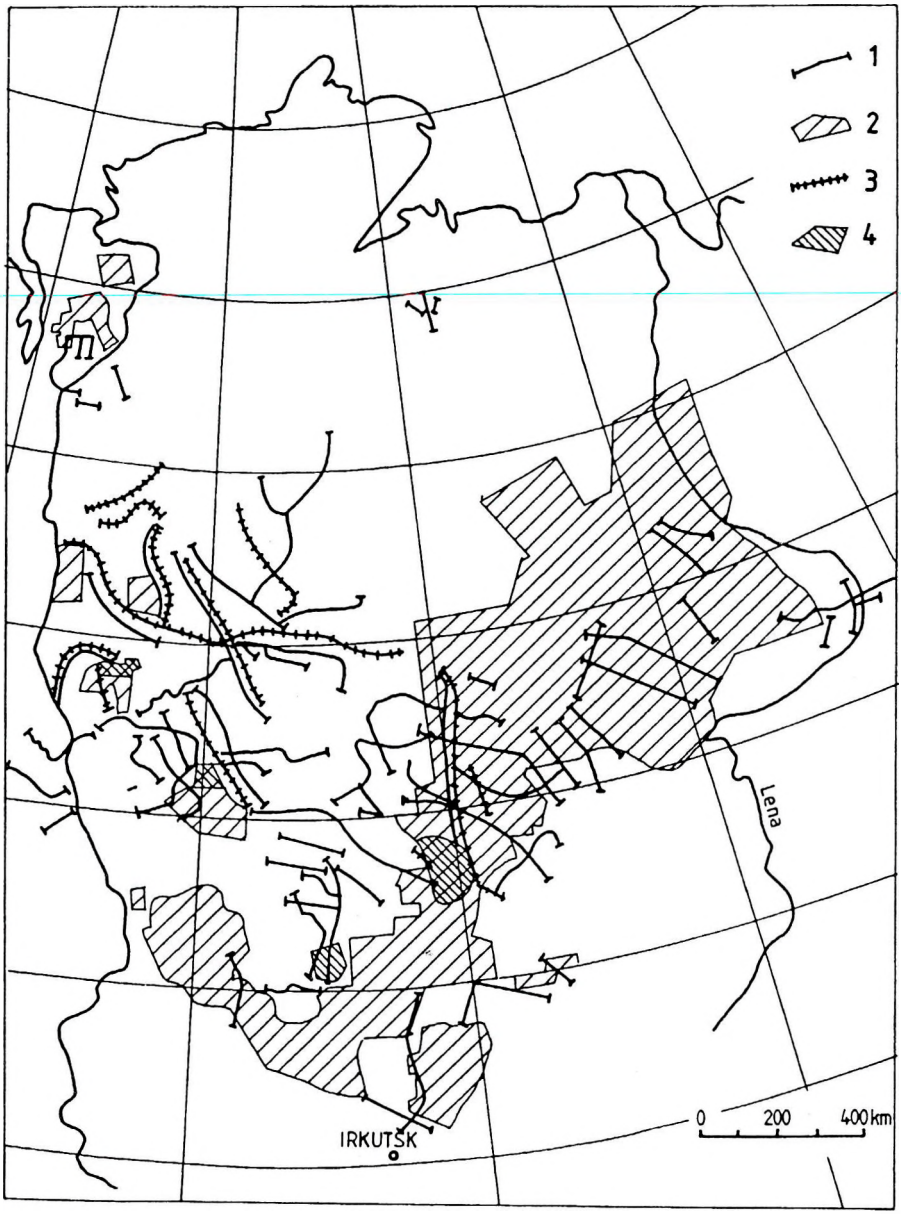

Fig. 6. Schematic map of the geoelectric surveys in Eastern Siberia [according to JAKOVLEV]. Magnetotelluric surveys: 1—traverse; 2—area. Transient soundings: 3—traverse; 4—area

6. ábra. A Kelet-Szibériában végzett geoelektromos kutatások vázlatos térképe [JAKOVLEV nyomán]. Magnetotellurikus kutatások: 1—szelvénymenti; 2—területi; Tranziens szondázások: 3—szelvénymenti; 4—területi

geoelectric investigations carried out in *Eastern Siberia*. Magnetotelluric surveys have covered an area of about 10^6 km^2. Almost the whole area is permafrost.

It is noteworthy that the geological structures revealed by MTS data are close to the seismic ones in many regions of Eastern Siberia. This is demonstrated by three examples. *Fig. 7* shows the seismic and geoelectric boundaries along a profile crossing the *Linden depression* (Vilyuisk syneclise). It can be seen that these boundaries practically coincide in the Upper Paleozoic se-

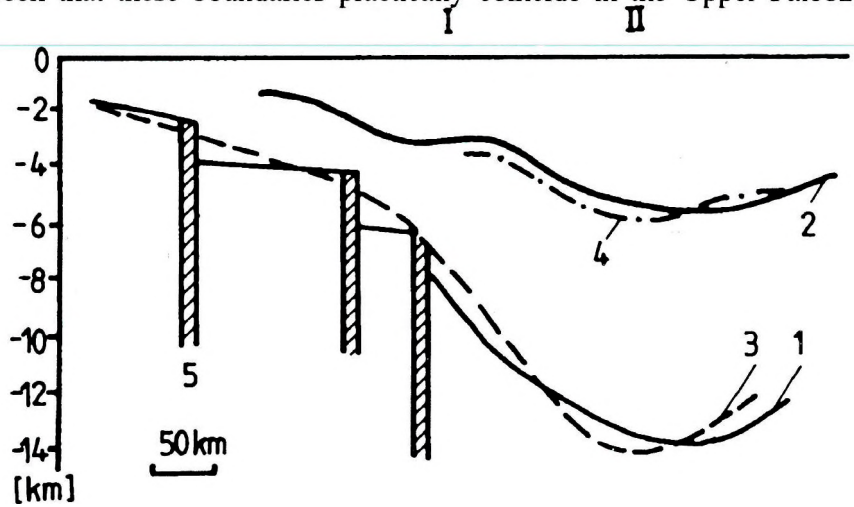

Fig. 7. Geophysical section along the profile Djelinda-Muna [according to JAKOVLEV]. I—Khapchagay elevation; II—Linden depression; 1—basement relief from seismic data; 2—seismic horizon in Permian; 3—basement relief from MTS data; 4—top of conductive Paleozoic layer from MTS data; 5—tectonic disruption from seismics

7. ábra. Geofizikai metszet a Djelinda-Muna szelvény mentén [JAKOVLEV nyomán]. I—Khapchagay kiemelkedés; II—Linden süllyedék; 1—az aljzat domborzata szeizmikus adatok alapján; 2—szeizmikus szint a permi képződményekben; 3—az aljzat domborzata MTS adatokból; 4—a jól vezető paleozoós réteg felszíne MTS adatok alapján; 5—tektonikai vonal szeizmika alapján

quence. The same can be said about the basement topography. The next example is given in *Fig. 8*. The profile crosses the *Igiattan* and *Linden depressions*. Similarly to the previous case, the geoelectric and seismic boundaries coincide quite well in the Upper Paleozoic sequence. The geoelectric boundary identified as the basement surface follows the seismic horizon but exaggerates the local structures in the Linden depression. *Fig. 9* shows the last example. This is part of a telluric field intensity map. Minima of telluric intensity correspond to the uplifts of the conductive Cambrian layer appearing in the seismic horizon as well.

Results of all magnetotelluric surveys were summarized in the tectonic map of the eastern part of the *Siberian platform* (*Fig. 10*). The map shows the main structures of this region and numerous local uplifts. The most significant

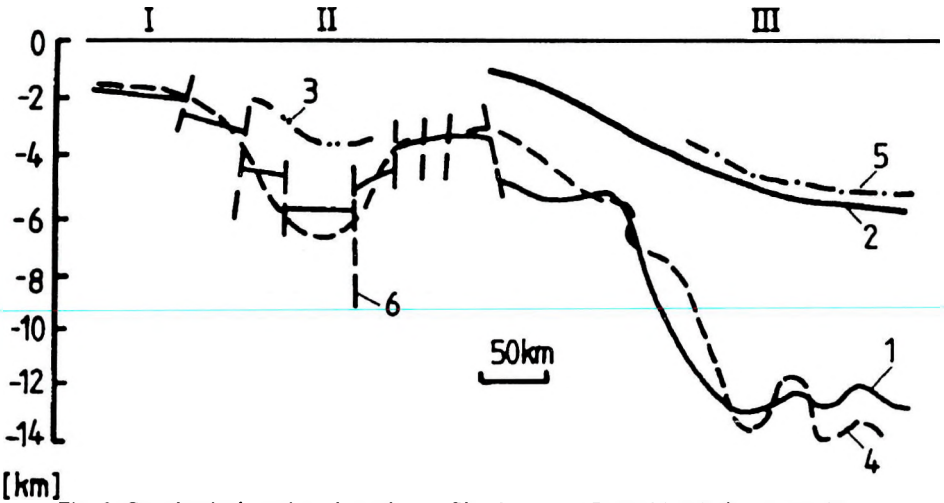

Fig. 8. Geophysical section along the profile Oczuguy-Botuobia Linden [according to JAKOVLEV]. I—Mirmin dome; II—Igiattan depression; III—Linden depression; 1 —basement relief from seismics; 2—seismic horizon in Permian; 3—in Cambrian; 4—basement relief from MTS data; 5—top of conductive Paleozoic sediments from MTS data; 6—fault from seismic data

8. ábra. Geofizikai metszet az Oczuguy-Botuobia-Linden szelvény mentén [JAKOVLEV nyomán]. I—Mirmin boltozat; II—Igiattan süllyedék; III—Linden süllyedék; 1—az aljzat domborzata szeizmika alapján; 2—szeizmikus szint a permi képződményekben; 3—szeizmikus szint a kambriumi képződményekben; 4—az aljzat domborzata MTS adatok alapján; 5—a jól vezető paleozoós üledékek felszíne MTS adatok alapján; 6—vető szeizmikus adatok alapján

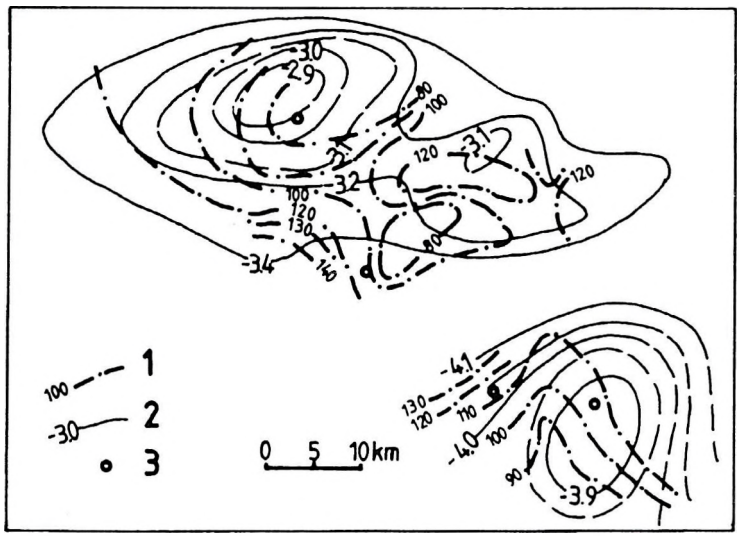

Fig. 9. Map of telluric field intensity in Yakutia [according to JAKOVLEV]. 1—contour of telluric intensity (conventional units); 2—contour of a seismic horizon in Permian formations (km); 3—location of reference MT soundings

9. ábra. A tellurikus intenzitás térképe Jakutiában [JAKOVLEV nyomán]. 1—a tellurikus intenzitás izovonala (konvencionális egység); 2—egy permi formáción belüli szeizmikus szint szintvonala (km); 3—MT szondázási alappontok helye

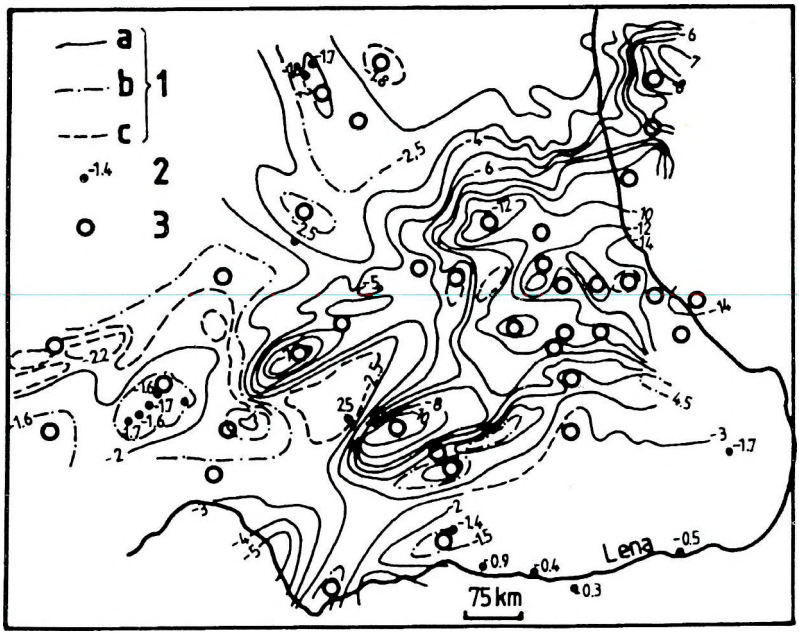

Fig. 10. Tectonic map of the eastern part of the Siberian platform [according to JAKOVLEV]. 1—contour of the depth to the basement (km); a—principal; b—intermediate; c—supposed. 2—depths to the basement (km) from drilling; 3— local structures

10. ábra. A Szibériai-tábla keleti részének tektonikai térképe [JAKOVLEV nyomán]. 1—az aljzatmélység szintvonala (km); a—legmegbízhatóbb; b—közepes megbízhatóságú; c—feltételezett; 2—aljzatmélység (km) fúrás alapján; 3—lokális szerkezetek

result of these surveys is that highly fractured Paleozoic limestones have been detected in the Vilyuis syneclise resulting in a new oil and gas perspective.

Sakhalin is the scene of the next case history. For many years MT sounding has been the main geophysical method used for regional investigations in the island. *Fig. 11* presents one of the results obtained, viz. the map of the thickness of the unconsolidated sediments. The largest thicknesses can be found in the depressions XV, XVI and XVII. These zones are the most promising ones. *Fig. 12* shows a part of the MT interpretation, this being the geoelectric cross-section along the eastern part of the island. The major tectonic elements and even the lithologic boundaries can be seen here. All these results serve to evaluate the potential of oil and gas occurrence.

Magnetotellurics has been most efficient in searching for oil and gas fields that are governed by tectonics. Recently oil and gas prospecting has been directed toward the fields of non-structural type in many regions of our country, and the geologists have to cope with more subtle lithologic problems. In Western Siberia, for instance, the lithologic changes in thin Jurassic layers (100 to 250 m) at a depth of about 3 km are to be studied and the problem is beyond the resolution of magnetotellurics. Therefore, the magnetotelluric surveys have

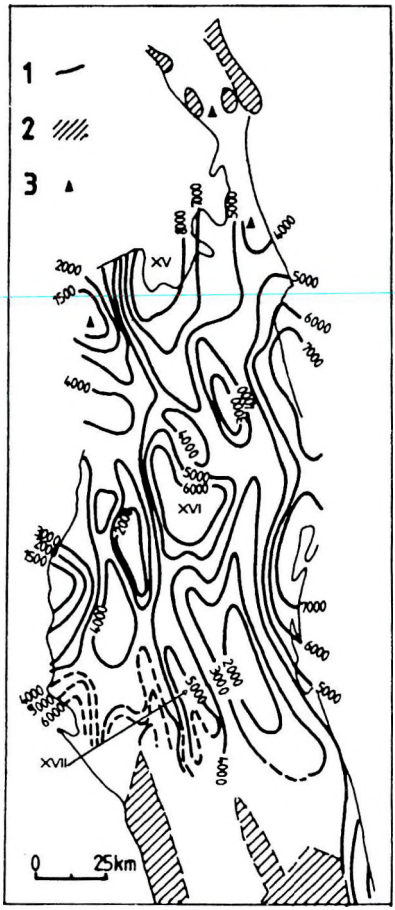

Fig. 11. Map of sediment thickness in North Sakhalin [according to ALPEROVICH]. 1—isopach of the sediments (metres); 2—pre-Neogene outcrops; 3—wells penetrating the pre-Neogene

11. ábra. Az üledékvastagság térképe Észak-Szachalinon [ALPEROVICH nyomán]. 1—az üledékek izopach vonala (m); 2—neogénnél idősebb kőzetek kibúvásai; 3—a neogénnél idősebb képződményt elérő fúrások

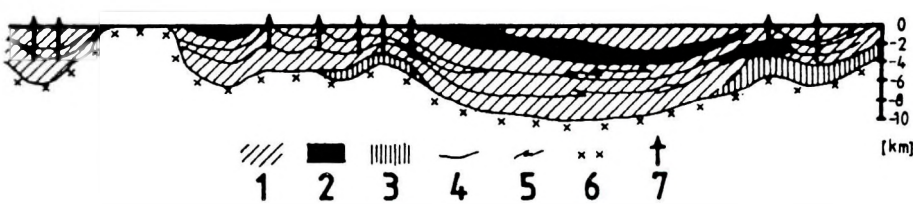

Fig. 12. Geoelectric section along the eastern part of Sakhalin [according to ALPEROVICH]. 1—argillaceous sediments, ρ <10 ohmm; 2—sandy-argillaceous sediments, ρ ~ 20-30 ohmm; 3—sandstone, ρ > 30 ohmm; 4—stratigraphic boundaries; 5—lithologic boundaries; 6—basement; 7—drilling

12. ábra. Geoelektromos szelvény Szachalin keleti részén keresztül [ALPEROVICH nyomán]. 1—agyagos üledékek, ρ>10 ohmm; 2—homokos-agyagos üledékek, ρ~20-30 ohmm; 3—homokkő, ρ> 30 ohmm; 4—sztratigráfiai határok; 5—litológiai határok; 6—aljzat; 7—fúrás

been stopped in this region. It might be of interest, however, to discuss some recent results obtained in areas where magnetotellurics has proved to be successful.

Rich oil and gas fields have been discovered in the *North Caspian Basin.* The region is characterized by diapiric structures and the reservoirs that are to be searched for lie beneath a salt cover of varying thickness. Two typical examples from the results obtained here by MT soundings are presented. *Fig. 13* shows a smoothed geoelectric cross-section from the central part of the *Astrakhan anteclise.* The low resistivity zone (hatched) outlined at a depth of more than 4 km (i.e. beneath the salt cover) is of great interest because it is the zone of highest porosity. The next example (*Fig. 14*) shows the geoelectric structure of the slope of the Astrakhan anteclise as a set of vertical conductivity profiles. These outline zones of higher and lower conductivity. In the centre of this cross-section a downthrown part of the conductive sediments underlying the salt and bordered by faults can be seen. It is significant that this promising zone (of higher porosity?) is not reflected in seismic data. It is evident that magnetotellurics is a useful supplement to seismics in this region.

One more example is shown in *Fig. 15.* This is a geoelectric cross-section constructed from MT data in *Southwestern Turkmenistan.* Gas-condensate deposits are known in this region. Magnetotellurics has detected highly conductive zones in the hydrocarbon-bearing stratum that can be interpreted as the zones of increased water saturation favourable for gas deposits.

2.3. Transient sounding [SIDOROV 1985, TIKSHAEV 1984, NEBRAT 1990]

In contrast to the situation concerning magnetotelluric activities — which are on the decrease — the method of transient sounding has come to the foreground. The traditional approach using the principle of apparent resistivity is widely used. At the same time some non-traditional approaches have also appeared. It seems, however, that these are poorly known in the West. In view of this, it would be reasonable to discuss these approaches in more detail.

2. 3. 1 The S-transform

SIDOROV proposed that the transient electric or magnetic field, $E(t)$ or $B(t)$ be transformed into $S(z)$ where S is the conductance of layers affecting the field at the moment t; and z is their total thickness. The transformation is carried out by means of the equivalent model which replaces the layered medium with a thin sheet located in the non-conducting space. *Fig. 16* shows two S-profiles obtained near drillholes. They correlate well with the well-logging data, the inclined sections correspond to the layers of higher conductivity. In *Fig. 17* the geoelectric cross-section along a profile in the northwestern part of the *North*

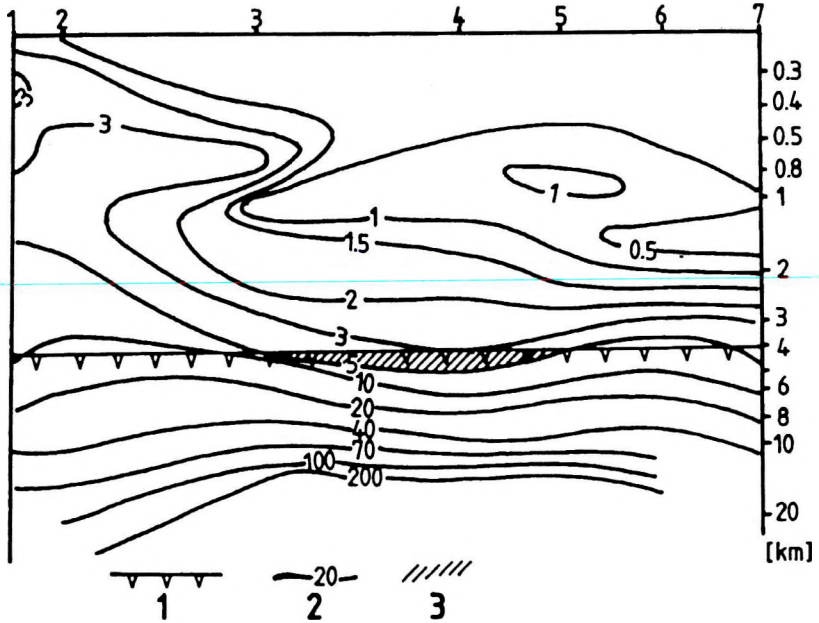

Fig. 13. Geoelectric section in the central part of the Astrakhan anteclise [according to GOLUBZOVA]. 1—bottom of salt; 2—contour of resistivity (ohmm); 3—zone of increased conductivity below the salt

13. ábra. Geoelektromos metszet az Asztrahány-anteklízis középső részén [GOLUBZOVA nyomán]. 1—a sóréteg alja; 2—a fajlagos ellenállás izovonalai (ohmm); 3—nagyobb vezetőképességű zóna a sóréteg alatt

Caspian depression can be seen. Changes in the conductance of the layers overlying the salt reflect the salt topography. Changes in the conductance of the layers underlying the salt are more interesting because they reflect the relations between the terrigenous and carbonate components in the rocks having hydrocarbon potential. It is worth mentioning one episode from the history of this method. Four soundings revealed the topography of salt in the Altatin area (in the North Caspian depression) but seismics provided different data. Moreover, these soundings outlined terrigenous layers within the salt body. Geologists did not accept this assumption but some years later drilling confirmed the interpretation of the geoelectric data.

2.3.2. The method of multiple overlapping

TIKSHAEV [1984] suggested a special technique of *S*-transformation based on a series of measurements with overlapping receivers (loops or grounded dipoles). Spatial averaging smooths out the field distortions caused by local lateral inhomogeneities and provides high measurement stability. This makes

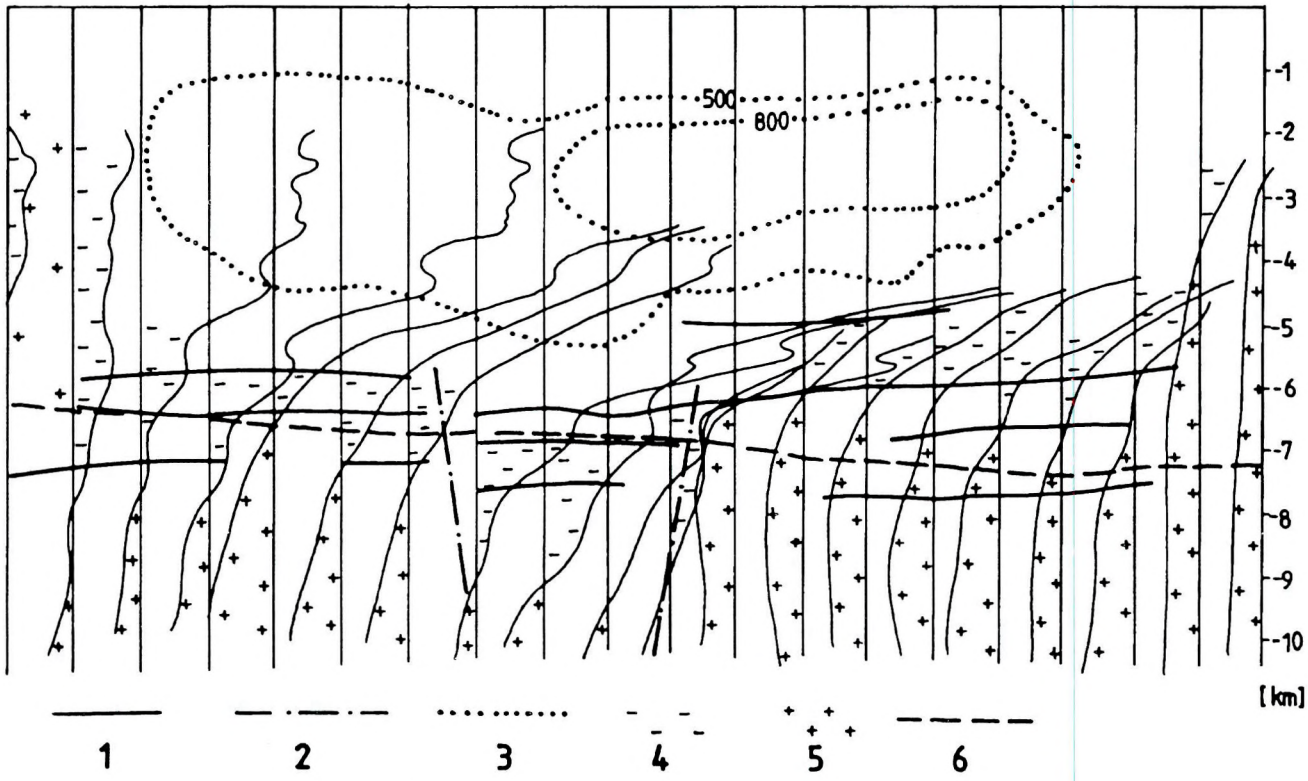

Fig. 14. Geoelectric section on the slope of the Astrakhan anteclise [according to PLAKHOV]. 1—conductivity profile; 2—tectonic disruption; 3—contour of conductivity (10^{-3} S/m); 4—zone of increased conductivity $\sigma > 0.1$ S/m; 5—zone of decreased conductivity $\sigma < 0.1$ S/m; 6—seismic horizon P_1

14. ábra. Geoelektromos metszet az Asztrahány-anteklízis lejtőjén [PLAKHOV nyomán]. 1—vezetőképesség szelvény; 2—tektonikai vonal; 3—vezetőképesség izovonala (10^{-3} S/m); 4—nagyobb vezetőképességű zóna, $\sigma > 0{,}1$ S/m; 5—kisebb vezetőképességű zóna, $\sigma > 0{,}1$ S/m; 6—P_1 szeizmikus szint

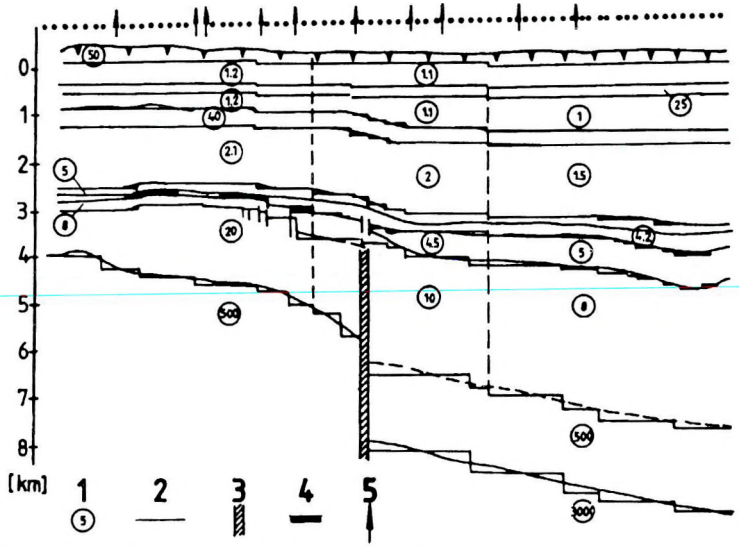

Fig. 15. Geoelectric section in Southwestern Turkmenistan [according to CHERNJAVSKY]. 1—resistivity (ohmm); 2—geoelectric boundary; 3—tectonic disruption; 4—zone of increased water saturation; 5—drilling

15. ábra. Geoelektromos metszet Délnyugat-Türkmenisztánban [CHERNJAVSKY nyomán]. 1—fajlagos ellenállás (ohmm); 2—geoelektromos határ; 3—tektonikai vonal; 4—megnövekedett víztelítettségű zóna; 5—fúrás

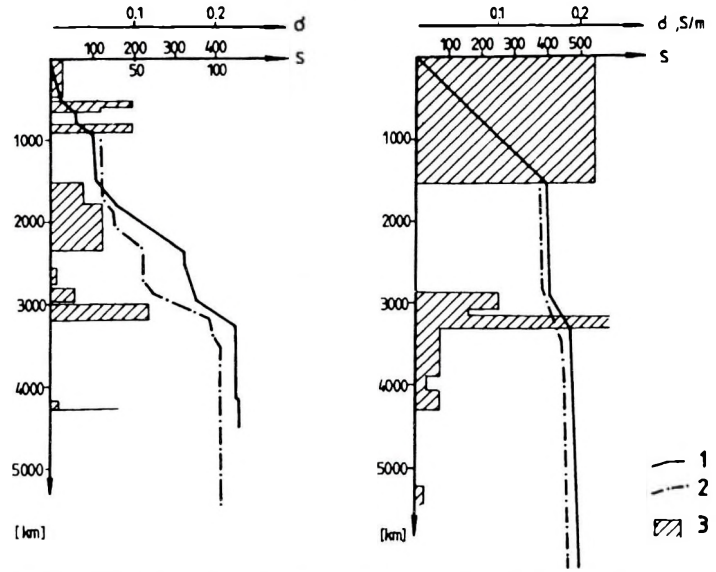

Fig. 16. Vertical profiles of conductance [according to SIDOROV]. 1—well-logging data; 2—data from transient sounding; 3—horizons of higher conductivity

16. ábra. Az összegzett hosszirányú vezetőképesség függőleges szelvényei [SIDOROV nyomán]. 1—mélyfúrásgeofizikai adatok; 2—tranziens szondázásokból kapott adatok; 3—nagyobb vezetőképességű szintek

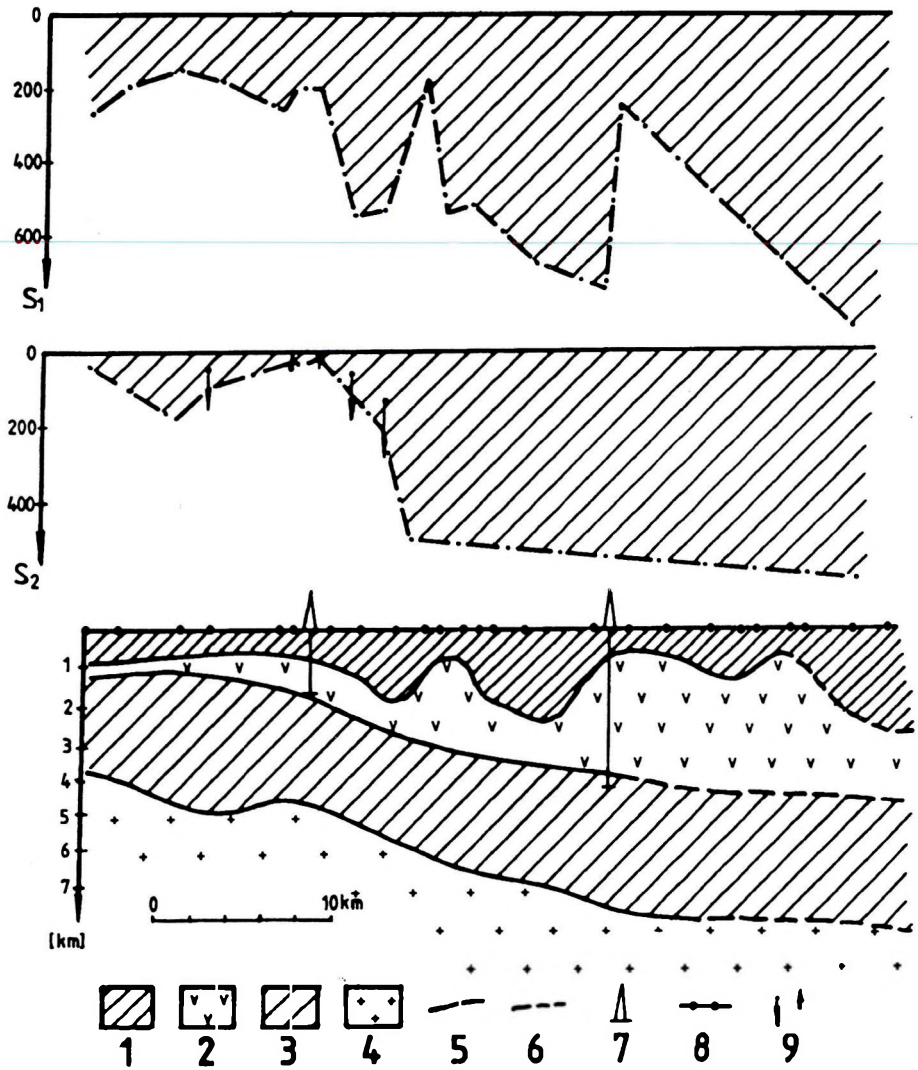

Fig. 17. Geoelectric section in the northwestern part of the North Caspian depression [according to SIDOROV]. 1—sediments overlying the salt; 2—salt; 3—sediments underlying the salt; 4—crystalline basement; 5—seismic horizon; 6—unreliable seismic horizon; 7—drilling; 8—transient sounding; 9—scattering of *S*-values; S_1—conductance of the layers overlying the salt; S_2—conductance of the layers underlying the salt

17. ábra. Geoelektromos metszet az Észak-Kaspi-süllyedék északnyugati részén [SIDOROV nyomán]. 1—a sóréteg felett települő üledékek; 2—sóréteg; 3—a sóréteg alatt települő üledékek; 4—kristályos aljzat; 5—szeizmikus szint; 6—bizonytalan szeizmikus szint; 7—fúrás; 8—tranziens szondázás; 9—az *S* értékek szórása. S_1— a sóréteg feletti rétegek összegzett hosszirányú vezetőképessége, S_2 —a sóréteg alatt települő rétegek összegzett hosszirányú vezetőképessége

it possible to determine a 'differential' conductivity such as $\sigma(z) = dS(z)/dz$. In order to reduce the range of conductivity variations the function $\tanh \sigma(z)$ is used for graphic representation.

Fig. 18 shows an example where the geoelectric section is plotted in such a manner. The similarity between the geoelectric and seismic sections is striking. It is reasonable to combine seismic and geoelectric sections and to correlate the seismic horizons with conductivity changes. This idea gives rise to 'seismoelectrostratigraphy', a method that is very efficient in outlining the highly porous zones. Even a joint parameter has been introduced that reflects variations both in velocity and resistivity, therefore it is sensitive to non-structural oil reservoirs. The method of multiple overlapping was successfully applied in the North Caspian region and in Eastern Siberia. Drilling confirmed the predicted reservoir characteristics of the carbonate rocks. Reef bodies were discovered and classified according to their hydrocarbon potential. Exploitable deposits have recently been discovered in two reefs.

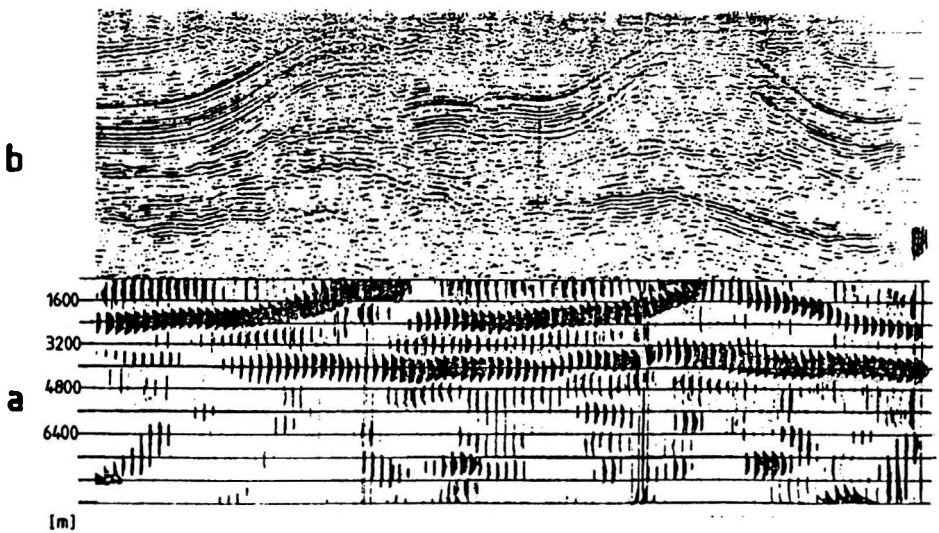

Fig. 18. Comparison of geoelectric and seismic sections [according to TIKSHAEV]. a—geoelectric section; b—seismic time section

18. ábra. Geoelektromos és szeizmikus szelvény összehasonlítása [TIKSHAEV nyomán]. a—geoelektromos metszet; b—szeizmikus időszelvény

2. 3. 3 The method of normalized second differences

NEBRAT proposed another approach providing a qualitative image of geoelectric structures. Data processing consists of three phases:

1) detection of fast field variations as a difference $\Delta F = F_s - F_l$ between two spline approximations, one with small steps (F_s), the other with large steps (F_l),
2) spatial averaging of ΔF and determination of the second differences $\Delta\Delta F = \Delta F - \Delta\bar{F}$ where $\Delta\bar{F}$ is the mean (median) value for all stations,
3) spatial averaging of $\Delta\Delta F$ and its normalization, $L = \Delta\Delta F / \Delta\Delta\bar{F}$ where $\Delta\Delta\bar{F}$ is the mean (median) value for all stations.

The method is widely used in marine prospecting. It is highly cost-effective because the electromagnetic observations are carried out simultaneously with seismic data acquisition (on the same ship). *Fig. 19* shows an electric time section of normalized second differences, together with the seismogeological section (*Black Sea*). The time section reflects rather well the main tectonic features of the region. *Fig. 20* shows another example from the same region. Here the zones of positive L that are outlined in the time interval 1.5–4.5 s correspond to the reef structures at a depth of about 2 to 3 km.

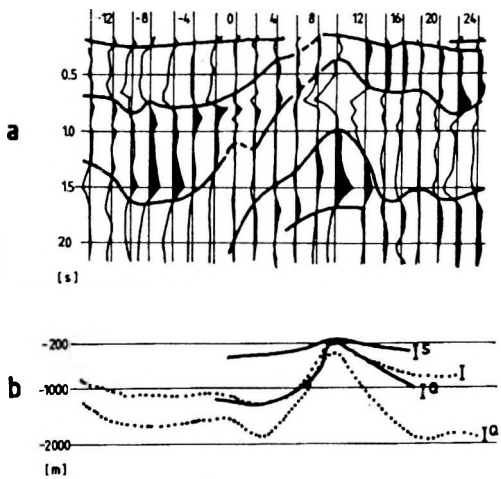

Fig. 19. Comparison of geoelectric and seismic sections [according to NEBRAT]. a—geoelectric time section; b—seismic section

19. ábra. Geoelektromos és szeizmikus szelvény összehasonlítása [NEBRAT nyomán]. a—geoelektromos időszelvény; b—szeizmikus szelvény

2. 4. *Frequency domain induced polarization* [KULIKOV, SHEMJAKIN 1978]

Frequency soundings were applied only on a small scale in the Soviet Union. There is now a tendency to increase the number of FS-teams due to the integration of frequency soundings with induced polarization (IP) profiling. This combination has proved to be very successful because frequency sound-

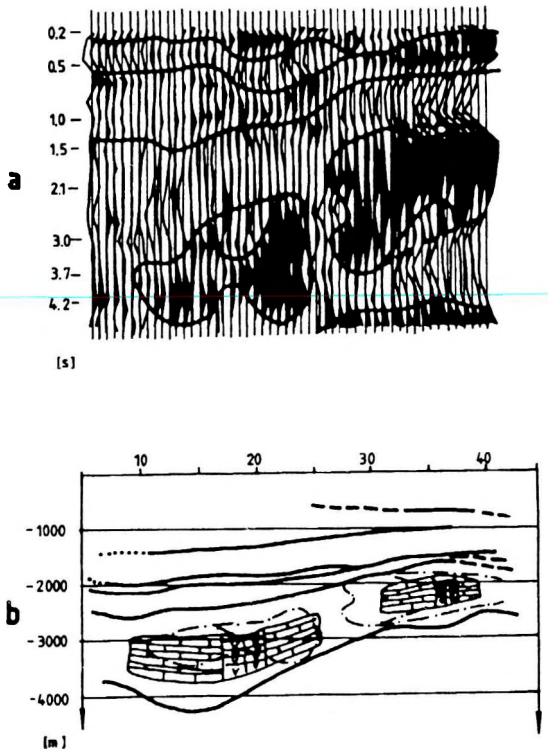

Fig. 20. Comparison of geoelectric and seismic sections [according to NEBRAT]. a—geoelectric time section; b—seismic section

20. ábra. Geoelektromos és szeizmikus szelvény összehasonlítása [NEBRAT nyomán]. a—geoelektromos időszelvény; b—szeizmikus szelvény

ings help to distinguish induction and polarization effects. *Fig. 21* shows the results of IP-profiling performed in the *North Caspian depression*. In order to reduce the induction effects the perpendicular layout was used and a sufficiently low frequency was chosen. It can be seen that oil fields manifest themselves as phase and polarizability maxima.

3. Global geomagnetic and deep magnetotelluric soundings

3. 1. Global geomagnetic sounding [ROTANOVA, PUSHKOV 1982, ROKITYANSKI 1982, FAINBERG 1983, SEMENOV 1989]

In geoelectric investigation of the middle and lower mantle the global geomagnetic sounding is the leading method. Fundamental results have been obtained by FAINBERG, ROTANOVA, SEMENOV using this method. *Fig. 22* shows the global apparent resistivity curve plotted by ROTANOVA. It represents the conductivity distribution in the mantle between 400 and 1500 km. DMITRIEV et al. [1986] performed the inversion of this curve using a set of models

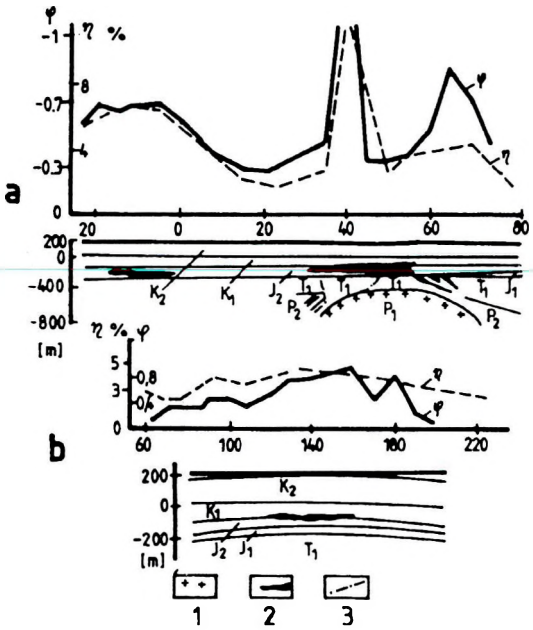

Fig. 21. Results of IP-profiling in the North Caspian depression [according to KULIKOV]. a—Kenkiak oil field; b—Kumsay oil field; IP profiles: φ—phase (degree); η—apparent polarizability; 1—salt; 2—oil field; 3—tectonic line

21. ábra. Az Észak-Kaspi-süllyedékben végzett GP szelvényezés eredménye [KULIKOV nyomán]. a—Kenkiak olajmezõ; b—Kumsay olajmezõ; GP—szelvények : φ—fázis (fok); η—látszólagos gerjeszthetõség; 1—sóréteg; 2—olajmezõ; 3—tektonikai vonal

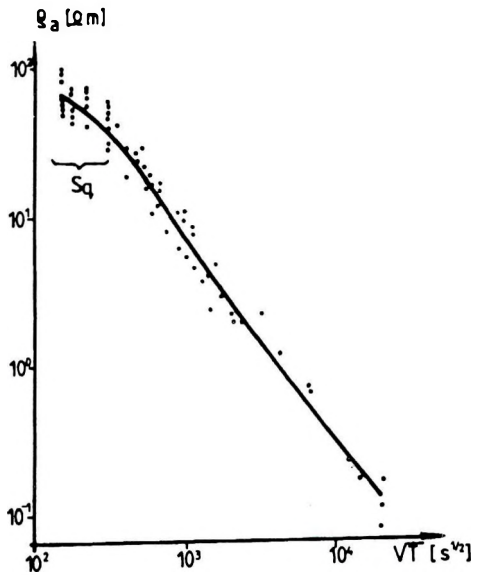

Fig. 22. Global apparent resistivity curve [according to ROTANOVA]. S_q—diurnal interval

22. ábra. Globális látszólagos ellenállás görbe [ROTANOVA nyomán]. S_q—napi változások intervalluma

which are consistent with modern geothermal concepts and physical laws determining the electric conductivity in this depth range. The solution obtained is shown in *Fig. 23.* As can be seen, the middle mantle has a clearly identifiable interval of steeply rising conductivity (between 400 and 700 km). This interval

encompasses the zone of presumable transitions 'olivin-spinel' and 'spinel-stishovite'. The conductivity of the lower mantle varies much more slowly and this suggests phase stability in this zone. The conductivity follows the Jeffreys-Gutenberg distribution of seismic velocity qualitatively.

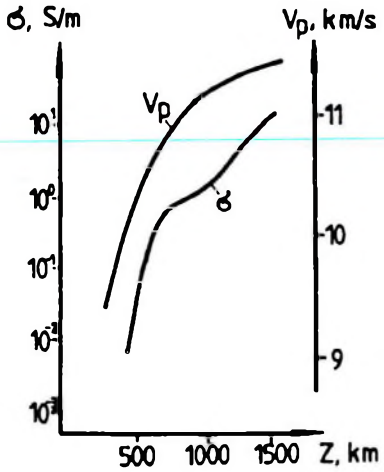

Fig. 23. Distribution of electric conductivity [according to DMITRIEV, ROTANOVA] and *P*-wave velocity V_p [according to JEFFREYS, GUTENBERG]

23. ábra. Az elektromos vezetőképesség [DMITRIEV, ROTANOVA nyomán] és a V_p *P*-hullámsebesség [JEFFREYS, GUTENBERG nyomán] eloszlása

3. 2. Deep magnetotelluric sounding and magnetovariation profiling [KOVTUN 1989, DYAKONOVA et al. 1986, MOROZ 1991, VANYAN, SHILOVSKY 1983, ZHAMALETDINOV 1984]

In geoelectric investigation of the crust and upper mantle, deep magnetotelluric sounding and magnetovariational profiling play the dominant role. For many years geophysicists believed that the Earth's crust had a high resistivity, as it should be for the dry crystalline rocks of the granite and basalt series. It seems that POSPEEV was the first who revealed highly conductive formations within the crystalline crust. Deep geoelectric investigations provided more and more data, and it was concluded that some parts of the Earth's crust are more or less conductive. The high conductivity of the crystalline rocks can be explained by the presence of conductive fluid or graphite. This new model of the lithosphere is gaining ground and opens new possibilities for metallogenic and hydrocarbon prognosis.

Deep geoelectric investigations were carried out in many regions of the former Soviet Union in the last two decades. A large amount of information on the conductivity of the Earth's crust has been collected. Therefore it has become possible to construct a map of crustal conductivity covering huge areas of *Eastern Europe* and *Northern Asia*. *Fig. 24* is a preliminary sketch

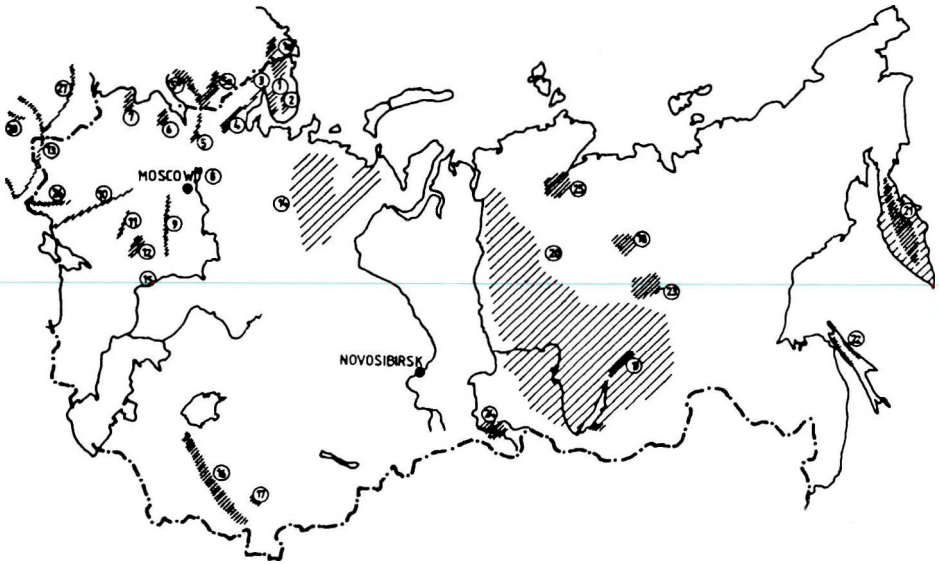

Fig. 24. Scheme of crustal conductivity anomalies [according to ZHAMALETDINOV]. Anomalies: 1—Pechenga; 2—Keivskaya; 3—Tiksheozersko-Belomorskaya; 4—Onega; 5—Ladoga; 5a—Ladoga-Botnicheskaya; 5b—Ladoga-Wennern; 6—Chudskaya; 7—Baltic; 8—Vologda; 9—Moscow-Tambov; 10—Kirovograd; 11—Kursk; 12—Voroncovo; 13—Carpathian; 14—Timan-Pechora; 15—Ilovlya; 16—Tien-Shan; 17—Fergana; 18—Anabar; 19—Bodaibo; 20—Voi-Siberian; 21—Kamchatka; 22—North Sakhalin; 23—Vilyuisk; 24—Minusa; 25—Khatanga; 26—Izmail-Poltava; 27—North German; 28—Pannonian

24. ábra. A kéregbeli vezetőképesség anomáliák vázlatos térképe [ZHAMALETDINOV nyomán]. Anomáliák: 1—Pechenga; 2—Keivskaya; 3—Tiksheozersko-Belomorskaya; 4—Onega; 5—Ladoga; 5a—Ladoga-Botnicheskaya; 5b—Ladoga-Wennern; 6—Chudskaya; 7—Balti; 8—Vologda; 9—Moszkva-Tambov; 10—Kirovograd; 11—Kursk; 12—Voroncovo; 13—Kárpáti; 14—Timan-Pechora; 15-Ilovlya; 16—Tien-Shan; 17—Fergana; 18—Anabar; 19—Bodaibo; 20—Voi-Szibéria; 21—Kamcsatka; 22—Észak-Szachalin; 23—Vilyuisk; 24—Minusa; 25—Khatanga; 26—Izmail-Poltava; 27—Észak-Német; 28—Pannon

of such a map constructed by ZHAMALETDINOV. It shows numerous linear zones and larger areas of high conductivity within the upper and lower part of the Earth's crust. The well-known arc-shaped *Carpathian anomaly* borders the Pannonian Basin. Its nature has long been a subject of discussion (fluid? partial melting? subduction?). Remarkable is the linear *Kirovograd anomaly* which can be traced for 600 km, from the Crimea to the Moscow syneclise. It is interpreted as a belt of deserpentinization caused by recent tectonic activity. One of the most intensive anomalies is the *Tien-Shan anomaly* caused by graphite-containing formations. High crustal conductivity can be observed within the *Baikal rift zone*, the *Tungus syneclise* and the *Vilyuisk syneclise*. The anomaly is assigned to crustal fluids forming a deep hydrosphere. These items of information are still awaiting geological analysis and generalization.

To get a better insight into deep geoelectrics, let us consider the *Kamchatka* region of the crustal conductivity map. *Fig. 25* shows the development of a highly conductive layer. This layer is uplifted in the central part of the peninsula and sinks at its flanks, with conductance decreasing from 6000-

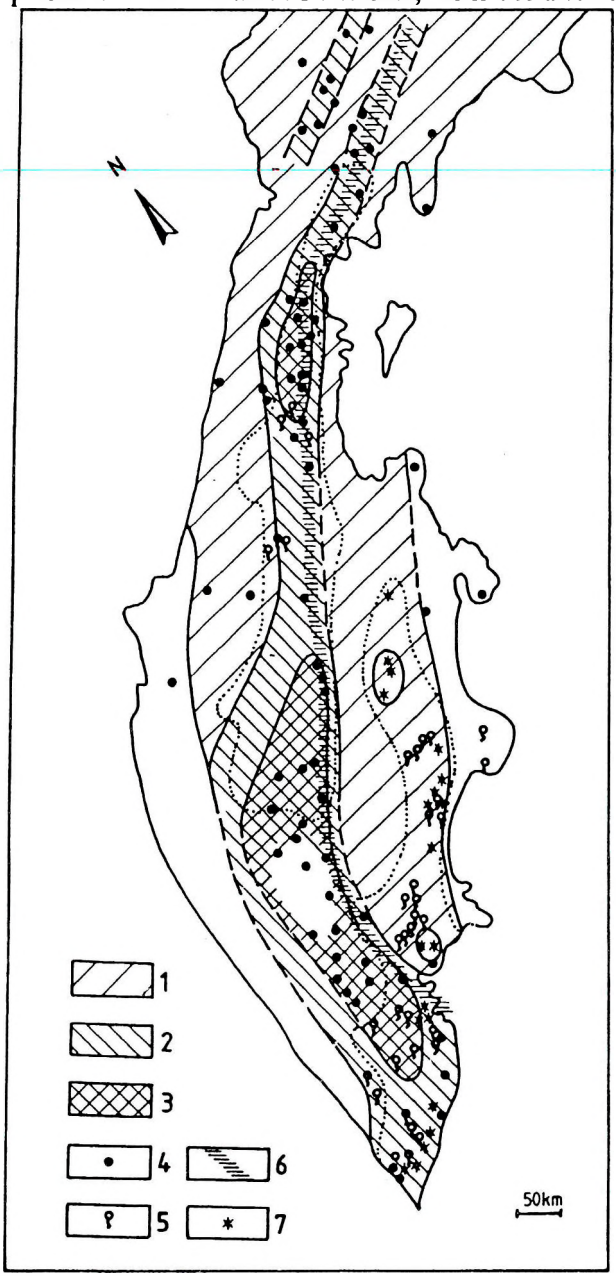

Fig. 25. Map of crustal conductivity in Kamchatka [according to MOROZ]

zone	crustal conducting layer	
	depth (km)	conductance (S)
1	20-30	1000-2000
2	10-15	3000-4000
3	7-10	6000-8000

4—ore occurrence; 5—hydrothermal alteration; 6—major deep fault in Kamchatka; 7—active volcano

25. ábra. A kéreg vezetőképességének térképe Kamcsatkán [MOROZ nyomán).

zóna	a kéregbeli jól vezető réteg	
	mélysége (km)	összegzett hosszirányú vezetőképessége (S)
1	20-30	1000-2000
2	10-15	3000-4000
3	7-10	6000-8000

4—ércelőfordulás; 5—hidrotermális elváltozás; 6—nagyobb mély vető Kamcsatkán; 7—működő tűzhányó

8000 S to 1000-2000 S. The zone of highest conductance coincides with the area of heat flow maximum. It is emphasized that almost all ore occurrences and hydrothermal phenomena are confined to this zone. The deep geoelectric cross-section of the Kamchatka peninsula is shown in *Fig. 26*. Two areas of lower resistivity are outlined within the Earth's crust. They are located in the zones of recent and ancient vulcanism. One of them coincides with a seismic velocity minimum. It seems that both areas can be interpreted as magma chambers. An elevation of the highly conductive asthenosphere is detected in the zone of recent vulcanism. The geoelectric pattern correlates well with the geothermal results. It is obvious that geoelectrics provides unique information about the deep structure of this region.

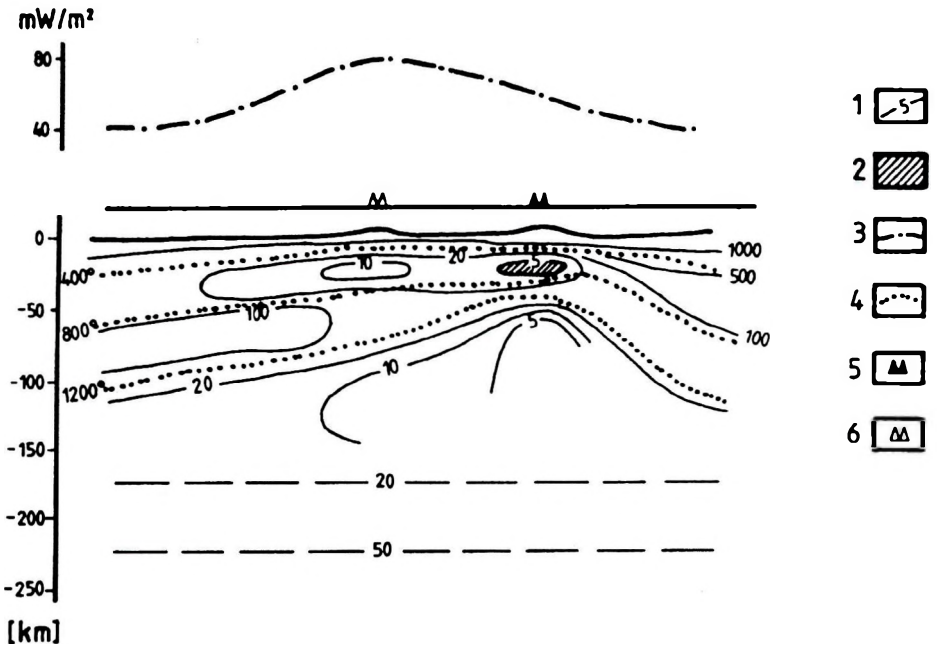

Fig. 26. Deep geoelectric section of the Kamchatka peninsula [according to MOROZ]. 1—contour of resistivity (ohmm); 2—zone of decreased seismic velocity; 3—regional heat flow profile; 4—contour of temperature (°C); 5—zone contemporary vulcanism; 6—zone of volcanic origin

26. ábra. A Kamcsatka-félsziget mély geoelektromos szelvénye [MOROZ nyomán]. 1—a fajlagos ellenállás izovonala (ohmm); 2—csökkent szeizmikus sebesség zónája; 3—regionális hőáram szelvény; 4—hőmérséklet izovonala (°C); 5—jelenlegi vulkanizmus zónája; 6—vulkáni eredetű zóna

4. Conclusions

Experience gained in the former Soviet Union and latterly in Russia suggests that new geoelectric prospecting techniques might provide spectacular results which contribute to the characterization of oil and gas reservoirs. Geologists acknowledge the potential of modern geoelectric prospecting methods that are capable of improving the discovery ratio. Nowadays we have about 80 teams in the petroleum industry applying transient, frequency, IP and magnetotelluric soundings. The use of geoelectric data in selecting drilling sites has become the practice in a number of geophysical enterprises. Great importance is attributed to deep geoelectric investigations aimed at metallogenic and hydrocarbon prognosis, and at dealing with general problems of regional structural geology.

REFERENCES

BACKUS G., GILBERT F. 1986: The Resolving Power of Gross Earth Data. Geophys. J. R. Astr. Soc., **16**, pp. 169-205

BAHR K. 1988: Interpretation of magnetotelluric impedance tensor: regional induction and local telluric distortion. J. Geophys., **62**, pp. 119-127

BARASHKOV A. S., DMITRIEV V. I., BARASHKOV I. S. 1988: A method of solution for inverse problem of sounding of quasi-layered media. IX Workshop on EM induction in the Earth and Moon

BERDICHEVSKY M. N., NGUEN THAN VAN 1991: Magnetovariational vector. Izv. Akad. Nauk SSSR, Fizika Zemli, No **3**, pp. 52-62

BERDICHEVSKY M. N., DMITRIEV V. I. 1992: Magnetotelluric sounding of horizontally homogeneous media. (in Russian) Moscow, Nedra

CAGNIARD L. 1953: Basic theory of the magnetotelluric method of geophysical prospecting. Geophysics, **18**, pp. 605-635

DYAKONOVA A. G., INGEROV A. I., ROKITYANSKY I. I. 1986: Electromagnetic soundings on the East European platform and Urals. (in Russian) Kiev, Naukova Dumka

DMITRIEV V. I., ROTANOVA N. M., ZAKHAROVA O. K., BALIKINA O. N. 1986: Model of deep electrical conductivity from generalized data of global sounding. Geomagnetism i Aeronomia, Vol. XXVI, No 2, pp. 299-306

DMITRIEV V. I. 1987: Inverse Problems in Electrodynamical Prospecting, In monograph: 'Ill-posed Problems in the Natural Sciences', Mir, Moscow, pp. 77-101

EGGERS D. E. 1982: An eigenstate formulation of the magnetotelluric impedance tensor. Geophysics, **47**, pp. 1204-1214

FAINBERG E. B. 1983: Global and regional magnetovariation sounding of the Earth. (in Russian) D.Sc. dissertation, Institute of Terrestrial Magnetism, Moscow

GAMBLE T. D. 1978: Remote reference magnetotellurics. Ph. D. Thesis, Lawrence Berkeley Laboratory, University of California

GONCHARSKY A. V. 1987: Ill-posed problems and their solution methods. In monograph: 'Ill-posed Problems in the Natural Sciences', Mir, Moscow, pp. 21-52

KOVTUN A. A. 1989: Structure of the Earth's crust and upper mantle in the northwestern part of the East European platform according to magnetotelluric data. (in Russian) Leningrad University

KRAJEV A. AP. 1941: Harmonic electromagnetic method for investigation a layered volume. Dokl. Akad. Nauk SSSR, Vol. **31**, No. 7

KULIKOV A.V., SHEMJAKIN E. A. 1978: Electrical prospecting with the phase method of induced polarization, (in Russian) Moscow, Nedra

LAVRENTJEV M. M., ROMANOV V. G., SHISHATSKY S. P. 1980: Ill-posed problems of mathematical physics and analysis. Nauka, Moscow, 286 p.

MOROZ J. F. 1991: Electrical conductivity of the Earth's crust and upper mantle below Kamchatka. (in Russian) Moscow, Nauka

NEBRAT A. G. 1990: Inductive excitation of induced polarization. Transactions of Moscow University. Series 4, Geology, No. 5.

NOVIKOV D. B., BERDICHEVSKY M. N. et al. 1992: The system MTM(at). Moscow State University, Department of Applied Mathematics and Cybernetics. Spline Ltd.

OBUKHOV G. G., CHERNJAVSKY G. A., JAKOVLEV J. A. 1983: Magnetotelluric prospecting in regions of oil potential in the USSR, (in Russian) Moscow, Nedra

OLDENBURG D. 1988: Inversion of Electromagnetic Data: An overview of new techniques. IX Workshop on EM induction in the Earth and Moon

ROKITYANSKI I. I. 1982: Geoelectromagnetic investigation of the Earth's crust and mantle. Berlin, Heidelberg, New York, Springer Verlag

ROTANOVA N. M., PUSHKOV A. N. 1982: Deep conductivity structure of the Earth. (in Russian) Moscow, Nauka

SAFONOV A. (ed.) 1988: Instructions for magnetotelluric prospecting and deep geoelectrics. (in Russian) Moscow, Vniigeofizika

SAVINSKY K. (ed.) 1983: Geological structure of Eastern Siberian provinces with oil potential based on geophysical data. (in Russian) Moscow, Nedra

SCHLUMBERGER C. 1920: Etude de la prospection électrique du sous-sol. Gauthier-Villars, Paris

SCHLUMBERGER M. 1939: The application of telluric currents to surface prospecting. Transactions of Am. Geoph. Union. 20th Annual Meeting. Part 3, pp. 271-277

SEMENOV V. Ju. 1989: Evaluation of electrical conductivity of mantle beneath continents of northern hemisphere. Izv. Akad. SSSR, Fizika Zemli, No 3, pp. 60-67

SHEINMANN S. M. 1947: On transient electromagnetic fields in the earth. Prikl. Geofiz. **3**, pp. 3-55

SIDOROV V. A. 1985: Electrical prospecting using impulses. (in Russian) Moscow, Nedra

TIKHONOV A. N. 1946: On the transient electric current in a homogeneous conducting half-space. Izv. Akad. Nauk SSSR, Ser. Geograf., Geofiz., **10** (3)

TIKHONOV A. N. 1950a: Determination of the electrical characteristics of the deep strata of the Earth's crust. Dokl. Akad. Nauk SSSR, **73**, 2, pp. 295-297

TIKHONOV A. N. 1950b: Determination of a varying electric field in a layered medium. Izv. Akad. Nauk SSSR, Ser. Geograf., Geofiz., **14** (2)

TIKHONOV A. N., ARSENIN V. Ja. 1976: Methodes de resolution de problemes mal poses. Mir, Moscow, 280 p.

TIKSHAEV V. (ed.) 1984: Instructions for transient sounding using multiple overlaps. (in Russian) Saratov Nizhne-Voezhsky. Institute of Geology and Geophysics

VANYAN L. L., SHILOVSKY P. P. 1983: Deep electrical conductivity structure of the oceans and continents. (in Russian) Moscow, Nauka

VOZOFF K. 1972: The magnetotelluric method in the exploration of sedimentary basins. Geophysics, **37**, pp. 98-141

VOZOFF K. (ed.) 1982: Magnetotellurics in oil exploration in the USSR. Vnnigeofizika, Moscow.

ZHAMALETDINOV A. (ed.) 1984: Crustal anomalies in electric conductivity. (in Russian) Leningrad, Nauka

ZINGER B. Sh., FAINBERG E. B. 1985: Electromagnetic induction in inhomogeneous thin layers. Moscow, Institute of Terrestrial Magnetism, 234 p.

A szerkesztő megjegyzése

A Szerkesztőség tisztában van azzal, hogy ezen cikk tartalmában eltér a Geofizikai Közlemények általában publikáltakétól. Úgy véltük azonban, hogy BERDICHEVSKY professzor összefoglalója egy olyan területre nyújt — talán elsőként — betekintést, ahonnan eddig kevés információt kaptunk. Ezért fogadtuk el publikálásra a cikket, annak ellenére, hogy az elméleti fejtegetések inkább kvalitativ leírások, az esettanulmányok pedig nem térnek ki a részletekre, a földrajzi helyek azonosítása sem egyszerű feladat.

A GEOELEKTROMOS MÓDSZEREK SZEREPE A SZÉNHIDROGÉNEK ÉS MÉLYSZERKEZETEK KUTATÁSÁBAN OROSZORSZÁGBAN — ÁTTEKINTÉS

Mark N. BERDICHEVSKY

A geoelektromos módszerek története Oroszországban az ellenállás módszerrel kezdődött a II. világháború előtti Szovjetunióban. A kezdeti sikerek után azonban a frekvencia tartománybeli és tranziens szondázás, a magnetotellurikus (MT) és tellurikus módszer vált uralkodóvá. A geoelektromos módszereket nem szerkezethez kötött szénhidrogén telepek kutatására is alkalmazzák.

Az MT módszer elméleti kérdéseit, az adatfeldolgozást, a vizszintes inhomogenitások hatásait, valamint a 2-D és 3-D inverz probléma megoldásának kérdéseit is tárgyalja. MT kutatási példákat mutat be a Moszkvai-szineklízis területéről, Nyugat-Szibériából, Kelet-Szibériából (Szibériai Tábla) és Szachalinból. A nem szerkezethez kötött telepek kutatására hoz példákat Nyugat-Szibériából, a Kaspi-medencéből és Türkmenisztánból.

A tranziens szondázásokban használt *S*-transzformációs, többszörös átfedéses és normált második különbséges módszert a Kaspi-süllyedékből, Kelet-Szibériából és a Fekete-tengerről vett példákkal mutatja be.

A frekvencia tartománybeli gerjesztett polarizációs szelvényezést sikerrel alkalmazták a szénhidrogének kimutatására az Észak-Kaspi-süllyedékben.

Végül a mély földmágneses és magnetotellurikus szondázás fizikai hátterét és néhány eredményét (Kelet-Európa és Oroszország, részletesen Kamcsatka) tárgyalja.

GEOPHYSICAL TRANSACTIONS 1994
Vol. 39. No. 1. pp. 35-44

LABORATORY METHOD FOR DETERMINING THE COMPLEX DIELECTRIC PERMITTIVITY OF LOOSE ROCKS (STANDING WAVE METHOD)

Pjotr FIJAS*, Bernhard FORKMANN*, Ivo RAPPSILBER**

To determine the dielectric permittivity of loose rocks a laboratory method employing the standing wave method was tested. This procedure is based on the impedance transformation equation for a partial medium-filled coaxial line [von HIPPEL 1954]. By measuring the complex dielectric permittivity of different loose rock samples, it was possible to establish a systematic trend in relation to frequency, water content and the structure of the sediments. The measurements were realized in the frequency range of ground-penetrating radar from 60 to 1000 MHz. If the dielectric permittivity is converted into characteristic propagation parameters, it is possible to describe the propagation relation of high-frequency electromagnetic waves in certain sediments.

Keywords: complex dielectric permittivity, dispersion, ground-penetrating radar, standing wave method

1. Theoretical foundations

The boundary surfaces between two different media (conductor/nonconductor) can be used to transmit electromagnetic waves. The coaxial line is one of the significant types of such wave conductors. From the geometrical condition for transmitting waves, the distance between the conductors being an integer multiple of the half vacuum wavelength projected to the normal of the conductor surface, follows for the loss-free wave propagation in an air-filled wave guide [BADEN FULLER 1974]:

* TU Bergakademie Freiberg, Institut für Geophysik, D-09599, Freiberg
** Geologisches Landesamt Sachsen-Anhalt, D-06118, Halle
Manuscript received: 14 Februray, 1994

$$\lambda_H = \frac{\lambda_0}{\sqrt{1 - \left(\frac{\lambda_0}{\lambda_c}\right)^2}} \tag{1}$$

λ_H—waveguide wavelength,
λ_0—vacuum wavelength,
λ_c—limiting wavelength (TEM-wave).

If a dielectric $\varepsilon_r \neq 1$ is put into the waveguide, Eq. (1) is valid in a modified form:

$$\lambda_{H\varepsilon} = \frac{\lambda_\varepsilon}{\sqrt{1 - \left(\frac{\lambda_\varepsilon}{\lambda_c}\right)^2}} \tag{2}$$

λ_ε—wavelength in the medium,
$\lambda_{H\varepsilon}$—waveguide wavelength in the medium.

With

$$\lambda_\varepsilon = \frac{\lambda_0}{\sqrt{\varepsilon_r}}$$

the following equation results for the dielectric permittivity [SCHILD 1981]:

$$\varepsilon_r = \left(\frac{\lambda_0}{\lambda_{H\varepsilon}}\right)^2 + \left(\frac{\lambda_0}{\lambda_c}\right)^2 \tag{3}$$

The consideration of the real, hence not loss-free, dielectrics requires the introduction of the complex dielectric permittivity

$$\varepsilon_r = \varepsilon' - j\varepsilon''$$

and the complex wave number

$$\gamma = \alpha + j\beta$$

Hence Eq. (3) is extended to [SCHILD 1981]:

$$\varepsilon' = 1 - \left(\frac{\lambda_0}{\lambda_H}\right)^2 - \left(\frac{\lambda_0}{2\pi}\right)^2 (\alpha^2 - \beta^2) \tag{4}$$

$$\varepsilon'' = \frac{\alpha\,\beta\,\lambda_o^2}{2\pi^2} \tag{5}$$

The approach to determining the wave number parameters α and β is possible using the impedance transformation in a waveguide [MEGLA 1961, UNGER 1980]:

$$\frac{\tanh\,[(\alpha+j\,\beta)\,d]}{(\alpha+j\,\beta)\,d} = \frac{1}{j\,\beta_0\,d}\;\frac{m-j\tan\,(\beta_0\,z_0)}{1-j\,m\tan\,(\beta_o\,z_0)} \tag{6}$$

m—adapting factor,
d—length of sample,
β_0—imaginary part of the wave number in the air-filled part of the coaxial line,
z_0—distance of the first voltage minimum to the surface of the sample.

Eq. (6) is a complex-valued transcendental function. Its evaluation is difficult. SCHILD [1981] recommends that the equation be decomposed into real and imaginary parts and the results be found for ε' and ε'' by an iteration algorithm.

Another problem is connected with the fact that Eq. (6) contains trigonometric functions. Some types of solution result from the periodicity of the function tanh.

2. Methodology of measurements

For the measurements, a coaxial line with a tuning out probe, an attachable container for the sample material, and a selective SMV 8.5 microvoltmeter were available. The wave impedance was 70 Ω. All plug connections and connecting cables were adjusted. At the end of the sample container, short circuiting was realized by a metal plate (*Fig. 1*).

The selective microvoltmeter allows one simultaneously to feed into the coaxial line electromagnetic waves with certain frequencies. These are guided along the measuring line and reflected at the short circuit end of the sample container. Thus a standing wave is formed in the coaxial line. Inside the sample the wave is guided with a shorter wavelength. By the transition from sample to air and the superposition with reflected waves from the surface of the sample, a 'change' is produced in the wave picture.

The resulting pattern of the electric field strength depends on the dielectric properties of the sample and reflects the special propagation reaction in the given sample material.

With the help of the capacitive tuning out probe the field distribution can be determined. The target quantities ε' and ε'' can be calculated (Eqs.4, 5) using

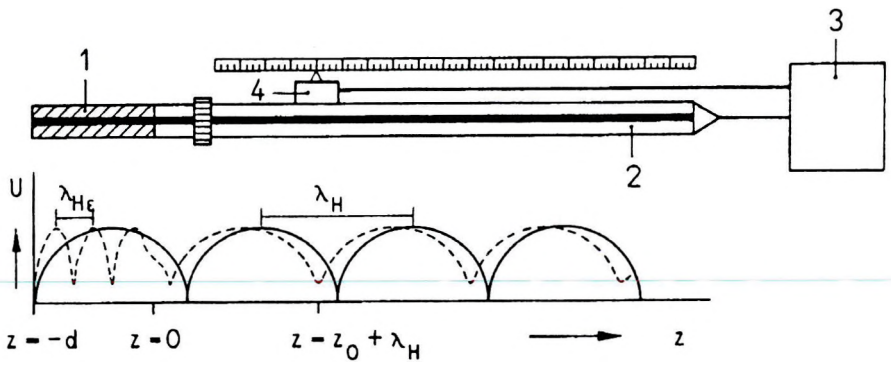

Fig. 1. Measurement place schematically with field strength pattern. 1 — sample container with samples; 2—coaxial line; 3—SMV 8.5; 4—capacitive tuning out probe; continuous line — field strength pattern without sample; dashed line — field strenth pattern with sample

1. ábra. A mérési elrendezés sematikus vázlata a térerősség eloszásával. 1—mintatok mintával; 2—coaxiális vonal; 3—SMV 8.5; 4 — kapacitiv hangoló egység. (A folytonos vonal a minta nélküli, a szaggatott vonal a mintával előálló térerősségeloszlást mutatja)

Eq. (6) by means of a computer program based on the values of the measured maximum and minimum voltage, the position of the voltage minimum with respect to the surface of the sample, the sample length, and the frequency of the fed wave. The computer program also enables one to carry out the iteration procedure in different intervals and thus to calculate different solutions. The correct solution can be found by carrying out measurements with two different sample lengths.

Only one solution corresponding to the measurement with greater sample length is in agreement with one solution corresponding to the measurement with the smaller sample length, thus representing the valid solution. By performing the measurement in a wide frequency range, the correct solution can be seen from the course of the dispersion curve. All the values of this curve have to lie in an interval between $\varepsilon=1$ (air) and $\varepsilon=81$ (water), and they must show a certain course with increasing frequency according to previous investigations [BÖHM 1985, FORKMANN 1983]. The different solutions converge at high frequencies. It was necessary to carry out the measurements at two different wavelengths with some samples only where local dispersion effects were observed (Figs. 4, 5) at higher frequencies and higher dielectric permittivities. Different sediments were prepared as samples [RAPPSILBER 1991] with different water content (all with 0, 1, 2, 4, 8 and some with 12, 16 mass percentage). A definite total mass (sediment and water) was filled into the sample container and compressed to a definite length. Thus the density was found. The sample container was attached to the measurement equipment. The measurements took place at 18 different frequencies between 62 and 1000 MHz.

3. Error analysis

The following input data for the computer program
m — adapting factor (from maximum and minimum voltage),
f — measuring frequency,
z_0 — distance of the first voltage minimum to the surface of the sample,
d — sample length
are erroneous, on the one hand due to accidental errors, on the other hand because of the systematic errors of the measuring devices. The error propagation law cannot be used because Eq. (6) is of transcendental type. Therefore LEHMANN [1989] carried out an error simulation for estimated normal distributions of the four input quantities. Apart from the above, other sources of errors had to be taken into consideration:

— inaccuracies in the determination of sample density,
— erroneously determined water contents,
— uneven sample-air boundary surface,
— possible air gaps between sample and inner or outer conductor [ROST 1979, HUANG, SHEN 1983].

The following error intervals were found:
$\Delta\varepsilon' = \pm 5\%$
$\Delta\varepsilon'' = \pm 8\%$

4. Results

A 3-dimensional representation should be used to illustrate the results of local effects in the dispersion curve of the dielectric permittivity, depending on the water content. This is shown in *Figs. 2, 3* for a sand sample, where the error bars are marked in accordance with the remarks made in Section 3.

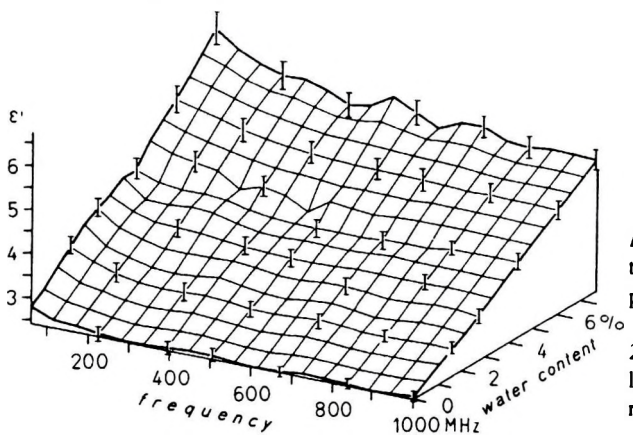

Fig. 2. Real part of the dielectric permittivity of a sand sample (density 1500 kg/m^3)

2. ábra. Egy homok minta dielektromos állandójának reális része (sűrűség 1500 kg/m^3)

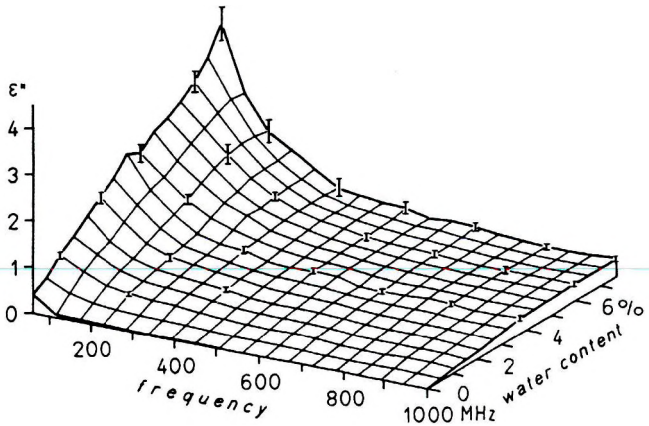

Fig. 3. Imaginary part of the dielectric permittivity of a sand sample (density 1500 kg/m^3)
3. ábra. Egy homok minta dielektromos állandójának képzetes része (sűrűség 1500 kg/m^3)

From similar representations for a number of sediment samples, an attempt was made to find a systematic pattern in the dependence of the dielectric permittivity on several parameters. The dispersion curves of the dielectric permittivity generally show the same behaviour: a stronger decrease in the range from 62 to 200 MHz and a flowing into a plateau area up to 1000 MHz. This behaviour was expected and is in agreement with the measurement results of other authors [SCHILD 1981, BÖHM 1985].

The characteristic increase of the dielectric permittivity with increasing water content is explained at least qualitatively by various mixing formulae. The ε-values obtained can be compared with the results of DELANEY and ARCONE [1984].

Comparing the results of samples with different grain-size distribution it follows that higher values of the dielectric permittivity, both in the real and in the imaginary part, were obtained for smaller effective grain diameters d_w. This may be proved by comparing Figs. 2 and 3 (d_w=0.35 mm) with *Figs. 4* and *5* (d_w=0.01 mm).

The values from the measurement with a glass sphere sample are interesting when compared with similar grain-size distributions of natural samples. Higher values of the dielectric permittivity were obtained for the glass sphere sample with higher water contents. This is due to the lower water bond of grains with relatively small inner surface, in contrast to the stronger water bond with non-regular grain form and, at the same time, a larger inner surface.

Characteristic dispersion effects were obtained for clay and silt samples. Just to give an example, the real and imaginary part of the dielectric permittivity of a clay sample are represented in Figs. 4 and 5.

This observation indicates a complicated relaxation effect of the water being more strongly bonded in fine-grained sediments. The relaxation of free

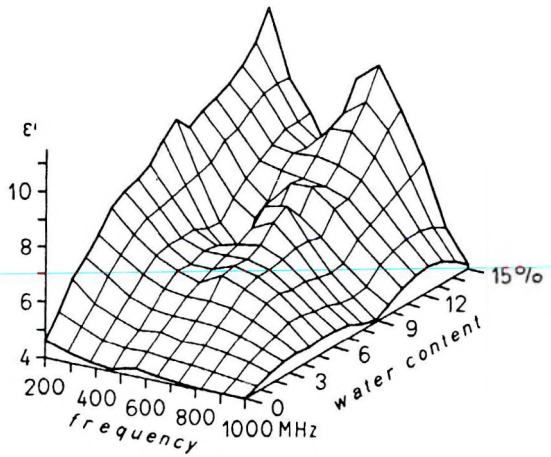

Fig. 4. Real part of the dielectric permittivity of a clay sample (density 1500 kg/m^3)
4. ábra. Egy agyag minta dielektromos állandójának reális része (sűrűség: 1500 kg/m^3)

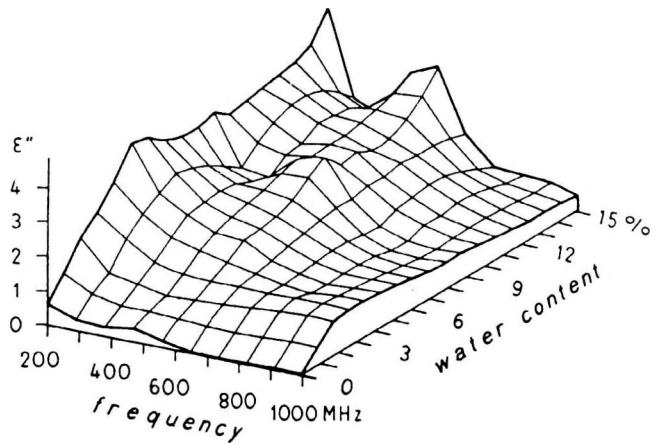

Fig. 5. Imaginary part of the dielectric permittivity of a clay sample (density 1500 kg/m^3)
5. ábra. Egy agyag minta dielektromos állandójának képzetes része (sűrűség: 1500 kg/m^3)

water lies in the GHz-range [HOEKSTRA, DELANEY 1974], but FORKMANN [1983] already assumed that because of specific bonding mechanisms of water in porous loose sediments a shift of the relaxation range to lower frequencies is to be expected.

5. Consequences for the ground-penetrating radar

The penetration depth τ and the phase velocity v are important propagation parameters for high-frequency electromagnetic waves applied to ground-penetrating radar (FORKMANN, PETZOLD 1989]. Both are directly dependent on the complex dielectric permittivity:

$$\tau = \frac{c\sqrt{2}}{\omega\sqrt{\sqrt{\varepsilon'^2 + \varepsilon''^2} - \varepsilon'}} \tag{7}$$

$$v = \frac{c\sqrt{2}}{\sqrt{\sqrt{\varepsilon'^2 + \varepsilon''^2} + \varepsilon'}} \tag{8}$$

Note that the ground-penetrating depth is defined as the distance along which the amplitude of the wave is decreased by e-times, whereas for the assessment of the range depth of a measurement system the performance factor and other equipment parameters have to be taken into account [FORKMANN, PETZOLD 1989]. The penetration depth mainly serves for comparing the propagation properties of different earth substances. Thus, transformation of dielectric permittivity values determined in the laboratory into propagation parameters contributes to the assessment of the applicability or the determination of actual performance parameters of ground-penetrating radar. As an example, the penetration depth is shown for a clay sample according to Figs. 4 and 5 (*Fig. 6*).

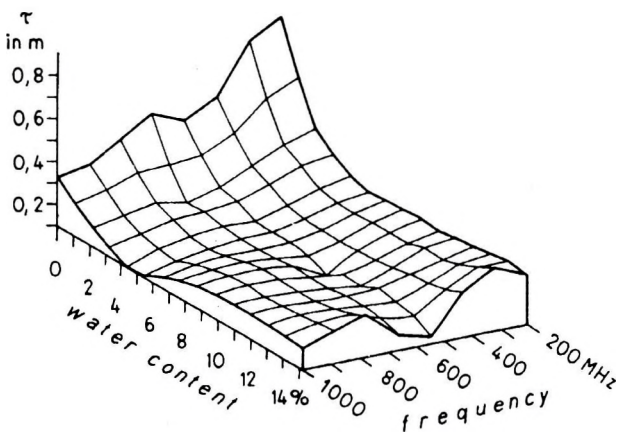

Fig. 6. Penetration depth for the clay sample
6. ábra. Behatolási mélység az agyag mintában

This example demonstrates the selective reduction of the penetration depth for this clay sample as a function of the frequency and water content, thus indicating the special features of wave propagation in cohesive loose sediments.

6. Conclusions

The laboratory determination of the dielectric permittivity of hard rocks in general is realized by placing the rock sample in a so called material condenser, and this does not cause any essential measuring problem. However, a loose rock sample working as a dielectric has to be filled into a coaxial line. Thus there are problems in maintaining in situ conditions. The use of the standing wave method shows that reliable results can be achieved for researching the dispersion curves of the dielectric permittivity as a function of the water content and the structure of various sediments. The utilization of the given laboratory method led to the error intervals being significantly smaller than the dispersion effects. On the other hand some dispersion effects especially of cohesive loose rocks point to the special nature of the water bond in these sediments. Their effects on the propagation of high-frequency electromagnetic waves are of considerable practical interest for ground-penetrating radar.

REFERENCES

BADEN FULLER A. J. 1974: Mikrowellen. Friedr. Viehweg & Sohn, Braunschweig

BÖHM C. 1985: Bestimmung der komplexen Dielektrizitätszahl zwischen 100 und 1000 MHz an Lockergesteinen. Diploma thesis, Bergakademie Freiberg

DELANEY A., ARCONE S. A. 1984: Dielectric measurements of frozen silt using time domain reflectometry. Cold region science and technology **9**, pp. 39-46

FORKMANN B. 1983: Strukturuntersuchungen mit elektromagnetischen Wellen (Gesteinsradar) für Aufgaben in der Betriebserkundung in der Braunkohlenindustrie. Research report, Bergakademie Freiberg

FORKMANN B., PETZOLD H. 1989: Prinzip und Anwendung des Gesteinsradars zur Erkundung des Nahbereiches. Freiberger Forschungshefte C 432. Deutscher Verlag f. Grundstoffindustrie Leipzig

von HIPPEL A. R. 1954: Dielectrics and waves. J.WILEY & Sons, New York

HOEKSTRA P., DELANEY A. 1974: Dielectric properties of soils at UHF and microwave frequencies. J. Geophys. Res. **79**, 11, pp. 1699-1708

HUANG F. S., SHEN L. C. 1983: Analysis of error due to presence of gaps in the measurement of rock samples in a coaxial line. Geophysics, **48**, pp. 206-212

LEHMANN F. 1989: Fehlersimulation zur Berechnung der komplexen Dielektrizitätskonstante auf der Grundlage experimenteller Ergebnisse. Research work, Bergakademie Freiberg

MEGLA G. 1961: Dezimeterwellentechnik. Verlag der Technik, Berlin, 128 p.

RAPPSILBER I. 1991: Labormethodik zur Messung der komplexen Dielektrizitätskonstante nach dem Stehwellenverfahren. Diploma thesis, Bergakademie Freiberg

ROST A. 1979: Messung dielektrischer Stoffeigenschaften. Akademie-Verlag, Berlin, WTB, Band 242, 126 p.
SCHILD D. 1981: Die Messung der komplexen Dielektrizitätskonstante von Gläsern über einen breiten Temperaturbereich im Mikrowellengebiet. Thesis, Technische Hochschule Ilmenau
UNGER H. G. 1980: Elektromagnetische Wellen auf Leitungen. Hüthig-Verlag, Heidelberg

LABORATÓRIUMI MÓDSZER LAZA KŐZETEK KOMPLEX DIELEKTROMOS ÁLLANDÓJÁNAK MEGHATÁROZÁSÁRA (ÁLLÓ HULLÁMOK MÓDSZERE)

Pjotr FIJAS, Bernhard FORKMANN, Ivo RAPPSILBER

A laza kőzetek dielektromos állandójának meghatározására az állóhullám módszert vizsgálták.

Ez az eljárás egy, közeggel részben feltöltött koaxiális kábel impedancia transzformációs egyenletén alapszik [von HIPPEL 1954]. A különböző laza kőzetminták komplex dielektromos állandójának mérésénél szisztematikus kapcsolatot találtak a frekvenciafüggés és az üledékes kőzet víztartalma, szerkezeti jellemzői között.

A méréseket 60 és 1000 MHz közötti frekvenciatartományban hajtották végre. A dielektromos állandót a terjedésre jellemző paraméterekké transzformálva a nagyfrekvenciás elektromágneses hullámok terjedési összefüggéseit írhatjuk le az üledékes kőzetekben.

GEOPHYSICAL TRANSACTIONS 1994
Vol. 39. No. 1. pp. 45-59

TRANSIENT CFS RESPONSE OVER A MULTILAYER EARTH

Hari Pada PATRA*, Baishali ROY*, Sankar Kumar NATH*

The values of the normalized vertical magnetic field component generated in Central Frequency Sounding (CFS) are computed with the help of direct numerical integration using the Gauss quadrature (GQ) method. Fourier summation of the response computed at each harmonic of the primary pulse gives the time domain response. Time domain CFS response curves generated for three-, four-, and five-layer models are analysed in terms of detectability at varying layer conductivity and layer thickness contrasts of a multilayer earth. The effect of loop radii on time domain CFS response resolution is also studied. The computed results from the GQ method agree with those obtained by the digital linear filter technique.

Analysis of data obtained through the GQ method, particularly for *H* and *K* type earth models, shows that the resolution of layers is improved with the increase of loop radius. However, the performance and resolution capability of time domain CFS response for multilayer models seem to be poor for more than three layers but improve with increased loop radius.

Keywords: transient CFS response, multilayer earth, Gauss quadrature method, Fourier summation, digital linear filter technique

1. Introduction

The transient electromagnetic field gradually decays when the primary field is cut off. This decay with the corresponding phase shifts in the frequency components of the primary source are interpreted in terms of the conductivity of the subsurface targets. The high frequency components of the transient pulse are due to shallower events whereas the low frequency components are due to deeper conducting bodies.

Various aspects of central frequency sounding (CFS) in the frequency domain have been studied in detail by PATRA [1970, 1976, 1978], SANYAL

* Department of Geology and Geophysics, Indian Institute of Technology, Kharagpur, 721302, India
Manuscript received: 21 March, 1994

[1975], PATRA and SHASTRI [1982, 1983a, b, 1985, 1988] following KOENIGSBERGER [1939] and YOSHIZUMI et. al [1959]. CFS uses a large circular or square loop as a source with measurements limited to the centre of the loop. A detailed study of the time domain CFS responses over a two-layer earth obtained by using digital linear filters [VERMA, KOEFOED 1973, VERMA 1977, ANDERSON 1979], the Gauss quadrature method, and Simpson's 1/3rd rule has been performed by PATRA et. al [1993, in press]. The Gauss quadrature (GQ) method of computation of the integral gives an accurate result in conformity with the digital linear filter (DLF) technique used by ANDERSON [1979] for computing apparent resistivity for Schlumberger arrays over a horizontally layered earth.

The transmitter-receiver configuration for time domain CFS measurements over a multilayer earth model is shown in *Fig. 1a*. The present work uses a Fourier summation approach to compute the time domain response of an earth model consisting of a number of subsurface layers for the CFS system. Widely spaced sets of geological models for various conductivities, thicknesses, transmitter-receiver separations and resolution of the intermediate layer parameters have also been studied at several geometric and parametric variables pertaining to the CFS system.

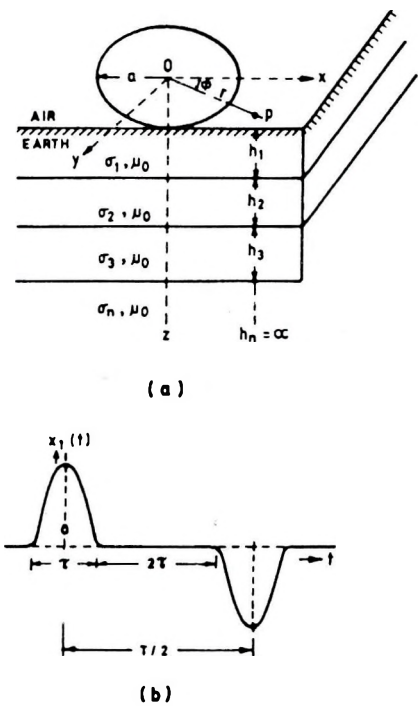

Fig. 1. a—Multi-layer earth model for CFS system; b—Half-sinusoidal primary excitation pulse

1. ábra. a — Többréteges földmodell CFS rendszerhez; b—Fél-szinuszos elsődleges gerjesztő impulzus

2. Methodology

Starting from the basic expression for CFS response [PATRA, MALLICK 1980], the equation for a normalized magnetic field can be given by

$$h_z = \frac{H_z}{H_0} = a^2 \int_0^\infty [1+f(\lambda)]\, \lambda J_1(\lambda a)\, d\lambda \tag{1}$$

The integral involved here is solved with the help of the GQ method of integration. Eq.(1) can be simplified as,

$$|h_z| = 1+a^2 \int_0^\infty f_1(\lambda)\, \lambda J_1(\lambda a)\, d\lambda \tag{2}$$

The kernel function $f(\lambda)$ is computed from the layer parameters and frequency using the recurrence relation

$$f(\lambda) = f_{0,n}(\lambda) \tag{3}$$

The kernel function for a three-layer earth can be given as

$f_{0,3} = f(\lambda) =$

$$= \frac{M_{0,1} + M_{1,2}\, e^{-2h_1\lambda_1} + M_{2,3}\, e^{-2(\lambda_1 h_1+\lambda_2 h_2)} + M_{0,1}\, M_{1,2}\, M_{2,3}\, e^{-2\lambda_2 h_2}}{1 + M_{0,1}\, M_{1,2}\, e^{-2\lambda_1 h_1} + M_{0,1}\, M_{2,3}\, e^{-2(\lambda_1 h_1+\lambda_2 h_2)} + M_{1,2}\, M_{2,3}\, e^{-2\lambda_2 h_2}} \tag{4}$$

where

$M_{0,1} = (\lambda_0 - \lambda_1)/(\lambda_0 + \lambda_1)$,
$M_{1,2} = (\lambda_1 - \lambda_2)/(\lambda_1 + \lambda_2)$,
$M_{2,3} = (\lambda_2 - \lambda_3)/(\lambda_2 + \lambda_3)$,
$\lambda_j^2 = (\lambda^2 + k_j^2)^{1/2}$,
$k_j^2 = i2\pi\mu_0\sigma_j f$ for $j = 1, 2, \ldots, n$,
λ — variable for integration,
f — frequency,
a — loop radius,
h_i — thickness of ith layer,
σ_i — conductivity of ith layer.

The kernel function can be extended to a multilayer earth as

$$f_{j-1,n} = f(\lambda) = \frac{M_{j-1,j} + f_{j,n}(\lambda)\, e^{-2h_j\lambda_j}}{1 + M_{j-1,j}.f_{j,n}(\lambda)\, e^{-2h_j\lambda_j}} \tag{5}$$

and

$$f_{n,n}(\lambda) = 0$$

$$M_{j-1,j} = (\lambda_{j-1} - \lambda_j) / (\lambda_{j-1} + \lambda_j)$$

This is the expression for the normalized magnetic field at the centre of the loop and can be used for any number of subsurface layers.

Primary excitation in a transient system can have any shape: step, ramp, sawtooth, square, trapezoidal, Gaussian, half sinusoidal or pseudo-noise waveforms. In the present study we have considered only one type of excitation, i.e., a series of half sinusoidal pulses of alternating polarity (Fig. 1b). The pulse width is 1 ms and off-period it is 2 ms, the total period is 6 ms, thereby giving a repetition of fundamental frequency of 167 Hz. Such a pulse is represented by:

$$\begin{aligned} f(t) &= H_0 \cos pt && -0.5 < t < 0.5 \text{ ms} \\ &= 0 && 0.5 < t < 2.5 \text{ ms} \\ &= -H_0 \cos pt && 2.5 < t < 3.5 \text{ ms} \\ &= 0 && 3.5 < t < 5.5 \text{ ms} \end{aligned} \tag{6}$$

with

$p = \pi/T$

T— period of complete sine wave

H_0 — primary peak value taken as unity.

The pulse train can be expressed in terms of a Fourier series,

$$f(t) = \sum_{n=1,3,5..}^{\infty} F_n \cos(n\,\omega_0\, t) \tag{7}$$

where

$$\omega_0 = 2\pi/T_0\,; \qquad T_0 = 6 \text{ ms}$$

$$\begin{aligned} F_n &= \frac{8\delta \cos n\pi\delta}{\pi(1 - 4n^2\delta^2)} && \text{for } 2n\delta \neq 1 \\ &= 2\delta && \text{for } 2n\delta = 1 \end{aligned} \tag{8}$$

$\delta = \tau/T$ = duration of the half sinusoid.

The pulse is generated by summing 100 terms. The error at $t = 0.5$ or -0.5 and at other corners of the sine pulse due to Gibb's phenomenon is 1 % [MALLICK, VERMA 1978].

Once the normalized values of the vertical magnetic field component corresponding to each harmonic have been computed, the Fourier series can be summed over all the harmonics to yield the time domain response given as

$$h_z(t) = \mathrm{Re}\left[\sum_{n=1,3,5..}^{N} F_n \left| \frac{H_z}{H_0}(\omega)_n \right| e^{i\, n\omega_0 t + \varphi_n(\omega)}\right] \qquad (9)$$

where

N — number of harmonics,

$\varphi_n(\omega)$ — phase of response at the nth harmonic.

In this case only 100 harmonics are considered since any further increase does not change the response value. The difference between the successive values of the response is less than 10^{-4} after 100 iterations as shown in *Table I.* This has been found to be true for all the models, and some of the results are presented in this table.

Model represented by	Response obtained after iteration (for t = 0.5 ms)			
	50	75	100	125
Fig. 3 (curve 3)	0.4181	0.4703	0.4922	0.4923
Fig. 9 (curve 2)	0.2813	0.3279	0.3452	0.3452
Fig. 10 (curve 1)	0.5321	0.5700	0.5801	0.5802

Table I. Choice of optimum number of iterations

I. táblázat. Az optimális számú iteráció kiválasztása

The summation is over the real part in the time domain. Eq. (9) can further be written as,

$$h_z(t) = \sum_{n=1,3,5..}^{N} F_n \left[\frac{H_z}{H_0}\Big|_n^{\gamma} \cos n\omega_0 t - \frac{H_z}{H_0}\Big|_n^{i} \sin n\omega_0 t \right] \qquad (10)$$

The vertical component of the magnetic field at the centre of the loop has been calculated using the GQ method as discussed below.

In this method the integral is approximated by

$$\int_0^{\infty} W(x)\,[1 + f(\lambda)]\,\lambda\, J_1(\lambda a)\, d\lambda = \frac{L}{2} \sum_{i=1}^{n} g_i f(v_i) \qquad (11)$$

where

$L \to \infty$. L is usually taken as large as possible till the integral converges.

i — varies from 1 to 12 for the 12-point GQ method,

g_i — weights or coefficients corresponding to the points v_i. The values of v_i and g_i have been taken from standard mathematical tables.

$W(x) = 1$.

3. Computational steps

The algorithm used to compute the CFS response by the GQ method consists of the following steps:

Step 1: Input parameters: loop radius, number of layers (NL), layer conductivities (σ_i), layer thicknesses (h_i) and GQ points (v_i), and their corresponding coefficients (g_i).

Step 2: Frequency (c/s)=167 to 33400 in steps of 334.

Assume $\alpha = 0$,

$$\beta = 0.01 \times \text{loop radius}.$$

Step 3: Compute the transformed variables

$$\gamma = (\beta - \alpha)/2 \; ; \quad \eta = (\beta + \alpha)/2$$

For $i = 1,12$ compute $x = \gamma v_i + \eta$

Step 4: Compute the Bessel function $J_1(\lambda a)$ and kernel $f(\lambda)$ using Eq. (5) with the substitution $\lambda a = x$.

Step 5: Compute the integrand $J_1(\lambda a)\,[1 + f(\lambda)]\,\lambda$.

Step 6: Multiply the above product by the coefficients g_i and carry out the summation as given in Eq. (11) for all 12 points. This gives the values of the integral in (α, β).

Step 7: Change $\alpha = \alpha + 0.01 \times$ loop radius

$\beta = \beta + 0.01 \times$ loop radius

and repeat steps 3-7 until the integral value reaches saturation.

Step 8: Steps 3-7 are repeated for all the harmonics and the values are stored in an array.

Step 9: Time domain response is computed using Eq. (10). The Fourier coefficients are computed at each harmonic using Eq. (8).

Step 10: Steps 2-9 are repeated for each time point, i.e., 0.5 - 2.5 ms in steps of 0.5 ms.

Step 11: The time point and the time domain response are taken as output.

4. Results and discussions

The following numerical model studies have been carried out for time domain CFS by using the above algorithm. The results are presented in the form of response curves for varying loop radii, layer conductivities and layer thicknesses.

A special four-layer case is considered to compare the results obtained by the commonly used DLF technique and by the GQ method used in the present study. *Fig. 2* represents the time domain CFS response curves computed by DLF and GQ methods for a loop radius of 500 m placed over the in-set layered

earth model for a half-sinusoidal excitation. The DLF and GQ responses are found to be in good agreement. In the subsequent case studies, only GQ responses are analysed.

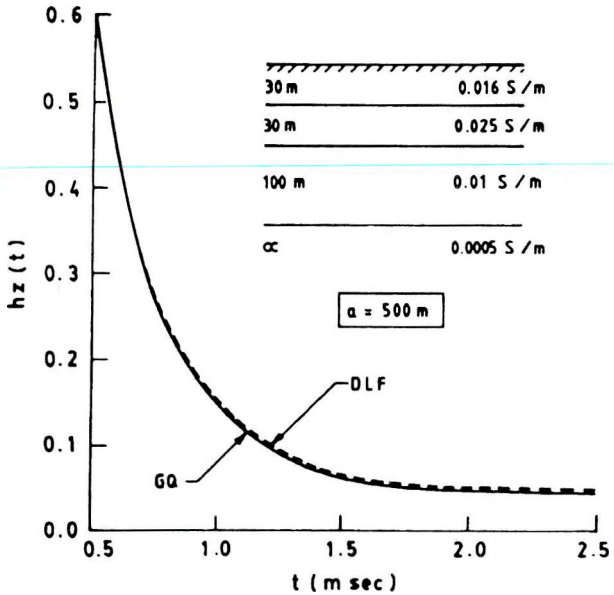

Fig. 2. Comparison between DLF and GQ responses

2. ábra. A digitális lineáris szűrés (DLF) és a Gauss kvadratúra (GQ) válaszfüggvények összehasonlítása

Effect of loop radius on the CFS response for 3-layer models:

Fig. 3 shows the model parameters and the time domain CFS response curves for *H*-type laterite-clay-sand sequence. Curves 1, 2 and 3 show the responses due to loop radii 500, 1000 , and 1500 m respectively. The response curves show that the decay is fast at early time points, e.g., 0.5 to 1 ms, and becomes flat at later times. This is true for all loop radii. But there is an increase in the magnitude of the response as the loop radius is increased. For large loop radii, information comes from deeper layers because of the lower harmonics. Thus, the decay rate is slow even at early time points for larger loop radii. This results in good resolution of response curves at early points and negligible resolution at later points.

Fig. 4. shows an *H*-type earth model with a highly resistive basement with weathered dry and saturated sequence on top. Curves 1, 2 and 3 represent the time domain responses for various loop radii. In this model, the thicknesses of the upper two layers are the same. The decay is much slower than the previous

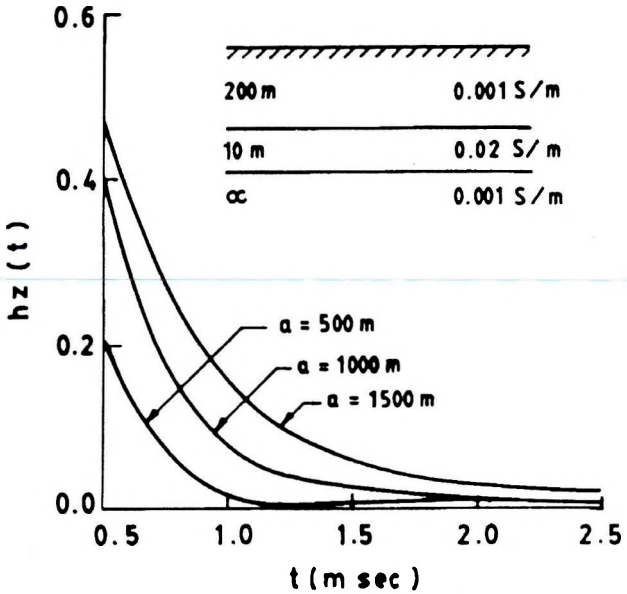

Fig. 3. Time domain CFS response curves for *H*-type earth: effect of loop radius

3. ábra. Időtartománybeli CFS válaszfüggvények *H*-típusú rétegek esetén: a hurok sugarának hatása

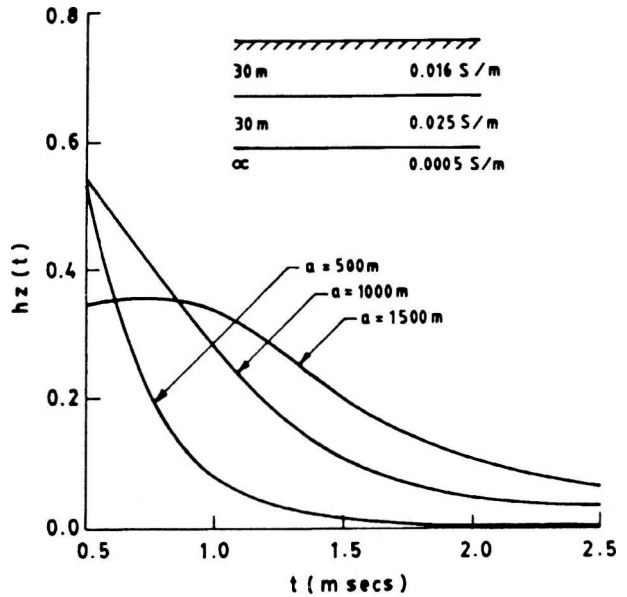

Fig. 4. Time domain CFS response curves for *H*-type earth: effect of loop radius

4. ábra. Időtartománybeli CFS válaszfüggvények *H*-típusú rétegek esetén: a hurok sugarának hatása

case. Here also the decay gradually diminishes as the loop radius is increased at all time points. The response is flat for a loop radius of 1500 m. The resolution of the curves is high for both early and late times.

Effect of layer conductivity on the CFS response for 3-layer models

The model parameters and the CFS response for a three-layer earth model with different conductivity contrasts (in terms of first layer conductivity) are presented in *Fig. 5.* All the models have a highly resistive basement. Curve 1 represents an *A*-type model and curves 2 and 3 represent *H*-type earth models. In all these models the thickness of the top layer is more than that of the second layer. The response curves indicate that for σ_2 less than σ_1, the decay is very fast up to about 1 ms and ceases to exist after that. However, for σ_2 greater than σ_1, the decay is gentle for early time points and becomes very slow at later times. There is good resolution of the curves for σ_2 greater than σ_1.

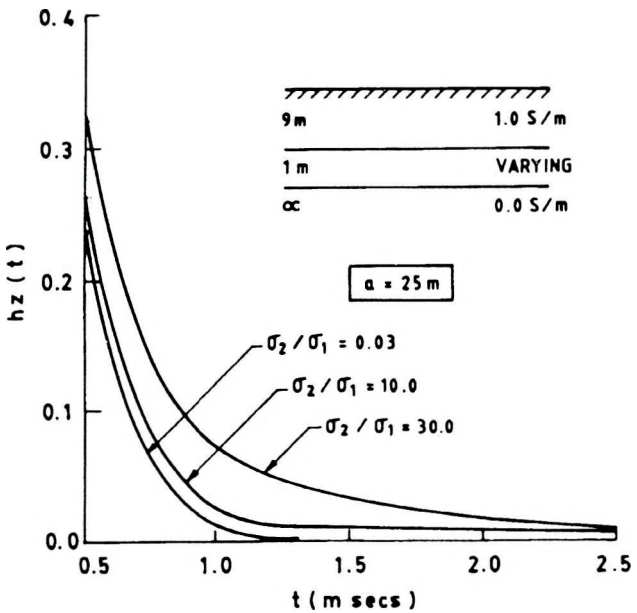

Fig. 5. Time domain CFS response for three-layer earth: effect of conductivity contrast

5. ábra. Időtartománybeli CFS válaszfüggvények háromréteges esetben: a vezetőképesség-kontraszt hatása

Effect of top layer thickness on CFS response for 3-layer models

The configuration and physical parameters of *A*-type model with a highly resistive basement are presented in *Figs. 6* and *7*. The models in Fig. 7 have a more conducting second layer compared to those in Fig. 6. The curve parameter here is a/h_1 with a loop radius of 25 m. From both figures it is observed that the decay rate is very fast and the response is negligible after 1 ms. As the top layer thickness increases, the decay rate becomes gentle. Although there is some resolution of the curves for early time points, resolution is totally lost after 1.5 ms. A comparison of Figs. 6 and 7 reveals that the resolution does not improve even if the σ_2/σ_1 ratio is increased.

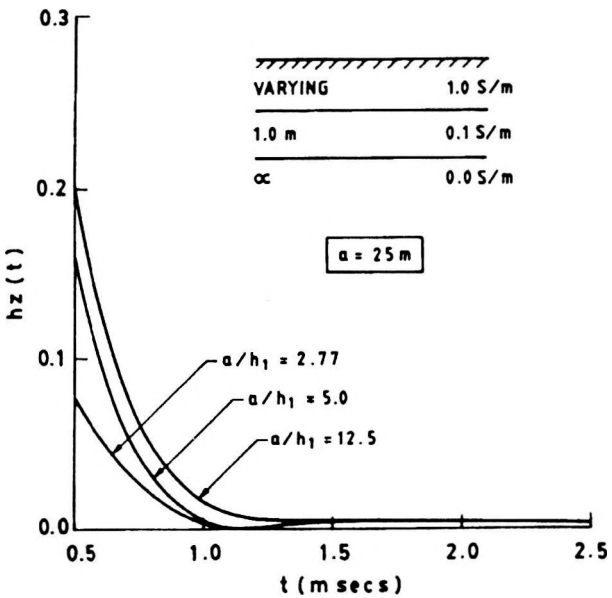

Fig. 6. Time domain CFS response curves for *A*-type earth: effect of top layer thickness
6. ábra. Időtartománybeli CFS válaszfüggvények *A*-típusú rétegek esetén: a fedőréteg vastagságának hatása

Effect of intermediate layer thickness on CFS response of 3-layer models

Fig. 8 is a representation of the transient CFS response obtained for *H*-type models for varying h_2/h_1 ratio and at different loop radii. Significant separation of the response curves is observed for loop radii 500 m and 1000 m and for thickness ratio 2 and 5. The change in layer thickness does not give rise to

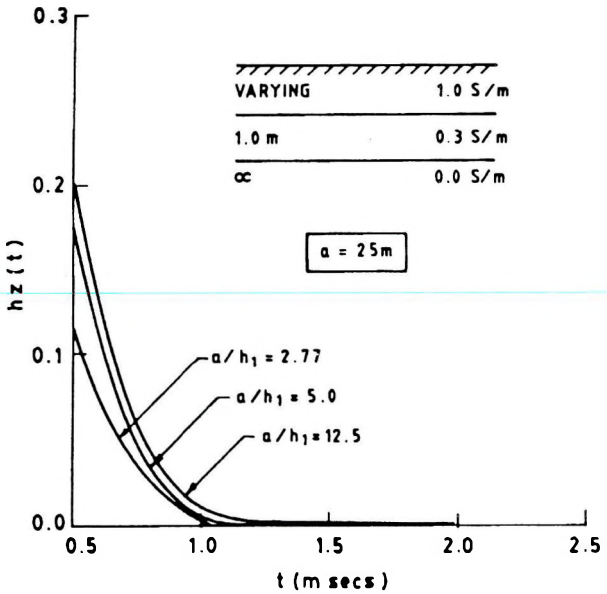

Fig. 7. Time domain CFS response curves for *A*-type earth: effect of top layer thickness
7. ábra. Időtartománybeli CFS válaszfüggvények *A*-típusú rétegek esetén: a legfelső réteg vastagságának hatása

significant variation in the anomaly pattern. Resolution is very poor at all time points with increase in h_2, although the situation improves with the increase in loop radius.

Nature of time domain CFS response curves for multilayer earth

The layer parameters and the response curves for a four-layer (*HA*-type) model and a five-layer (*HAA*-type) model are shown in Figs. 9 and 10. Response curves presented for a four-layer earth in *Fig. 9* show that variation in layer conductivity is well reflected on the response curves with increase in loop radius. The response decays rapidly at early times for small loop radius. Slow decay of response, particularly at later times, is due to the presence of conductive and resistive layers in the four-layer earth model. The response is more flat than that for the three-layer case with a comparatively high resolution.

The quantitative nature of the response due to a five-layer earth model is presented in *Fig. 10.* The nature of response is almost similar to that obtained for a four-layer case. Gradual change in response at late times for large loop radius and rapid fall of response at early times for small loop radius are important criteria for identifying an additional layer inserted within a four-layer

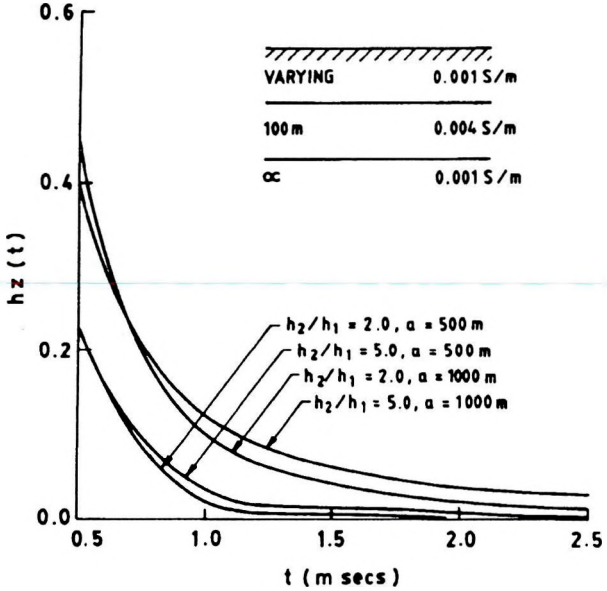

Fig. 8. Time domain CFS response curves for *H*-type earth: effect of thickness and loop radius
8. ábra. Időtartománybeli CFS válaszfüggvények *H*-típusú rétegek esetén: a vastagság és a hurok sugarának hatása

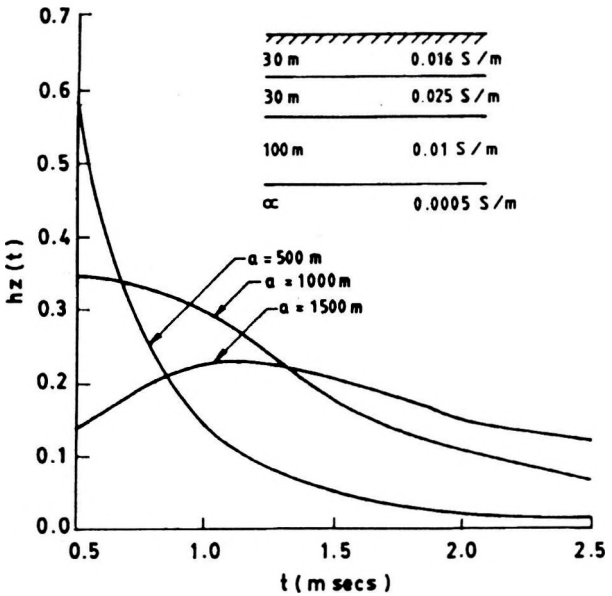

Fig. 9. Time domain CFS response curves for four-layer earth: effect of loop radius
9. ábra. Időtartománybeli CFS válaszfüggvények négyréteges esetben: a hurok sugarának hatása

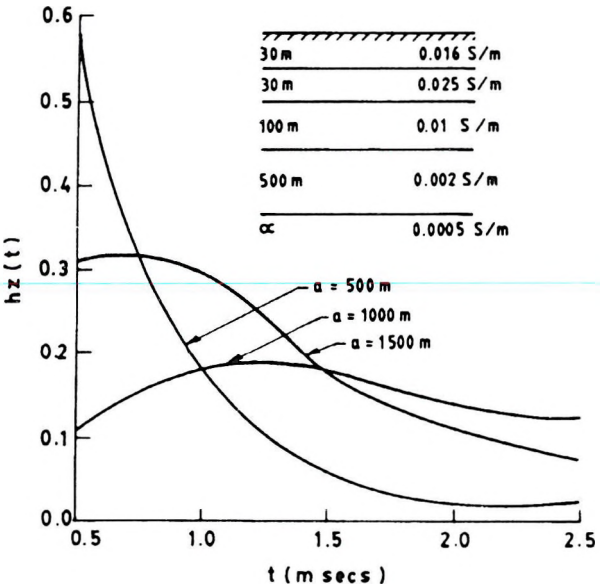

Fig. 10. Time domain CFS response curves for five-layer earth: effect of loop radius
10. ábra. Időtartománybeli CFS válaszfüggvények ötréteges esetben: a hurok sugarának hatása

earth situation. A slow variation in the nature of the response curves is prominent here and the resolution is good.

A comparison of Fig. 4 (for a three-layer case) with those of four- and five-layer cases given in Figs. 9 and 10 respectively shows:

— For a loop radius of 500 m, the shape of the curves for three-, four- and five-layer cases, remains unaltered showing poor detectability.

— For loop radii 1000 m and 1500 m, however, the shape of the curves undergoes considerable change with a better resolution and detectability.

5. Conclusion

A study of the variation in amplitude of a normalized magnetic field over a multilayer earth provides an idea of relative depth of investigation and the resolution capabilities of transient CFS. The variation in amplitude of the normalized magnetic field component at varying layer conductivity contrasts in a three-layer sequence is well reflected particularly at later times and high conductivity contrasts between the first and second layers. The resolution of layer thickness in three-layer models is improved by the increase in second layer thickness and loop radius. The effect of variation of layer conductivity

and layer thickness in a multilayer sequence on the separation between response curves improves with an increase in loop radius. The intermediate conductive layer in an *H*-type earth model is also resolved better with the increase in loop radius. For increase in number of layers beyond three, detectability is, in general, poor. Increase in loop radius beyond 500 m marginally enhances the resolution .

REFERENCES

ANDERSON W. L. 1979: Computer Program — numerical integration of related Hankel transform of orders 0 and 1 by adaptive digital filtering. Geophysics **44**, pp. 1287-1305

KOENIGSBERGER J. G. 1939: Elektrische Vertical-Sounding von der Erdoberfläche aus mit der Zentral-Induktions Methode. Beiträge Zur Angewandten Geophysik **7**, pp. 112-161

MALLICK K., VERMA R. K. 1978: Time varying electromagnetic sounding with horizontal vertical coplanar loops on a multilayer earth. Geoexploration **16**, pp. 291-302

PATRA H. P. 1970: Central frequency sonding in shallow engineering and hydrogeological problems. Geophys. Prosp. **18** (2), pp. 236-254

PATRA H. P. 1976: Electromagnetic depth sounding for groundwater with particular reference to CFS: Principles, interpretation and applications. Geoexploration **14**, pp. 254-258

PATRA H. P. 1978: A three frequency computational method for two layer CFS data. Bolletino di Geofisica Teorica ed Applicata **21** (7), pp. 35-45

PATRA H. P., MALLICK K. 1980: Geosounding Principles II, Time varying geoelectric soundings, Elsevier, Amsterdam

PATRA H. P., SHASTRI N. L. 1982: Relative performances of central and dipole frequency sounding over a layered earth. Pageoph **120**, pp. 527-537

PATRA H. P., SHASTRI N. L. 1983a: Computation of model curves for central frequency sounding by means of digital linear filter. Bolletino di Geofisica Teorica ed Applicata **25** (98), pp. 119-130

PATRA H. P., SHASTRI N. L. 1983b: Theoretical central frequency sounding response curves over a generalised three-layer earth. Pageoph **121** (2), pp.317-325

PATRA H. P., SHASTRI N. L. 1985: Response characteristics of central frequency sounding over a multilayer earth. Bolletino di Geofisica Teorica ed Applicata **27** (105), pp. 41-46

PATRA H. P., SHASTRI N. L. 1988: Multifrequency sounding results of laboratory simulated homogeneous and two layer earth models. Transactions on Geoscience and Remote Sensing **36** (6), p. 749

PATRA H. P., ROY B., SHASTRI N. L., NATH S. K. 1993: Transient CFS response over a two-layer earth (in press)

SANYAL N. 1975: Some studies on electromagnetic depth sounding for shallow groundwater exploration problems. Ph. D Thesis, IIT Kharagpur, India

VERMA R. K. 1977: Detectability by electromagnetic sounding systems, IEEE Trans. Geosci. Electr. **GE-15** (4), pp. 232-251

VERMA R. K., KOEFOED O. 1973: A note on the linear filter method of computing electromagnetic sounding curves, Geophys. Prosp. **21**, pp. 70-76

YOSHIZUMI E., TANIGUCHI K., KIYONO T. 1959: Vertical electrical sounding by central ring induction method. Mem. Fac. Eng. Kyoto Univ. 21/2, pp. 154-169

A TRANZIENS KÖZÉPPONTI FREKVENCIASZONDÁZÁS VÁLASZFÜGGVÉNYE TÖBBRÉTEGES MODELL ESETÉN

Hari Pada PATRA, Baishali ROY, Sankar Kumar NATH

A középponti frekvenciaszondázással (CFS) generált normalizált vertikális mágneses térkomponens értékeit Gauss kvadratúra (GQ) módszerrel, direkt numerikus integrálással számították ki. Az időtartománybeli választ az elsődleges impulzus minden harmónikusára kiszámított Fourier összegzés adja. A három-, négy- és ötréteges modellekre kiszámított időtartománybeli válaszgörbéket változó vezetőképesség- és rétegvastagság különbségek mellett az érzékelhetőség szempontjából elemezték. A hurok sugarának hatását az időtartománybeli regisztrátum felbontási teljesítménye tekintetében is tanulmányozták. A GQ módszerrel számított eredmények megegyeznek a digitális szűrés eredményeivel.

A GQ módszerrel nyert adatok, különösen a *H* és *K* típusú rétegmodellek esetén azt mutatják, hogy a hurok sugarának növelésével a felbontás javul .

Többréteges esetben, — háromnál több réteg esetén — azonban az időtartománybeli CFS átvitel minőség és felbontás tekintetében túl szegényesnek tűnik, amelyek azonban javithatók a hurok sugarának növelésével.

GEOPHYSICAL TRANSACTIONS 1994
Vol. 39. No. 1. pp. 61-75

MAGNETIC PULSE METHOD APPLIED TO BOREHOLE DEVIATION MEASUREMENTS

Vladimír SEDLÁK*

A magnetic method for borehole deviation measurements in certain cases of tunnelling and driving other underground workings is presented. The mutual positions of boreholes arranged in groups for driving underground mining and engineering workings in water-bearing layers by the freezing and grouting method are determined. In determining the distances between boreholes the pulse magnetic method is supplemented by accuracy analysis.

Keywords: magnetic induction, borehole deviation, accuracy analysis, Slovak Magnesite Mines

1. Introduction

Basically there are three operational causes of borehole deviations in long borehole drilling (*Fig.1*), viz. alignment (d_a), collaring (d_c), and trajectory (d_t) (rod path/bit contact with rock). In this sense therefore, borehole deviation can be defined as the departure of a borehole from its designed starting point, its designed path, and its designed destination point.

Since operator/machine dependent causes, viz. alignment and collaring occur outside of boreholes and are hence easier to investigate and understand, this study concentrates on the third problem, i.e. trajectory borehole deviation, which is by far the most critical — especially for long boreholes. The source categories of factors contributing to trajectory deviation include pattern of boreholes, drill forces, equipment components, and rock properties.

* Technical University of Košice, Department of Geodesy and Geophysics, Letná 9, Košice, SK-04200, Slovakia
Manuscript received (revised version): 14 May, 1994

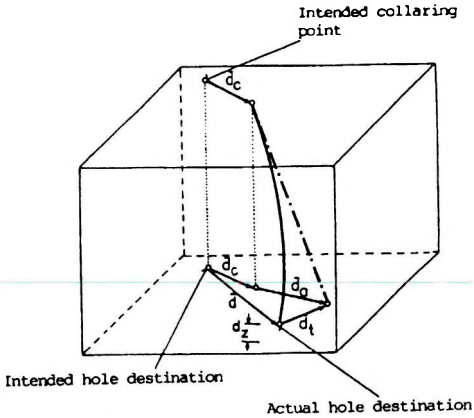

Fig. 1. Diagramatic representation of alignment (d_a), collaring (d_c), and trajectory (d_t) deviations

1. ábra. A d_a eltérés, d_c béléscsövezés, és a d_t elcsavarási-trajektoria diagramszerű vázlata

A great many studies have dealt with the problem of whether one can learn more about the rock dependent part of trajectory deviation and thereby influence the deviation by means of borehole patterns [SINKALA 1987].

Water-bearing cohesionless layers pose a considerable problem in tunnelling and driving underground workings and other engineering projects. The most extensively used methods of strengthening or sealing rock in these layers include rock freezing and the grouting of various suspensions and solutions. The factor which determines the efficiency of strengthening the rock by freezing and grouting is mainly the accuracy of drilling the position of the freezing and grouting boreholes.

In drilling a series of boreholes several tens of meters in length, these may deviate from the required direction. Such deviation and deflection of one of several boreholes e. g. boreholes Nos. 1 and 6 in *Fig. 2* in tunnelling, may cause

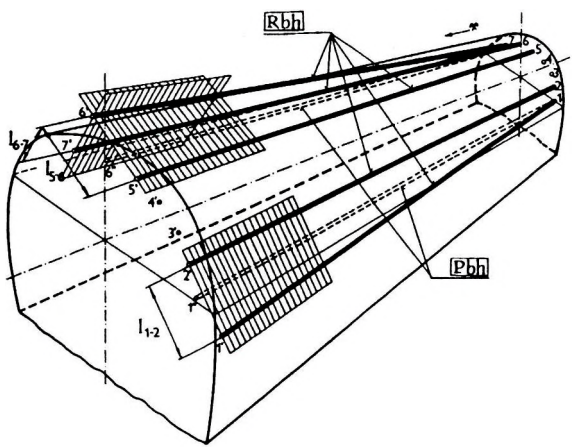

Fig. 2. Block scheme of deviated boreholes in tunnelling. *Pbh*—Projected boreholes; *Rbh*—Realized boreholes

2. ábra. Az elhajlott fúrólyukak vázlata. *Pbh*—tervezett fúrólyukak; *Rbh*—megvalósult fúrólyukak

failure of the entire technological process. Boreholes for blasting are important for underground technologies. The degree of breakage is dependent on the mutual position and deviation of these boreholes.

2. Principle of the magnetic pulse method

One way of mapping the position of boreholes by magnetic methods is based on measuring the component of magnetic induction B of a generated magnetic field. Using the measured values of the field of a rod magnet, it is possible to determine the distance (length l) between the source of this field and the sensor of the magnetometer, i.e. $B=f(l)$ [SEDLÁK 1991, 1992, 1993].

The mutual position of the boreholes is determined in the mapping plane as a network of triangles based on lengths l (distances between boreholes). It is then possible to evaluate the suitability of borehole course and position for applying freezing and grouting technologies or the technology of driving underground mining or engineering workings by blasting.

The advantages of this magnetic probe method include the fact that the cost of devices and materials is low, the accuracy of the method is relatively high, measurements are rapid, and the results can be calculated directly in-situ.

The advantages of the pulse regime are low power input but, at the same time, it is possible to gain an increase in the time change of the measured magnetic field intensity. Electromagnet feeding is illustrated by the diagram of *Fig. 3,* where contact *SP* in the preparatory phase to the measurement is in the given position and condenser C_1 is charged at the initial voltage $U_{C1(0)}$. At the moment of a measurement, the contact *SP* disconnects condenser C_1 from the feeding source and switches it in series with the electromagnet winding,

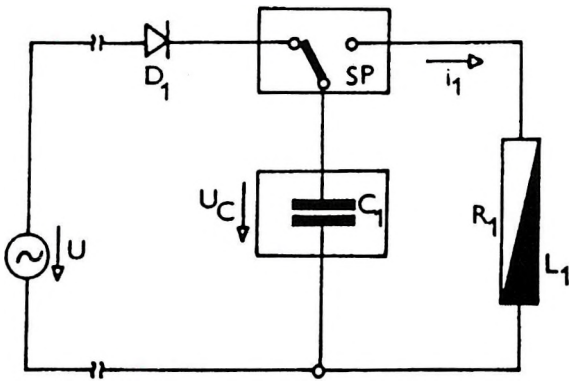

Fig. 3. Diagram of electromagnet electric circuit. *SP*— contact; C_1 —condenser; L_1— inductance; R_1—resistance

3. ábra. Az elektromágnes áramkörének vázlata. *SP*—érintkezés; C_1—kondenzátor; L_1—önindukció; R_1—ellenállás

characterized by the active resistance R_1 and in inductance L_1. The transition phenomena occurs, inducing the defined magnetic field intensity time change [BLAŽEK 1985].

In the electric part of the circuit this phenomena is expressed by the equation

$$R_1 i_1 + l_1 \frac{\mathrm{d}i_1}{\mathrm{d}t} + \frac{1}{C_1}\int_0^t i_1 \mathrm{d}t + U_{C1(0)} = 0 \tag{1}$$

By modifying the differential equation of the second order, one obtains the roots

$$k_{1,2} = -\beta \pm (\beta^2 - \Phi_r^2)^{(1/2)} \tag{2}$$

where

$$\beta = \frac{R_1}{2L_1}; \qquad \Phi_r^2 = \frac{1}{L_1 C_1} \tag{3}$$

and where β represents the damping coefficient and Φ_r the resonance frequency.

It is suggested that the parameters of the electromagnet are such that the condition of low circuit damping will be fulfilled, so $R_1 < 2 (L_1 C_1)^{1/2}$. The transition phenomenon of the electromagnet current is then a periodic harmonic function

$$i_1 = \frac{U_{C1(0)}}{\Phi_r L_1} = e^{-\beta t} \sin \Phi_r t \tag{4}$$

In first approach it is possible to consider the ideal case of undamped oscillations, when the amplitude reaches the value

$$i_{1(max)} = \frac{U_{C1(0)}}{\Phi_r L_1} = I_0 \tag{5}$$

and this current value will be reached at moment

$$t_{1(max)} = \frac{\pi}{2}(L_1 C_1)^{1/2} \tag{6}$$

The electromagnet current maximum time change can then be expressed by

$$\lim_{\mathrm{d}t \to 0} \frac{\mathrm{d}i_1}{\mathrm{d}t} = I_0 \Phi_r \tag{7}$$

To this state corresponds the maximum time change of the magnetic field intensity H and maximum time change of the electromagnet magnetic induction B

$$\left[\frac{dh}{dt}\right]_{max} = \frac{N}{2^{1/2}} I_0 \Phi_r; \qquad \left[\frac{dB}{dt}\right]_{max} = \mu_0 \left[\frac{dH}{dt}\right]_{max} \tag{8}$$

where N gives the number of windings of the electromagnet and μ_0 is core permeability.

In pulse magnetization of materials this is magnetized in internal small (minority) loops, and it is the result of current or voltage impacts in one direction [REINBOTH 1970]. In order to obtain the maximum change of induction dB, the shortest time pulses must be selected.

The magnetic field is generated by an electromagnet with a corresponding number of turns wound round the cylindrical core of a special, magnetically-soft material. The electromagnet is inserted into the casing of the source probe. During measurements the probe is placed in the appropriate measurement area in a single borehole. The measuring element is in the form of an induction coil inserted into the casing of the measuring probe which is placed, during measurements, in the appropriate measurement area in the second borehole (*Fig. 4*). It is necessary to determine the distance between the probe of the source and the measuring probe in the mapping plane, i.e., the length l between both boreholes in this plane. This is based on the knowledge that the vector of magnetic induction B, parallel to the axis of the given electromagnet, is situated at the points of the plane perpendicular to this axis and passing through the centre of the electromagnet (equatorial plane). The value of magnetic induction B depends on the distance l between the probe of the source and the measuring probe.

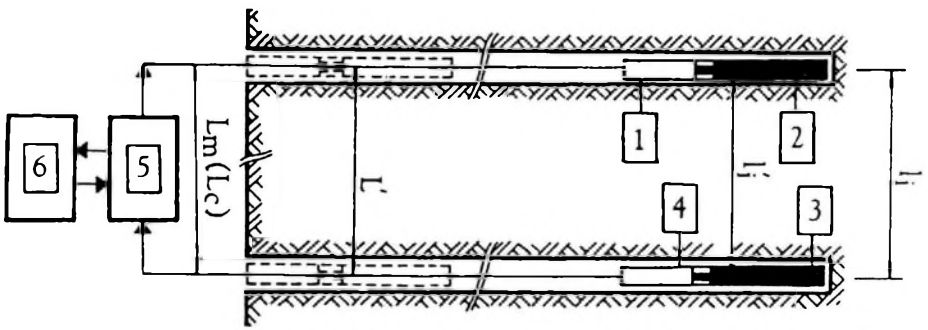

Fig. 4. Principle of the magnetic pulse method. 1—pulse feeder; 2— electromagnet; 3— sensor; 4— circuit for signal regulation; 5— control and evaluation system; 6— operator

4. ábra. A mágneses impulzus módszer alapelve. 1—impulzus töltõ; 2—elektromágnes; 3—érzékelõ; 4—jelszabályozó áramkör; 5—ellenõrzõ és értékelõ rendszer; 6—operátor

Fig. 4 shows the measuring principle with computer adjustment of the measured magnetic induction values. The main part of the power system is the pulse feeder which is connected to the electromagnet. Direct current in the range from 1 to 10 amperes [A] is sufficient to saturate the electromagnet and generate a magnetic field with the required induction. The measuring element is the sensor with the circuit for signal regulation. Theoretically, if it is taken into account that the measuring circuit operates in the pulse regime, interference by external stationary magnetic fields can be ignored.

The mutual position of boreholes can then be determined from the distribution of their openings and the distribution plan of the bottoms of these boreholes, this plan being constructed on the basis of the distances between the individual boreholes in the plane perpendicular to their direction.

3. Magnetic measurements in boreholes

Measurements taken in holes are based on calibration curves. The elements of a calibration base and the conditions of calibration measurements (distances between the probes, intensities of current pulses) are selected in accordance with the need to obtain the required number of calibration curves. These curves are then plotted as a graphic function of the measured induced current I_i on the logarithmic scale against length (distance) l between the probes (*Fig. 5*).

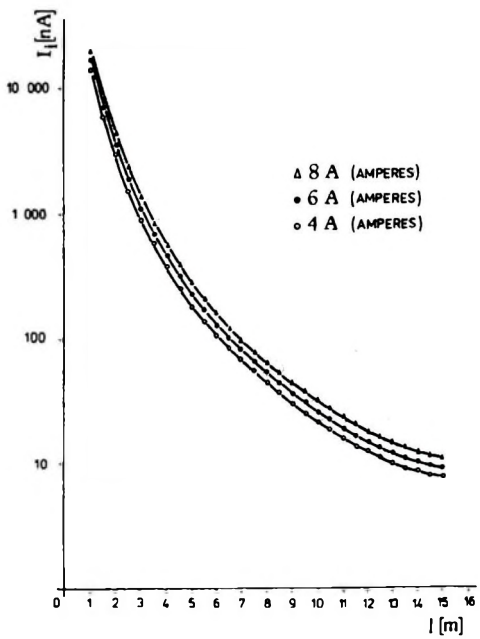

Fig. 5. Calibration curves; measured induced current I_i, length (distance) l between probes

5. ábra. Kalibrációs görbék, I_i a mért indukált áram, l a hosszúság (távolság) a minták között

When determining the distance between the boreholes it is necessary to eliminate the influence of the magnetic properties of the surrounding rock on the magnetic induction measured value. This problem is solved by introducing the correction coefficient k, which is determined in-situ by the source and measuring probes inserted in the openings of two boreholes where we want to determine the distance of their bottoms (Fig. 4). The probes are inserted in the borehole openings so that both probes are situated in the full-space of a rock material. From the measured data of magnetic induction we can estimate the correction coefficient k as the ratio of the measured or calculated distance L_m (L_c), (L_m is equal to L_c), to distance L',

$$K = \frac{L_m}{L'} = \frac{L_C}{L'} \tag{9}$$

which can then be used to correct the individual distances l_i in the mapping area

$$l_i = kl_i' \tag{10}$$

where L' and l_i' are the distances determined from the appropriate calibration graph.

Determination of the correction coefficient k in this way assumes invariable magnetic permeability of a rock mass.

The magnitude of magnetic induction B depends directly on the magnetic permeability μ and the magnetic intensity H of a medium in which the electromagnet is found. This follows from the known relation for a power activity of the generated magnetic field

$$B = \mu H \tag{11}$$

4. Verification of magnetic measurements under mining conditions

The proposed magnetic pulse method of determining the mutual position of the boreholes arranged in a group was successfully verified directly under mining conditions, in a protective pillar F-8 in the fourth mining horizon of the underground, Bankov mine — Slovak Magnesite Mines in Košice [SEDLÁK 1991].

Magnetic measurements were taken in a group of six quasi-parallel and quasi-horizontal boreholes drilled through the protective pillar. The coordinates of the points 1, 2, 3, ... 6 of their openings and the points 1', 2',3', ... 6' of their bottoms as well as the coordinates of the points 1_m, 2_m, 3_m, ... 6_m; $1_m'$,$2_m'$,$3_m'$, ... $6_m'$, of magnetic measurements were calculated from the positional and levelling surveys in the geodetic coordinate system (*Fig. 6*). Because the differences of magnetic measurements at points 1, 2, 3, ... 6 and 1_m, 2_m, 3_m, ... 6_m (analogically 1', 2', 3', ... 6' and $1_m'$, $2_m'$, $3_m'$, ... $6_m'$) were neglected, all

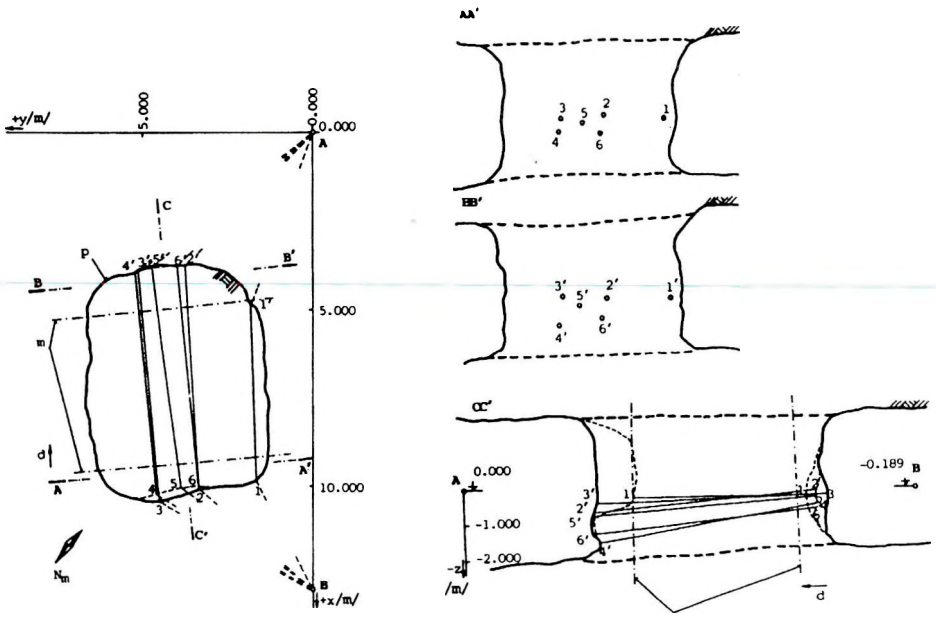

Fig. 6. Block scheme of the magnetic measurements in boreholes in the Slovak Magnesite Mines -Košice. d—drilling direction; m— plans of magnetic mapping; p— protective pillar

6. ábra. A Szlovák Magnetit Bányák (Kassa) fúrólyukaiban mért mágneses mérések blokkvázlata. d—fúrásirány; m—a mágneses térképezés tervei; p—védőpillér

accuracy analyses are applied to the points 1, 2, 3, ... 6 of the borehole openings and 1', 2', 3', ... 6' of the borehole bottoms.

The pulsed magnetic method was applied at saturating currents of 3 and 4 A without commutation. The resultant lengths in the average values of the lengths l_{mag} obtained from the individual magnetic measurements using three electromagnets in all boreholes are presented in *Table I.* The lengths l_{calc} were calculated on the basis of the positional and levelling surveys. All calculations are supplemented by analysis of the estimated distance accuracy.

On the basis of comparison of the correction coefficient k=0.931 and the magnetic permeability values μ of rock in the protective pillar, formed by a mixture of carbonates of the magnesite series with $MgCO_3$ prevailing (based on laboratory measurements, the magnetic permeability of this material is μ=0.9282667, i.e., approximately 1), it can be concluded that the correction coefficient value k of magnetic measurements is represented by the magnetic permeability μ of the surrounding rock; *k is* just satisfied in respect of the accuracy of 1 when working in homogeneous rocks. The accuracy will drop significantly in mineralized rocks, where the magnetic susceptibility varies in a wide range even within a few meters [SEDLÁK 1992].

Points in boreholes	LENGTHS l_{calc}	l_{mag} [m]	$l_i = kl_{mag}$	Real errors $E = l_{calc}-l_i$ [mm]	Square EE [mm^2]
1_1-2_1	1.716	1.792	1.668	48	2304
1_1-3_1	2.960	2.968	2.763	197	38809
1_1-4_1	3.031	3.190	2.970	61	3721
1_1-5_1	2.348	2.470	2.300	48	2304
1_1-6_1	1.870	1.918	1.786	84	7059
2_1-3_1	1.269	1.337	1.245	24	576
2_1-4_1	1.378	1.435	1.336	42	1764
2_1-5_1	0.671	0.677	0.630	41	1681
2_1-6_1	0.556	0.575	0.535	21	441
3_1-4_1	0.454	0.592	0.551	-97	9409
3_1-5_1	0.722	0.795	0.740	-18	324
3_1-6_1	1.276	1.448	1.348	-72	5184
4_1-5_1	0.726	0.770	0.717	9	81
4_1-6_1	1.203	1.220	1.136	67	4489
5_1-6_1	0.622	0.640	0.596	26	676
1_2'-2_2'	1.849	1.958	1.823	26	676
1_2'-3_2'	3.172	—	—	—	—
1_2'-4_2'	3.359	3.523	3.280	79	6241
1_2'-5_2'	2.695	—	—	—	—
1_2'-6_2'	2.100	2.208	2.056	44	1936
2_2'-3_2'	1.325	1.425	1.327	-2	4
2_2'-4_2'	1.606	1.708	1.590	16	256
2_2'-5_2'	0.860	0.898	0.836	24	576
2_2'-6_2'	0.600	0.672	0.626	-26	676
3_2'-4_2'	0.830	0.890	0.829	1	1
3_2'-5_2'	0.565	—	—	—	—
3_2'-6_2'	1.332	1.497	1.394	-62	3841
4_2'-5_2'	0.821	0.843	0.785	36	1296
4_2'-6_2'	1.270	1.400	1.303	-33	1089
5_2'-6_2'	0.782	0.875	0.815	-33	1089

Mean square error: $m = \pm ([EE]/n)^{1/2}$
Openings: $m_{LM(0)} = \pm 72.5$ mm; Bottoms: $m_{LM(B)} = \pm 38.4$ mm
Average: $m_M = \pm 55.4$ mm

Table I. Resultant distances between boreholes from magnetic measurements
I. táblázat. A fúrólyukak közötti távolságok a mágneses mérések alapján

5. Analysis of distance accuracy

The accuracy of the magnetic method under investigation is determined by comparing distances between borehole openings and borehole bottoms determined geodetically with the same distances determined magnetically.

N. B. To simplify the symbols used, the following are introduced:

— borehole openings:

$$l_{calc} = L_{12G}, L_{13G}, \ldots L_{56G} = L_{ijG} = L_G$$
$$l_{mag} = L_{12M}, L_{13M}, \ldots L_{56M} = L_{ijM} = L_M \qquad (12)$$

— borehole bottoms:

$$l_{calc}' = L_{12G}', L_{13G}', \ldots L_{56G}' = L_{ijG}' = L_G'$$
$$l_{mag}' = L_{12M}', L_{13M}', \ldots L_{56M}' = L_{ijM}' = L_M' \qquad (13)$$

Accuracy of distances determined geodetically

Every space distance L_{ij}; $i, j < 1,n>$ is defined by two points B_i, B_j whose coordinates X, Y, Z are determined geodetically in a cartesian three-dimensional rectangular system.

For these distances the following hold:

$$L_{12} = (X_2-X_1)^2+(Y_2-Y_1)^2+(Z_2-Z_1)^2$$
$$\vdots \qquad (14)$$
$$L_{ij} = (X_j-X_i)^2+(Y_j-Y_i)^2+(Z_j-Z_i)^2$$
$$\vdots$$
$$L = f(C_1, \ldots C_i, C_j, \ldots) \qquad (15)$$

where

$$C_i = \begin{bmatrix} X_i \\ Y_i \\ Z_i \end{bmatrix} \qquad (16)$$

is the 3x1 vector of coordinates of a point B_i and

$$\sum_{Ci} = \begin{bmatrix} m_{Xi}^2 & & \\ & m_{Yi}^2 & \\ & & m_{Zi}^2 \end{bmatrix} \tag{17}$$

is its covariance matrix (with zero covariance components).

In order to express the variances of L, the known law of propagation of variances can be applied to (15) in the form

$$\Sigma_L = F \cdot \Sigma_C \cdot F^T \tag{18}$$

where

$$\sum_C = \begin{bmatrix} m_{X1}^2 & & & & & & & & \\ & m_{Y1}^2 & & & & & & & \\ & & m_{Z1}^2 & & & & & & \\ & & & m_{X2}^2 & & & & & \\ & & & & m_{Y2}^2 & & & & \\ & & & & & m_{Z2}^2 & & & \\ & & & & & & \cdot & & \\ & & & & & & \cdot & & \\ & & & & & & & m_{X6}^2 & \\ & & & & & & & & m_{Y6}^2 \\ & & & & & & & & & m_{Z6}^2 \end{bmatrix} \tag{19}$$

is the covariance matrix of all coordinates of six points and

$$F = \begin{bmatrix} \frac{\partial L_{12}}{\partial X_1}, \frac{\partial L_{12}}{\partial Y_1}, \frac{\partial L_{12}}{\partial Z_1}, \ldots \frac{\partial L_{12}}{\partial X_i}, \frac{\partial L_{12}}{\partial Y_i}, \frac{\partial L_{12}}{\partial Z_i}, \ldots \frac{\partial L_{12}}{\partial X_6}, \frac{\partial L_{12}}{\partial Y_6}, \frac{\partial L_{12}}{\partial Z_6} \\ \cdot \\ \cdot \\ \frac{\partial L_{23}}{\partial X_1} \\ \cdot \\ \cdot \\ \frac{\partial L_{ij}}{\partial X_1}, \frac{\partial L_{ij}}{\partial Y_1}, \frac{\partial L_{ij}}{\partial Z_1}, \ldots \frac{\partial L_{ij}}{\partial X_i}, \frac{\partial L_{ij}}{\partial Y_i}, \frac{\partial L_{ij}}{\partial Z_i} \\ \cdot \\ \cdot \end{bmatrix} \quad (20)$$

is the matrix of related coefficients (Jacobian matrix).

Because the plane of the borehole opening and bottom distributions is small (about 12 to 15 m^2), the standard errors m_X, m_Y, m_Z in (19) were taken as a 'middle point' determined by calculating the average measured values: horizontal angles, zenith distances z, and lengths d between point B and points 1, 2, 3, ... 6; and point A and 1', 2', 3', ... 6'. The variances and the standard errors obtained for this 'middle point'

$$\begin{aligned} m_X^2 &= 12.3 \text{ mm}^2 \\ m_Y^2 &= 12.3 \text{ mm}^2 \\ m_Z^2 &= 2.2 \text{ mm}^2 \end{aligned} \quad (21)$$

have then been introduced into the matrix Σ_C (19).

The covariance matrix Σ_L indicates the variances of determined lengths L_{ij}. The variances $m_{Lij}2$ of these lengths are situated on the diagonal of this matrix and the covariances m_{Lij} off the diagonal.

$$\sum_L = \begin{bmatrix} m_{L12}^2, & m_{L12,13}, & \cdot & \cdot & \cdot \\ m_{L13,12}, & m_{L13}^2 & \cdot & & \\ \cdot & & \cdot & & \\ \cdot & & m_{Lij}^2 & & \\ \cdot & & & \cdot & \\ \cdot & & & & \cdot \end{bmatrix} \quad (22)$$

Table II shows the mean square (standard) errors obtained.

Distance		Mean square error		
L_{ijG} [m]		m_{Lij}^2 [mm^2]	m_{Lij} [mm]	$m_{average}$
L_{12}	1.716	20.7	4.5	openings:
L_{13}	2.960	21.2	4.6	
L_{14}	3.031	20.6	4.5	$m_{LG(0)}$ = ±4.2 mm
L_{15}	2.348	20.5	4.5	
L_{16}	1.870	19.8	4.4	
L_{23}	1.269	21.1	4.6	
L_{24}	1.378	19.3	4.4	bottoms:
L_{25}	0.673	18.7	4.3	
L_{26}	0.556	2.9	1.7	$m_{LG(B)}$ = ±4.0 mm
L_{34}	0.454	15.6	3.9	
L_{35}	0.722	23.3	4.8	
L_{36}	1.276	20.0	4.5	
L_{45}	0.726	20.4	4.5	average:
L_{46}	1.203	20.7	4.5	
L_{56}	0.622	15.0	3.9	m_G = ±4.1 mm
L_{12}'	1.849	24.4	4.9	
L_{13}'	3.172	1.5	1.2	
L_{14}'	3.356	23.5	4.8	
L_{15}'	2.695	24.7	5.0	
L_{16}'	2.100	23.3	4.8	
L_{23}'	1.325	24.1	4.9	
L_{24}'	1.606	19.7	4.4	
L_{25}'	0.860	24.2	4.9	
L_{26}'	0.600	7.0	2.6	
L_{34}'	0.830	4.8	2.2	
L_{35}'	0.565	15.6	3.9	
L_{36}'	1.332	17.4	4.2	
L_{45}'	0.821	12.5	3.5	
L_{46}'	1.270	23.9	4.9	
L_{56}'	0.782	19.0	4.4	

Table II. Mean square errors of the distances (L_G,L_G')
II. táblázat. A távolságok (L_G,L_G') átlagnégyzetes hibái

Accuracy of distances determined magnetically

Whole accuracy analysis of distances l_{mag} (L_M,L_M',) determined by the magnetic pulse method is included in Table I. The mean square error m_M was calculated on the basis of the calculated distances l_{calc} (L_G,L_G').

6. Comparing accuracy of distances determined geodetically with those determined magnetically

If it is taken into consideration that the distances L_G are determined with the standard error m_G= ±4.1mm, it means that these distances are not exact. Then the final standard error m_{MAG} of the magnetically determined distances will be given by

$$m_{MAG} = \pm(m_M{}^2 - m_G{}^2)^{1/2}$$
$$m_{MAG} = \pm 55.2 \text{ mm} \qquad (23)$$

For detailed accuracy analysis of the distances determined by the magnetic pulse method the following should be taken into account: the standard errors of the magnetic induction value deductions B (I_i) on the measuring device, of the rock magnetic permeability μ determination, of the calibration curve distance deduction, etc., too. However, in mining activities where a 10% length toleration of determined distances between boreholes is sufficient, a 5% accuracy in the magnetically determined distances is sufficiently accurate.

7. Conclusion

The possibilities of magnetically determining borehole deviations are presented. The proposed magnetic pulse method is utilized in determining the mutual positions of boreholes arranged in groups, e. g. blasting boreholes, freezing and grouting boreholes.

Borehole deviations whose convergence or divergence is not greater than 15 to 20° can be determined from these magnetic measurements. The measurement range, from 10 m to 12 m and more, with an accuracy about ±5%, is completely adequate for this purpose. However, the position of one borehole from a group of boreholes must be determined by an inclinometric method, because the distances between boreholes can be determined by the pulse magnetic method only. The magnetic method presented here can be applied only in straight boreholes, i. e. in boreholes whose axes are lines, not curves. In spite of these limits, the magnetic pulse method for determining borehole deviations can find a wide application in tunnelling, mining and structural engineering or boreholes used in other fields.

REFERENCES

BLAŽEK J. 1985: Pulse magnetic method for determining mutual borehole positions. *In*: Proceedings, 3rd Int. Scient. Conf., Mining University in Ostrava, pp. 81-86

REINBOTH H. 1970: Technologie und Anwendung magnetischer Werkstoffe. VEB Verlag Technik Berlin, 510 p.

SEDLÁK V. 1991: Using magnetic methods in mapping technological boreholes in mining conditions. Transactions of the Technical University of Košice **1** (1), pp. 153-158

SEDLÁK V. 1992a: Rock magnetism and borehole magnetic measurements. Geologica Carpathica **43**, 3, p.169

SEDLÁK V. 1992b: The geomagnetic field influence upon electromagnet magnetic properties. (in Czeh) Slaboproudy obzor **5-6**, 53, pp. 97-98

SEDLÁK V. 1993: Magnetic induction applied to borehole deviation problems. Geotechnical and Geological Engineering **11**, London, pp. 25-35

SINKALA T. 1987: Rock and hole pattern influence on precussion hole deviations — A Field Study. *In*: Int. Conf. 'Drillex'87', Stoneleigh, (poster)

MÁGNESES IMPULZUS MÓDSZER A FÚRÓLYUK ELHAJLÁSÁNAK MÉRÉSÉRE

Vladimír SEDLÁK

Fúrólyuk-elhajlást mérő mágneses módszert mutatnak be, amely bizonyos esetekben, alagút kihajtásban és más földalatti munkáknál alkalmazható. A mélyszinti bányákban illetőleg egyéb mérnöki munkálatoknál a víztároló rétegekben a fagyasztásos és a cement-injektálásos módszernél a fúrólyukak kölcsönös elhelyezését határozzák meg. A fúrólyukak közötti távolság meghatározásához az impulzusos mágneses módszert hibaelemzéssel egészítették ki.

GEOPHYSICAL TRANSACTIONS 1994
Vol. 39. No. 1. 77-87

INTERCORRELATION OF CAPILLARY PRESSURE DERIVED PARAMETERS FOR SANDSTONES OF THE TÖRTEL FORMATION, HUNGARY

Abdel Moktader A. EL SAYED*

Porosity, permeability and capillary pressure data of 50 sandstone core samples obtained from the Törtel Formation have been used to evaluate reservoir quality. Three types of reservoir rocks and capillary curves are outlined, and various correlation charts constructed to delineate porosity, permeability, pore throat size, recovery efficiency, height above free water level and capillary pressure at different water saturation values of the reservoir rock. The capillary pressure techniques utilized are typically favoured for geological and engineering applications to develop sandstone pay zones of the Törtel Formation.

Keywords: capillary pressure, sandstone, Hungary

1. Introduction

The results of capillary pressure can be used by geologists, petrophysicists and petroleum engineers to evaluate reservoir quality, fluid saturation, seal capacity, thickness of the transition zone, and to approximate recovery efficiency during primary or secondary recovery.

Capillary pressure studies of potential hydrocarbon reservoirs is important because capillarity controls the static distribution of fluids in the reservoir prior to production and the remaining of hydrocarbons after primary production [VAVRA et al. 1992].

The Törtel Formation of the Great Hungarian Plain was the target for the present studies. This Formation is penetrated by more than 900 holes drilled in the Algyő oil and gas field (*Fig. 1*). It comprises five hydrocarbon bearing sandstone reservoirs. Upwards from below; these pay zones are: Algyő-1,

* Dept. of Geophysics, Fac. of Science, Ain Shams University Abbasia, Cairo, Egypt.
Manuscript received: 4 December, 1992

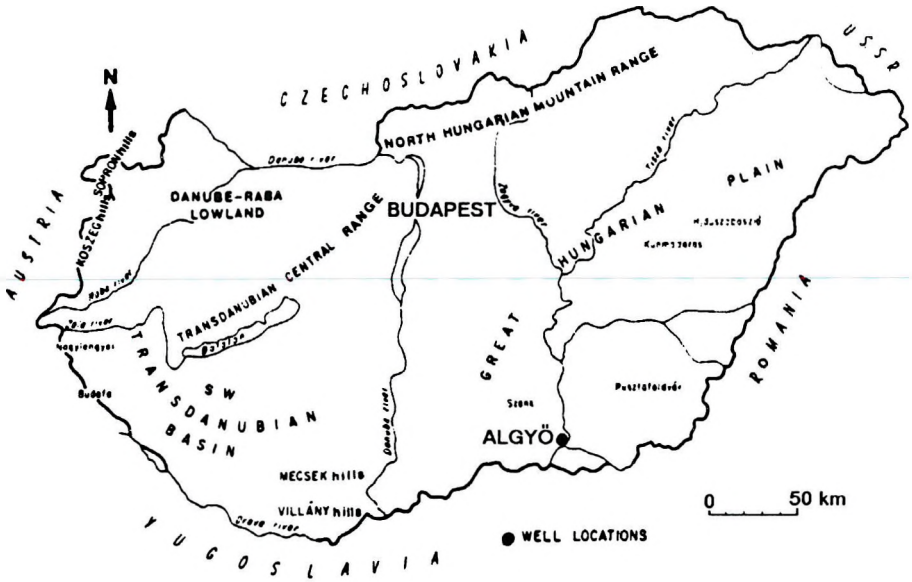

Fig. 1. Location map
1. ábra. Helyszínrajz

Algyő-2, Szeged-1, Szeged-2 and Szeged-3. The Törtel Formation (Pannonian s.l.) overlies the Algyő Formation and underlies the Zagyva Formation. It is interpreted as deltaic sandstone [MUCSI, RÉVÉSZ 1975, EL-SAYED 1981, BÉRCZI, PHILLLIPS 1985; BÁN, EL-SAYED 1987, JUHÁSZ 1991], and was studied from the aspect of petrophysics by EL-SAYED and VOLL [1992]. Delineation of both productive and non productive traps in the Törtel Formation was studied by EL-SAYED [1992].

In the present work, the data of 50 sandstone core samples derived from mercury injection capillary pressure curves were investigated with a view to constructing correlation diagrams in order to delineate reservoir concepts for evaluating the Törtel Formation.

2. Methodology

The gas permeability of the core samples was measured by using a Ruska Gas permeameter. The measuring technique is outlined by EL-SAYED and VOLL [1992]. Mercury porosimetry is used to approximate reservoir conditions, and allows accurate determination of the petrophysical properties of sandstones of the Törtel Formation.

The term capillary pressure as used in this paper, refers to the injection pressure necessary to inject non-wetting fluids (mercury) into the sandstone

pore spaces. The capillary pressure (P_c) was calculated using the equation (modified by WARDLAW 1976, from WASHBURN 1921 and BERG 1975):

$$P_c = 2\gamma \cos\theta / r \qquad (1)$$

where:

γ — surface tension of Hg (485 dynes/cm),
θ — contact angle of mercury in air (140°) and
r — radius of pore aperture for a cylindrical pore.

The height of hydrocarbon column required (i.e. weight above the free water level) to attain a pressure of interest for the sandstone samples was calculated by using the equation:

$$h = P_c / (0.433\ (\rho_b - \rho_{hc})) \qquad (2)$$

h is the height above the free water level (in ft), ρ_b=1.0 g/cm^3 and ρ_{hc}=0.71 g/cm^3 are the specific gravities of brine and hydrocarbons under reservoir conditions, respectively, and 0.433 psi/ft is the conversion factor.

Mercury injection pressure is increased in a stepwise manner and the percentage of rock pore volume at each step is corrected after allowing sufficient time for equilibrium to be reached. The pressure is then plotted against the mercury saturation (*Fig. 2*) resulting in the injection curve. Data from the

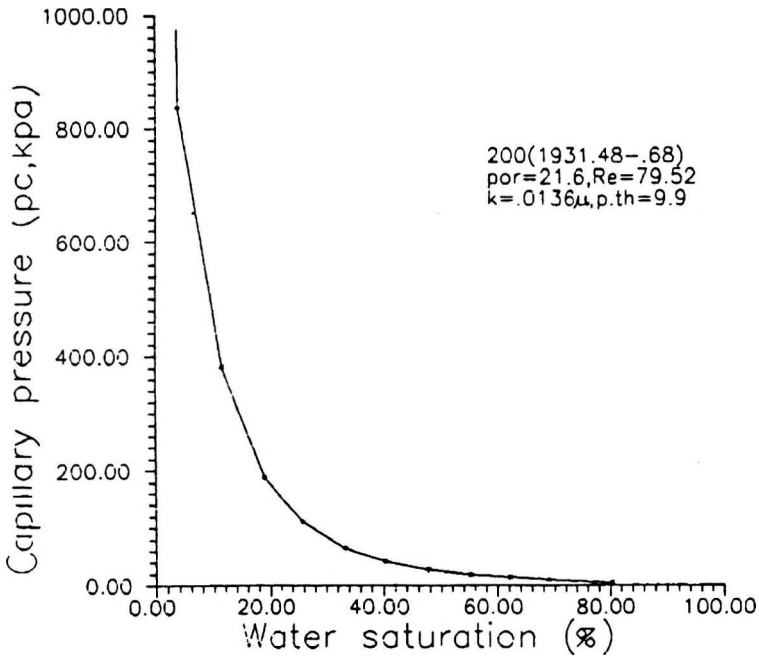

Fig. 2. Injection capillary pressure curve
2. ábra. Injektálásnál a kapilláris nyomásgörbe

mercury injection curve is used to approximate the distribution of pore values accessible by throats of given effective size using the equation:

$$r_c = 107.6/P_c \quad (3)$$

r_c (μm) and P_c is capillary pressure (psi).

By using the air imbibation curves, the withdrawal efficiency [WARDLAW, TAYLOR 1976] or recovery efficiency [HUTCHEON, OLDERSHOW 1985] was defined as:

$$R_e = ((S_{max} - S_r)/S_{max}) \cdot 100 \quad (4)$$

The recovery efficiency (R_e) in the mercury/air system is governed by pore geometry.

3. Results and discussion

From the standpoint of geology, the mercury injection capillary pressure curves obtained for sandstones of the Törtel Formation gave considerable information about the reservoir pore space geometry as discussed below:

Pore throat and reservoir types

Both the sorting and skewness of the pore throat sizes were determined on the basis of the curve shape of the mercury injection capillary pressure [JODRY 1972, VAVRA et al. 1992]. Accordingly, the sandstones of the Törtel Formation were mainly affiliated to three capillary pressure curve types (*Fig. 3a*). They are well-sorted coarse skewness; poorly-sorted coarse skewness; and poorly-sorted slight fine skewness. The first two types are represented by 87 % of all the studied samples; the last type, however, is represented by only 13.0 % of all the samples.

The reservoir types were depicted by using the classification adopted by JODRY [1972]. The sandstone samples exhibiting well-sorted coarse skewness and poorly-sorted slight coarse skewness are classified as good and intermediate reservoirs respectively; the samples showing poorly-sorted slight fine skewness are mainly specified as poor reservoir type (Fig. 3b). This histogram reveals that 87 % of the sandstones of the Törtel Formation are mainly classified as good to intermediate reservoit rocks.

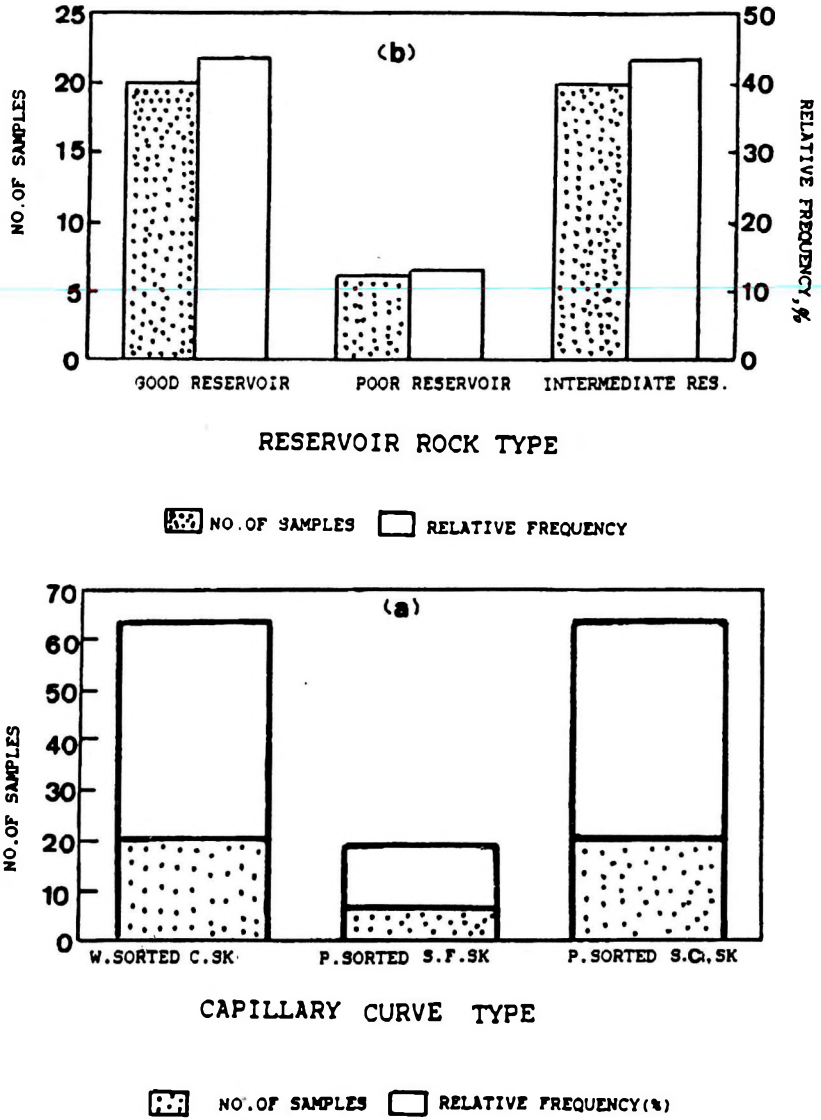

Fig. 3. Graph showing classification of capillary pressure curves (a) and reservoirs rock types (b)
3. ábra. A kapilláris nyomásgörbék (a) és a tározó kőzettípusok (b) osztályozását bemutató diagramok

Porosity vs. water saturation

The measured porosity data were plotted against water saturation (volume of pore filled by wetting phase) at different values of heights above free water level (where P_c=0.0, *Fig. 4a*). This plot illustrates that water saturation increases with decreasing porosity at heights ranging from 0.0 up to 150 m above the free water level (all pores are filled with water). This plot could be beneficial for reservoir porosity determination at any required height above free water level in the Törtel Formation if water saturation is known. Therefore, the next step is to estimate the actual depth of the free water level. This is typically done by comparing hydrocarbon shows and measured fluid saturations with capillary pressure data [SCHOWALTER, HESS 1982].

Figure (4b) shows the height above free water level and capillary pressure versus water saturation at porosity ranges from 12.2 % to 29.39 %. The figure serves for the sandstone reservoir performance and description within the Törtel Formation in the Algyő field.

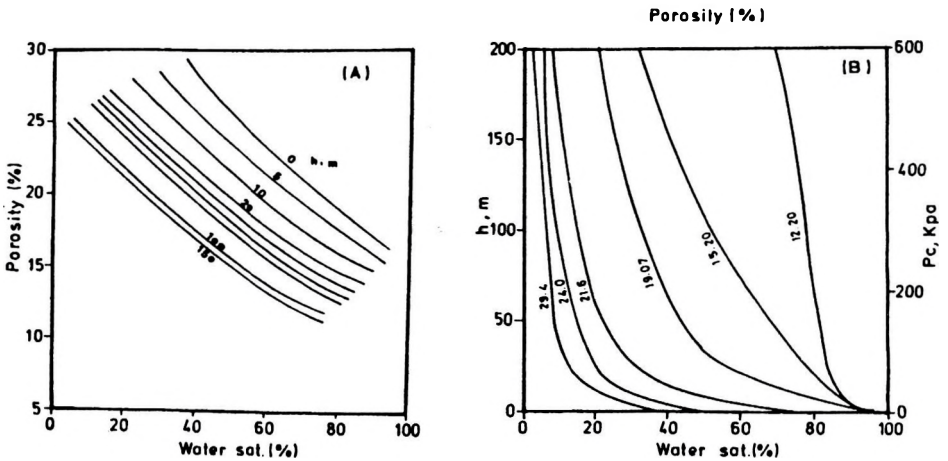

Fig. 4. Porosity vs. water saturation at different values of height (A). Water saturation vs. height and capillary pressure at different porosity values (B)

4. ábra. Porozitásértékek a víztelítettség függvényében különböző magasságértékekre (A). Víztelítettség a magasság és a kapillárisnyomás függvényében különböző porozitásértékekre (B)

Permeability vs. water saturation

The measured gas permeability data has been plotted against water saturation values calculated from mercury injection capillary pressure curves

at heights ranging from 0.0 m to 150 m (Fig. 5a). The plot shows that at any certain fixed height the water saturation decreases with increasing permeability. At the same time the water saturation also decreases with increase in height above the free water level. In the same manner, if we know the height above the free water level, then we can calculate the water saturation and/or hydrocarbon saturation from the permeability data. *Fig. 5b* exhibits the other version of the same relationship; in addition, the capillary pressure is plotted.

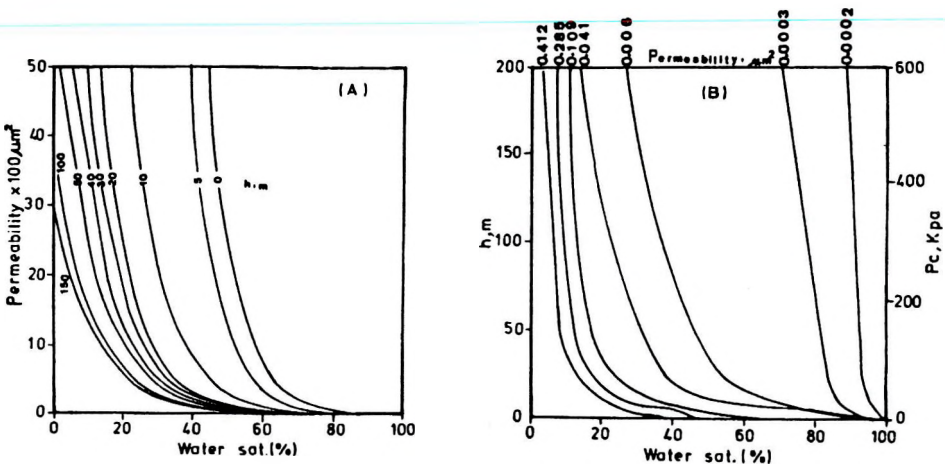

Fig. 5. Permeability vs. water saturation at different heights (A). Water saturation vs. height and capillary pressure at different values of permeability (B)

5. ábra. Permeabilitás a víztelítettség függvényében különböző magasságértékekre (A). Víztelítettség a magasság és kapillárisnyomás függvényében különböző permeabilitás értékekre (B)

Pore throat size vs. water saturation

The pore throat size data obtained from the mercury injection porosimetry is converted from angstrom units (Å) into phi-scale (geologically recognized statistical measure). The phi values are equal to the negative logarithm of the base=2.0 of the millimeter value. The high phi values of pore entry radius represent small pore throats, whereas low phi values represent relatively large pore throats.

Fig. 6a reveals that water saturation increases with decrease in the pore throat sizes (high phi values) towards the free water level. This diagram enables the pore throat size to be estimated at any height value from the free water level, if the water saturation is known. On the other hand, if both the water saturation and the pore throat size are known for a certain interval in the Törtel Formation, then the height above the free water level can be determined (*Fig. 6b*).

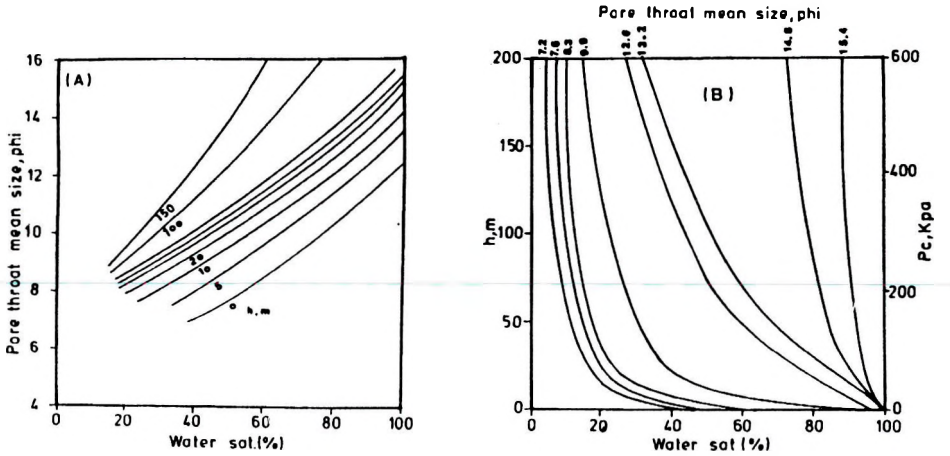

Fig. 6. Pore throat size vs. water saturation at different heights (A). Water saturation vs. height and capillary pressure at different values of pore throat size (B)

6. ábra. Pórusnyílás méret a víztelítettség függvényében különböző magasságértékekre (A). Víztelítettség a magasság és kapillárisnyomás függvényében különböző pórusnyílás méretekre (B)

Recovery efficiency vs. water saturation

The recovery efficiency (R_e) of the wetting phase (water) has been determined and related to both water saturation and height above free water level (*Fig. 7a*). It shows that recovery efficiency increases with increase in water saturation towards the free water level (P_c=0.0). Consequently, the height above the free water level can be determined if both the water saturation and the water recovery efficiency are known (*Fig. 7b*).

Fig. 8 exhibits a summary of the behaviour of the reservoir parameters. The relative values of porosity, permeability, pore throats, recovery efficiency, and height above free water level can be determined at any value of water saturation for the sandstones of the Törtel Formation in the Great Hungarian plain.

4. Conclusions

1. The mercury injection capillary pressure curves obtained for the sandstones of the Törtel Formation were mainly classified into three major types based on both sorting and skewness of the pore throat size distribution.

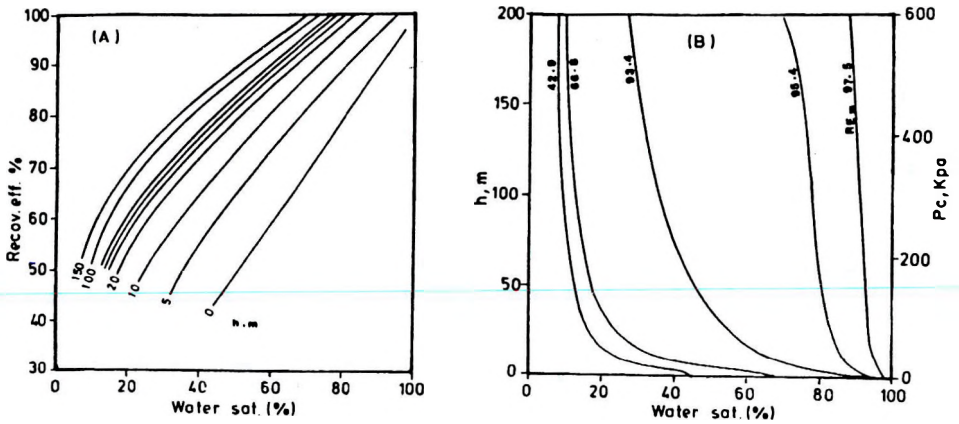

Fig. 7. Recovery efficiency vs. water saturation at different heights (A). Water saturation vs. height and capillary pressure at various values of recovery efficiency (B)

7. ábra. Regenerálódási hatásfok a víztelítettség függvényében kölönböző magasságértékekre (A). Víztelítettség a magasság és a kapillárisnyomás függvényében a regenerálódási hatásfok függvényében (B)

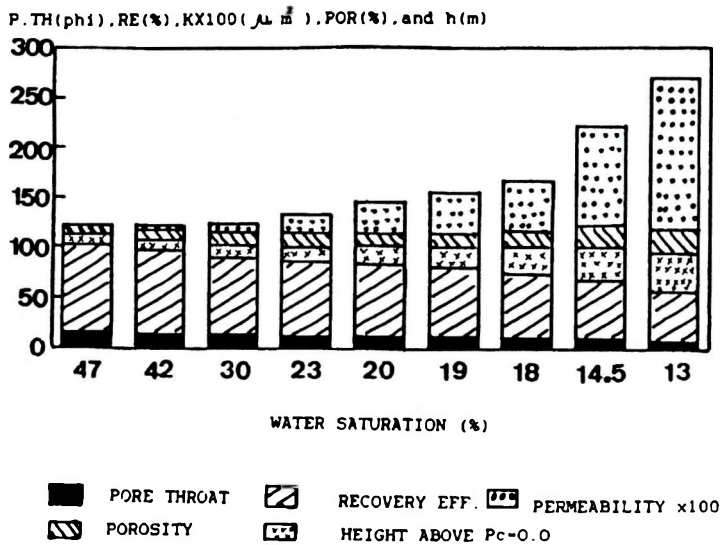

Fig. 8. Graph showing relative abundance of reservoir parameters at different values of water saturation

8. ábra. A tározó paraméterek relatív eloszlása különböző víztelítettség értékeknél

2. Reservoir classification indicates that 87 % of the studied sandstone samples represent good to intermedate reservoir rocks; the rest represent poor reservoir rocks.
3. By estimating the actual depth of the free water level, the fluid saturation, pore throat sizes, recovery efficiency, porosity, and permeability could be determined for sandstones of the Törtel Formation.
4. The reservoir parameters could be outlined from the water saturation values.
5. Care should be taken in transferring these data to other geologic regions.

Acknowledgements

The author acknowledges the financial support provided by the Hungarian Hydrocarbon Institute (SzKFI). Special thanks are due to reservoir geology and petrophysics staff in both Budapest and Szeged. The laboratory assistance of Mr. D. LÁSZLÓ of the Oil and Gas Industrial Laboratory (OGIL) of Szolnok is gratefully acknowledged.

REFERENCES

BÁN A., EL-SAYED A. A. 1987: Genetic delineation of deltaic rock types in terms of log curve shapes in the Algyő-2 hydrocarbon reservoir, Hungary. Acta Geologica Hungarica **30**, 1-2, pp. 231-240

BÉRCZI I., PHILLIPS R. L. 1985: Processes and depositional environments within Neogene deltaic-lacustrine sediments, Pannonian basin, Southeast Hungary. Geophysical Trans. **31**, 1-3, pp. 55-74

BERG R. R. 1975: Capillary pressure in stratigraphic traps. AAPG Bull. **59**, pp. 939-956

EL-SAYED A. A. 1981: Geological and petrophysical studies for the Algyő-2 reservoir evaluation, Algyő oil and gas field, Hungary. Ph. D. Thesis, Hungarian Academy of Science Budapest, 166 p.

EL-SAYED A. A., VOLL L. 1992: Empirical prediction of porosity and permeability in deltaic sandstones of the Törtel Formation, Hungary. Ain Shams Univ. Fac. of Sci. Scient. Bull. **30**, pp. 461-487

EL-SAYED A. A. 1992: Relationship of porosity and permeability to mercury injection derived parameters for sandstones of the Törtel Formation, Hungary. Geophys.Trans. **38**, 1, pp. 35-46

HUTCHEON I., OLDERSHAW A. 1985: The effect of hydrothermal reactions on the petrophysical properties of carbonate rocks. Bull. of Canadian petroleum Geology **33**, pp. 359-377

JODRY R. L. 1972: Pore geometry of carbonate rocks (basic geologic concepts): in oil and gas production from carbonate rocks. G. V. CHILINGAR (ed.). American Elsevier Pub. Co., New York, pp. 35-82

JUHÁSZ GY. 1991: Lithostratigraphical and sedimentological framework of the Pannonian (s. l.) sedimentary sequence in the Hungarian Plain (Alföld), Eastern Hungary. Acta Geol. Hung. **34**

MUCSI M., RÉVÉSZ I. 1975: Neogene evolution of the south-eastern part of the Great Hungarian Plain on basis of sedimentological investigations. Acta Mineral. -Petro., Szeged, XXII, pp. 29-49

SCHOWALTER T. T., HESS, P. D. 1982: Interpretation of subsurface hydrocarbon shows. AAPG Bull. **66**, pp. 1302-1327

VAVRA C. L., KALDI J. G., SNEIDER R. M. 1992: Geological application of capillary pressure: A review. AAPG Bull. **76**, pp. 840-850

WARDLAW N. C. 1976: Pore geometry of carbonate rocks as revealed by pore casts and capillary pressure. AAPG Bull. **60**, pp. 245-257

WARDLAW N. C., TAYLOR R. P. 1976: Mercury capillary pressure curves and the interpretation of pore structures and capillary behavior in reservoir rocks. Bull. of Canadian Petroleum Geol. **24**, pp. 225-262

WASHBURN E. W. 1921: Note on a method of determinig the distribution of pore sizes in a porous material. Proc. of the National Acad. of Science (USA) **7**, pp. 115-116

A KAPILLÁRIS NYOMÁSBÓL LEVEZETETT PARAMÉTEREK KAPCSOLATA A TÖRTEL FORMÁCIÓ HOMOKKÖVEINÉL

Abdel Moktader A. EL SAYED

A rezervoár minőségének becslésére a Törtel formációból 50 homokkő magminta porozitás, permeabilitás és kapilláris nyomás adatait használták fel. A tározó kőzet és kapilláris görbe három típusát körvonalazták és különböző korrelációs térképeket szerkesztettek a porozitás, permeabilitás, a pórus torokméret, a helyreálllítási hatásfok, a szabad vízszint feletti magasság és a kapilláris nyomás között a tározó kőzet különböző víztelítettségi értékei mellett. Az alkalmazott kapilláris nyomástechnika különösen kedvelt a geológiai és mérnöki alkalmazásokban a Törtel formáció műrevaló zónáinak kialakításánál.

EÖTVÖS L. GEOPHYSICAL INSTITUTE OF HUNGARY

THE OLDEST INSTITUTION FOR APPLIED GEOPHYSICS OFFERS THE LATEST ACHIEVEMENTS FOR GROUND-WATER PROSPECTING and ENVIRONMENTAL PROTECTION

The most often occurring demands:

- local geophysical measurements for the water supply of small communities by a few wells
- regional geophysical mapping to determine hydrological conditions for irrigation, regional agricultural development,
- large-scale exploration for the water supply of towns, extended areas i.e. regional waterworks,
- determination of bank storage of river terraces, planning of bank filtered well systems,
- thermal water exploration for use as an energy source, agricultural use or community utilization,
- cold and warm karst water prospecting,
- water engineering problems, water construction works

The Maxi-Probe electromagnetic sounding and mapping system – produced under licence by Geoprobe Ltd. Canada – is an ideal tool for shallow depths, especially in areas where seismic results are poor or unobtainable

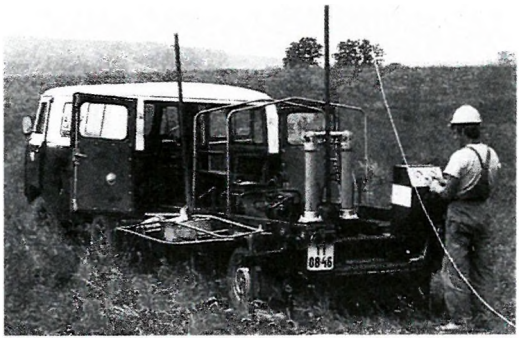

ELGI has a vast experience in solving problems of environmental protection such as control of surface waters, reservoir construction, industrial and communal waste disposal, protection of surface and ground water etc. ELGI's penetrologger provides in-situ information – up to a maximum depth of 30 m – on the strength, sand/shale ratio and density without costly drilling.

Field work with ELGI's 24-channel portable seismograph

ELGI offers contracts with co-operating partners to participate in the whole complex process of exploration–drilling–production.

For further information ask for our booklets on instruments and applications. Let us know your problem and we will select the appropriate method and the best instrument for your purpose.

Our address: ELGI POB 35. Budapest, H–1440. HUNGARY
Telex: 22-6194 elgi h

ESS - 03 - 24

PC based 24 channel portable seismograph

ESS-03 was designed for high-resolution subsurface imaging using up-to-date electronics and computer technology. Compared with excavation or dense drilling networks, it offers a highly cost-effective solution for geotechnical problems.

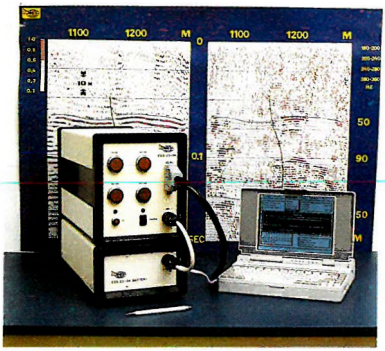

It is an excellent tool

- for raw material prospecting;
- for determining static corrections for surface seismic methods;
- for acquiring information when designing large scale foundations such as factories, dams or roads;
- for seismic investigation of well-sites;
- for in-mine exploration;
- for detection of destructive building-vibrations.

ESS-03 can be used not only for rapid and inexpensive data acquisition, but the built-in PC and software package offer excellent on-site processing, quick-look interpretation, and visual display of the results.

Specifications:

Frequency response: 1-8000 Hz
Resolution: 12 bit A/D+42 dB IFP
Built-in electronic roll along switch
Microprocessor control 80386-SX-20
Data recording on floppy disc 1.44 MB, hard disc 80 MB
Menu-driven operating commands
LCD display with VGA resolution
Self-testing programs and parameter checking
Weight: 10 kg
Dimensions: 200*220*450 mm

Eötvös Loránd Geophysical Institute of Hungary

Budapest, XIV. Columbus u. 17-23.
Letters: H-1440 Budapest, POB. 35.
Phone: (36-1) 184-3309
Fax:(36-1) 163-7256
Telex: (61) 22-6194 elgi h
E-mail: H6123 TIT@ELLA.HU

Founded in 1919

DON'T BUY EQUIPMENT OR SERVICES UNTIL YOU KNOW THE FACTS

ELGI's Well Logging Divison has put its 25 years of experience to work again in the new line of well logging technology in

water,

coal,

mineral,

geotechnical

prospecting

HERE'S WHAT WE OFFER

- Complete series of surface instruments from portable models to the PC controlled data logger
- Sondes for all methods: electrical, nuclear, acoustic, magnetic, mechanical, etc.
- Depth capacity down to 5000 m
- On-site or office computer evaluation
- International Metrological Base for calibration to true petrophysical parameters
- Training and in-house courses
- Design laboratory for custom-tailored assemblies

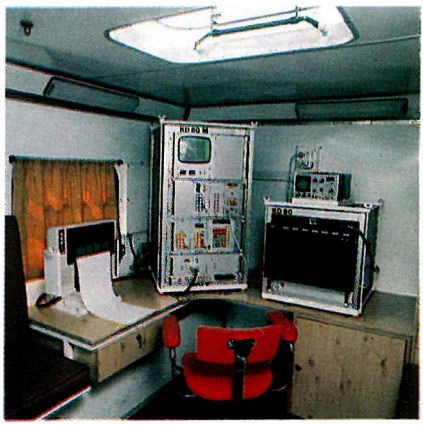

Just think of us as the scientific source of borehole geophysics you may never have heard of

SALES ✣ ✣ ✣ ✣ RENTALS ✣ ✣ ✣ ✣ SERVICES

Well Logging Division of ELGI
POB 35, Budapest, H-1440 Hungary
Phone: (361) 252-4999, Telex: 22-6194,
Fax: (361) 183-7316